Progress in Particle and Nuclear Physics 112 (2020) 103765

Contents lists available at ScienceDirect

Progress in Particle and Nuclear Physics

journal homepage: www.elsevier.com/locate/ppnp

Review

Cosmic ray detection in space

Mirko Boezio [a,b], Riccardo Munini [a,b], Piergiorgio Picozza [c,d,*]

[a] INFN, Sezione di Trieste, I-34149 Trieste, Italy
[b] IFPU, I-34014 Trieste, Italy
[c] INFN, Sezione di Rome "Tor Vergata", I-00133 Rome, Italy
[d] Department of Physics, University of Rome "Tor Vergata", I-00133 Rome, Italy

ARTICLE INFO

Article history:
Available online 3 February 2020

Keywords:
Cosmic rays
Space instrumentation
Particle detectors
Antimatter
Dark matter
Heliosphere

ABSTRACT

Cosmic rays are energetic particles composed primarily of protons and helium nuclei but including, with varying abundances, all atomic nuclei species, electrons and even antiparticles. They originate from sources that, save for the highest energies, are located in the Galaxy. After more than one century from their discovery and except for a clear contribution, particularly important at energies lower than a few GeV, from our Sun the origin of cosmic rays is still an open question. Supernovae explosion, pulsars, relativistic jets, active galactic nuclei, have been proposed as sources of cosmic rays although unambiguous evidences have still to be found. The study of the cosmic radiation have been approached, indirectly, with instrumentation located on ground and, directly, with apparatus placed on stratospheric balloons and satellites. The last decades have seen a flourishing of new techniques applied to space science with satellite-borne experiments taking center stage in the unveiling of the properties of the cosmic radiation.

Contents

* Corresponding author at: Physics Department, University of Rome Tor Vergata, Via della Ricerca Scientifica 1, 00133 Rome, Italy.
E-mail address: Piergiorgio.Picozza@roma2.infn.it (P. Picozza).

https://doi.org/10.1016/j.ppnp.2020.103765
0146-6410/

1. Introduction

Cosmic rays are a sample of solar, galactic and extragalactic matter which includes the nuclei of all elements and their isotopes known in the periodic table, as well as electrons, positrons, and antiprotons. They are associated with the most energetic events and active objects in the Universe as supernovae explosion, pulsars, relativistic jets, active galactic nuclei. The discovery of the cosmic rays dates back to 1912 with the August balloon flight of Victor Hess, awarded in 1936 with the Nobel Prize, measuring the ionization at various altitudes. The ionization, after passing through a minimum immediately above the ground, increased considerably with height, reaching at an altitude of 5200 m a value 100% higher than the total radiation observed on the ground. The key and careful measurements of Hess had been preceded by those at the top of the Eiffel Tower made by Theodor Wulf, on board high altitude balloon by Albert Gockel, and underwater by Domenico Pacini. All data agreed with the conclusion that a non-negligible part of the penetrating radiation was independent from the direct action of the radioactive substances in the uppermost layers of the Earth. For a history of cosmic ray studies see [1]. This discovery led to the birth of Particle Physics that developed for many years by studying cosmic rays in the Earth's atmosphere. Positrons, muons, pions and strange particles were revealed detecting directly cosmic rays or products of their interaction. It took four decades of technological efforts to partially reproduce cosmic ray energies with accelerators and to compete in intensity.

The study of the cosmic radiation from space or close to the top of atmosphere, after starting in the sixties with the pioneer series of Proton satellite experiments of Grigorov [2] and the first unambiguous detection of electrons by Earl [3] and Meyer and Vogt [4], has been accelerating in the '80s and '90s thanks to a massive campaign of experiments mounted on balloons or on small satellites. They completed the transition from the early observation of cosmic radiation as a laboratory for production and direct detection of new particles to the study of the mechanisms of production, acceleration and propagation of cosmic rays in the Galaxy and to their role in the physics of the cosmos.

Fig. 1 shows the cosmic ray fluxes as a function of energy, the so called energy spectrum. It represents one of the most impressive results of the experimental research in astrophysics, ranging for about 32 orders of magnitude in the flux determination and up to 10^{20} in the explored energy. In the energy spectrum of cosmic rays there are, well hidden, the answers to the main questions in the cosmic rays research. Where do these particles are coming from? How and where they are getting accelerated? How do they propagate through the interstellar medium and what kind of interaction do they encounter? What role do they play in the energy budget of the interstellar medium? To what energies the extragalactic contribution becomes dominant? Do we find hints of the existence of exotic particles as relic from the early Universe, as antimatter and dark matter?

In the sub-GeV region cosmic rays are produced or strongly modulated by the Sun. Above few GeV the whole spectrum is approximately described by the power law in energy (E): $E^{-\gamma}$ with a spectral index $\gamma \sim 3$ on average. However, a detailed analysis of the data from experiments probing different energy regions shows a spectral index value of ≈ 2.7 up to $\sim 10^{15}$ eV (shown as a dashed line in Fig. 1), region in which a broad maximum appears, the first knee, centered at $\approx 3 \times 10^{15}$. The knee is followed by a steepening of the spectrum with $\gamma \approx 3.3$, a broad dip centered at $\sim 10^{16}$ eV and a second knee at $\sim 10^{17}$ eV. Very peculiar is the last part of the energy spectrum. A new break in the power law occurs at higher energies with a pronounced hardening of the spectrum around 5×10^{18} eV (the so-called "ankle" feature), followed by an abrupt softening above $\approx 5 \times 10^{19}$ eV. This suppression is considered as due to different reasons: pion-producing interactions between extremely energetic protons and cosmic microwave background (CMB) photons, with a cut-off at $\approx 5 \times 10^{19}$ eV, known today as the GZK effect from Greisen [11] and Zatsepin & Kuz'min [12], and to photo-dissociation of heavier nuclei on cosmic backgrounds, from microwave to ultraviolet. Moreover, it is expected that also a possible acceleration power limit of the source could contribute to the spectral steepening in the cosmic ray energy spectrum.

The cosmic ray particles, at least up to about 10^{15} eV, are considered of galactic origin and the power required for their acceleration is generally thought to be provided by shock waves of expanding supernovae remnants. The observations of high-energy photons presumably coming from neutral pion emission from accelerated protons in the Supernova Remnant W44 [13,14] and SR IC 443 [15] made by Agile and Fermi experiments, measurements performed by Cerenkov imaging telescopes [16] and in X-ray emissions from the borders of SRN [17] strongly support this hypothesis. Currently, the most widely accepted theory on cosmic rays assume that they are mostly ambient interstellar matter accelerated and finally

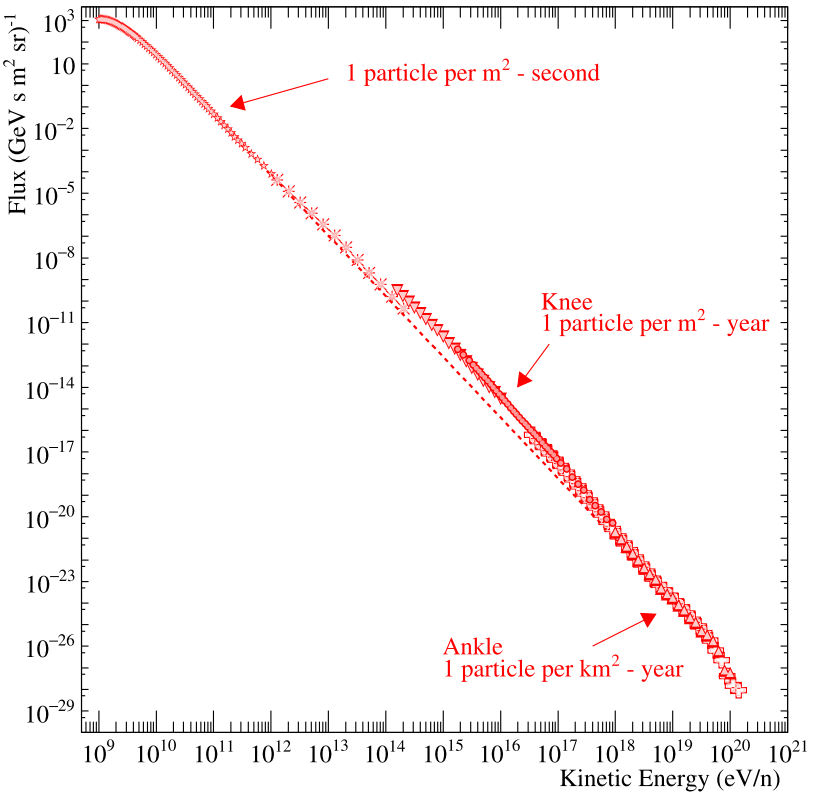

Fig. 1. The cosmic ray energy spectrum: up to about 10^{14} eV proton fluxes from direct measurements are shown, above the all-particle spectrum measured by ground observatories is presented. The dashed line is a power law with spectral index −2.7.
Source: Data used for the figure are from [5–10].

injected as energetic particles into the interstellar space, where they spend about 10^7 years before escaping into the intergalactic space. This long confinement suggests a coupling to the galactic magnetic field as well as a scattering on random magnetic fields that leads to a random walk in real space and in momentum space. This diffusion is confirmed by the high degree of isotropy shown from the cosmic radiation in this energy region. This propagation in the Galaxy affects the energy spectra of cosmic rays that are expected to be different at the source with respect to those measured at Earth. This variation can be understood by studying the fluxes and energy spectra of secondary nuclei that are produced mainly by spallation interaction of primary nuclei with the interstellar matter. These fluxes are directly related to the encountered amount of matter and to the lifetime of the cosmic rays in the Galaxy. Moreover, at low energy, up to a few tens of GeV, solar modulation significantly affects the propagation of cosmic rays in the heliosphere further modifying their energy spectra.

The transition at high energy from a cosmic ray production by galactic to a production by extragalactic sources is an issue still strongly debated. Different theoretical hypotheses claim the first knee as a mark of the end of the galactic contribution and the start of the transition to dominant extra-galactic sources, others assign it to the second knee or to the ankle region if at all (e.g. [18]). Recently, the Pierre Auger Observatory measured unambiguously (at more than 5 σ level of significance) an anisotropy in the arrival direction of cosmic rays with energies above 8 EeV [19]. The magnitude and direction of the anisotropy indicate an extragalactic origin for these ultra-high energy particles.

Many sources have been proposed for extra galactic cosmic rays, covering a large range of astrophysical objects, from extremely fast-spinning young pulsars, across active galactic nuclei and starburst galaxies, to gamma-ray bursts. New exciting information could come from ultra-high energy cosmic rays (UHECRs) with energies around and beyond 10^{20} eV [20,21]. The energy losses by the GZK effect limit the volume of space in which UHECRs can originate to be observed at Earth and, consequently, the number of their powering sources. This feature and the circumstance that at these energies particle deflection by extra-galactic and galactic magnetic fields is weak make it possible to identify individual sources, thus opening the field of particle astronomy. Moreover, in the trans-GZK energy region also a top-down scenario is conjectured, in which UHECRs are produced by the decay or annihilation of Super-Heavy Particles with mass of about $10^{22} - 10^{25}$ eV.

The flux of cosmic rays ranges from about one particle per m^2 per second at a few tens of GeV up to less than one particle per km^2 per one thousand years in the trans-GZK region and beyond, with a few particle per m^2 per year at the energy

around 10^{15} eV. The exploration of the cosmic ray energy spectrum is made by direct space measurements, mainly at satellite orbit or at high altitude, at the edge of space, up to around the first knee. Above these energies the measurements are indirect. They use atmosphere as a calorimeter and very large ground detector arrays. A new method in phase of implementation is to detect UHECRs looking down to the Earth by orbiting telescopes. This is expected to be the future for the studies of UHECRs.

Cosmic rays can also provide information about two of the most compelling issues facing astrophysics and cosmology, the apparent absence of cosmological antimatter and the nature of dark matter. Many questions are still open. What was the role of matter and antimatter in the early Universe? Is the present Universe baryon symmetric or baryon asymmetric? Is the matter only baryonic? What is dark matter made of? Is also the strange quark a component of until now undetected ordinary matter? These topics are now being addressed with great balloon borne, satellite and Space Station experiments using the most advanced technologies. High precision measurements of gamma ray, positron and antiparticle energy spectra could allow to disentangle possible faint contributions of dark matter signals or primordial antimatter from standard antiparticle production. Strange quark matter could instead be revealed looking at its trajectory in the atmosphere.

In this work we will discuss the experimental studies of cosmic rays conducted from the space or near the top of the atmosphere with a focus on the most recent advances in this field. In Section 2 we will discuss the experimental techniques employed in balloon and space-based experiments. Section 3 presents the experimental results obtained from space including discussions on interpretations of the data. Conclusions are drawn in Section 4 with an outlook on the future of the field.

2. Detection of cosmic rays from space

As discussed in the previous section, the energy spectra of cosmic rays (see Fig. 1) spans many decades in energy up to the EeV region. A single instrumental approach is clearly non viable, hence many approaches have been adopted over the years to measure the cosmic radiation. Most significant is the distinction between direct and indirection detentions. Because of the steeply falling energy spectrum higher the energies larger the acceptance and longer the data taking required for a meaningful detection. Since the rate in the so-called knee region (10^{15}–10^{16} eV) is about 1 particle per m^2 per year, it is obvious that at higher energies a direct sampling of the cosmic radiation becomes unfeasible. Over the years, various techniques have been used to measure the cosmic radiation at the highest energies. However, all of them relay on measuring the products of cosmic-ray interactions with the atmosphere, thus the classification of indirect measurements. The vast majority of measurements have been conducted from ground. However, in a few cases apparatus were flown on stratospheric balloons and, ultimately, approaches from space have also been proposed. The indirect experiments and technique from ground will not be discussed in this work that is going to be focused solely on the direct and indirect detection of cosmic rays from space.

2.1. Physical quantities relevant for cosmic ray studies

The answer to the question of the origin, acceleration and propagation of cosmic rays in the Galaxy lies in fully understanding the energy spectrum in Fig. 1. That means measuring the chemical composition of the cosmic rays and how this varies with energy, as well as the energy spectrum of the various components. Is the energy spectrum a nearly smooth power law with just three features as it appears in Fig. 1? And is this valid for all particle species?

The commonly accepted explanation of cosmic rays is based upon two pillars: cosmic rays are interstellar material that are accelerated by shock waves produced by supernovae explosions; after leaving the acceleration sites the cosmic rays propagate in the Galaxy diffusing in the turbulent magnetic fields (for a review see [22]). Models based on these pillars predict near power-law energy spectra at least up to the knee region where the diffusive shock acceleration becomes inefficient and the maximum energy attainable varies linearly with the charge of the cosmic-ray nucleus depending on the model and types of supernovae considered. Therefore, precise measurements of the spectra and composition become the tools to verify these hypothesis discriminating and improving the various models.

In conclusion, to answer the fundamental questions about the cosmic rays it is necessary to measure with the highest precision the cosmic-ray fluxes in the largest energy range possible for as many nuclear components as achievable. Lastly, as will be discussed in Section 3.1, also the location where these measurements are performed plays a significant role that has to be properly accounted for. In the remaining of this section, we will discuss how, in the field of cosmic ray physics, these physical quantities can be and have been measured.

2.2. Energy measurements

2.2.1. Magnetic spectrometers

Except for a minor component at low energy of solar origin, cosmic rays detected at Earth are fully ionized nuclei, since their atomic electrons were stripped during the acceleration phase. The physics behind the acceleration and propagation of cosmic rays involves magnetic fields and turbulence in these fields. Therefore, the most natural "energy" quantity is the rigidity R defined as $R = pc/(Ze)$, c being the speed of light and p the momentum of a particle of charge Ze.

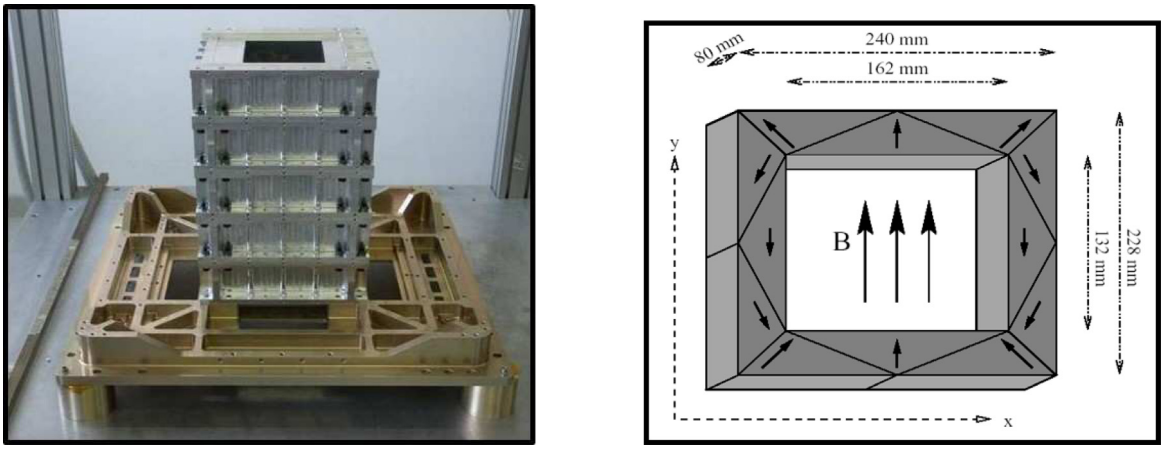

Fig. 2. Left: The PAMELA magnet assembled on the apparatus base plate. Right: Cross-sectional view of a magnetic module and magnetic cavity.

An obvious approach to measure the rigidity is using a magnetic spectrometer, i.e. create a magnetic field in a volume filled with tracking detectors where the trajectories of cosmic rays are recorded. From the knowledge of the cosmic-ray trajectory and of the magnetic field intensity the curvature and, consequently, the rigidity of the cosmic-ray particles is reconstructed.

Fig. 2 shows the magnet [23,24] used in the cosmic-ray satellite-borne PAMELA experiment [25]. The magnet, shown on the left, was composed of five modules forming a tower 44.5 cm high. Each module (shown on the right) comprised twelve magnetic blocks, made of a Nd–Fe–B alloy with a residual magnetization of 1.3 T. The blocks were configured to provide an almost uniform magnetic field oriented along one direction inside a cavity of dimensions 13.1×16.1 cm^2. The five magnetic modules were interleaved with six equidistant 300 μm thick silicon detector planes inserted inside the magnetic cavity. A charged cosmic-ray particle, crossing the magnetic cavity, ionized the silicon sensors providing an information on the impact point on each plane. A track finding algorithm was then used to associate the measured points to a physical track, from which, given the magnetic field map, the rigidity of the particle was derived.

In the case of a constant magnetic field B (in Tesla) the rigidity R (in GV) of a charged particle is related to the radius of curvature r (in meters) of its trajectory (a helix) by [26]:

$$R\cos\lambda = 0.3Br,$$

where λ is the pitch angle of the helix. The measurement error on the rigidity results essentially from two errors: one due to the finite measurement resolution, mostly relevant at high rigidities, and one due to the multiple scattering, particularly important at low rigidities. The error due to the finite resolution scales with R and varies linearly with the spatial resolution σ, i.e. [26]:

$$\frac{\Delta R_{res}}{R} \propto \frac{\sigma}{BL^2}R, \tag{1}$$

with L the projected length of the track on the bending plane.

At low values of the rigidity the dominant uncertainty results from the multiple Coulomb scattering of the particle as it crosses the spectrometer matter. Hence, this error depends on the total track length in the spectrometer, on the radiation length of the scattering medium and on the speed β ($\beta = v/c$, with v particle velocity) of the particle. Therefore, its rigidity dependence can be approximated as:

$$\frac{\Delta R_{ms}}{R} \propto \frac{1}{\beta}, \tag{2}$$

For clarity Fig. 3 shows how these two contributions add up to the rigidity resolution. From this results natural to express the spectrometer bending power in terms of Maximum Detectable Rigidity or MDR. This is the value of the rigidity which corresponds to a 100% uncertainty on its measurement and is commonly related to the upper limit achievable by a magnetic spectrometer.

It is worth noticing that the distribution of measurements of the curvature is approximately Gaussian, while the distribution of rigidity measurements is not. However, the inverse of the rigidity ($\eta = 1/R$), often called magnetic deflection, is proportional to the curvature and, hence, its measurement distribution can be approximated with a Gaussian. Another important point is that the particle trajectory, hence the sign of the curvature, depends on the sign of the charge of the particle. Thus, magnetic spectrometers are an obvious device to discriminate particles according to the sign of the charge, i.e. separate particles from antiparticles.

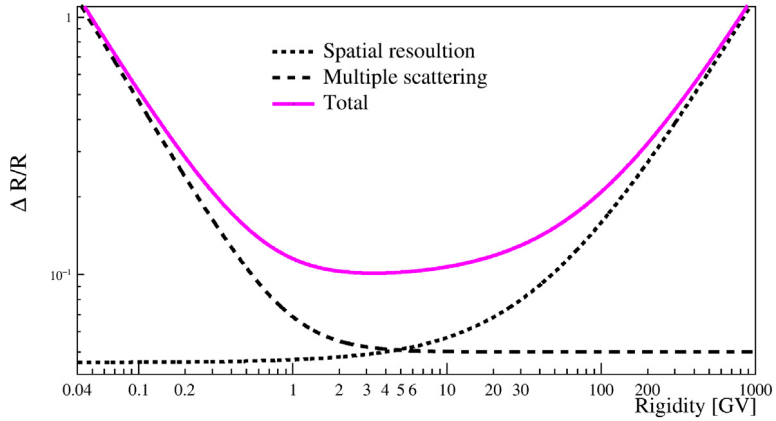

Fig. 3. Generic resolution of a spectrometer with an MDR of 1 TV as a function of rigidity. The short-dashed line shows the error due to the finite spatial resolution (Eq. (1)) while the long-dashed line shows the relative error due to the multiple scattering (Eq. (2)). The solid line is the quadratic sum of the two errors.

A few conclusions can be drawn from Eq. (1) and Fig. 3. Larger values of the magnetic field intensity and of the track length results in lower errors at high rigidities, hence allowing to extend the measurements to higher rigidities (i.e. greater MDR). Similarly, an increase in the precision on the measurements on the impact positions results in a higher MDR. On the contrary, at low rigidities the multiple scattering dominates and the uncertainty on the rigidity measurements is mostly affected by the tracking material.

How does this translate to applications in the field of cosmic rays? The huge energy range spanned by cosmic rays implies that a single solution is not applicable. Even limiting the measurements to the energy region below the "knee", the instruments are required to span more than eight decades in energy, from tens of MeV[1]) up to 10^{16} eV. To properly sample the sub-GeV region a magnetic spectrometer has to be equipped with low density and thin tracking material while the TeV region requires high intensity magnetic field, long track length and excellent spatial resolution. Over the years magnetic spectrometers were developed focusing on various energy ranges addressing different scientific goals.

The first magnetic spectrometer launched in space was Mariya [27] that was first used on the Soviet satellite Salyut 7. Later, improved versions of the spectrometer were installed on board of the Soviet space station Mir. The instruments were designed to measure cosmic rays and particles trapped in the Earth's magnetic belts below a few GeV. The spectrometer consisted of a magnet and a set of scintillators providing tracking and time-of-flight information.

However, magnetic spectrometers had already been used to directly sample the cosmic radiation. They were launched with stratospheric balloons for day-long duration flights. Flying at a few g/cm^2 of residual atmosphere, instruments placed on stratospheric balloons are able to measure the cosmic rays mostly unaffected by interaction with the atmosphere. Particularly interesting was the first detection of positrons in the cosmic radiation by De Shong, Hildebrand and Meyer [28] that using a permanent magnet equipped with spark chambers were able to separate positrons from electrons and measure their energy from 40 MeV to 3 GeV.

The most relevant cases of magnetic spectrometer in space are those of the recent PAMELA [25] and Alpha Magnetic Spectrometer (AMS-02) [29] space-borne experiments. The PAMELA magnetic spectrometer, previously discussed and shown in Fig. 2, operated for 10 years from 2006 until 2016 when the communications with the Russian Resurs satellite, housing the PAMELA experiment, were terminated. The PAMELA permanent magnet (Fig. 2) produced a rather uniform magnetic field of 0.43 T that, together with a spatial resolution of 3 μm in the bending view and a track length of $\approx$ 50 cm, resulted in an MDR of $\approx$ 1 TV for a geometrical acceptance of 0.0022 m^2 sr. AMS-02 was installed on the International Space Station (ISS) in May 2011 and since then it has been in operation. The magnetic spectrometer is composed by a permanent magnet and planes of double-sided silicon detector. The magnetic field intensity is 0.15 T with a spatial resolution of 10 μm over a track length of $\approx$ 3 m resulting in an MDR of $\approx$2 TV for a geometrical acceptance of 0.3 m^2 sr. Relevant experimental results from these two experiments will be discussed in Section 3.

In the sixties it became possible to adapt the superconducting magnet technology to fly cryogenic magnets (e.g. [30]). Illustrative of this concept is the magnet spectrometer used by the BESS experiments [31]. Actually, it was a spectrometer that was continuously improved for a sequence of 11 balloon flights over more than 10 years going for day-long balloon flights to long duration flights of many days. Fig. 4 shows the BESS-Polar II apparatus [31] that flew over Antarctica for 24.5 days of operation. The instrument was equipped with a thin superconducting solenoid magnet capable of producing a rather uniform magnetic field of 0.8 T. Combined with gaseous drift chambers as tracking devices the magnetic

[1] Meaningful galactic cosmic-ray measurements nearby the Earth at these energies and lower are significantly hindered by the solar wind and heliospheric environment as it will be discussed in Section 3.1.

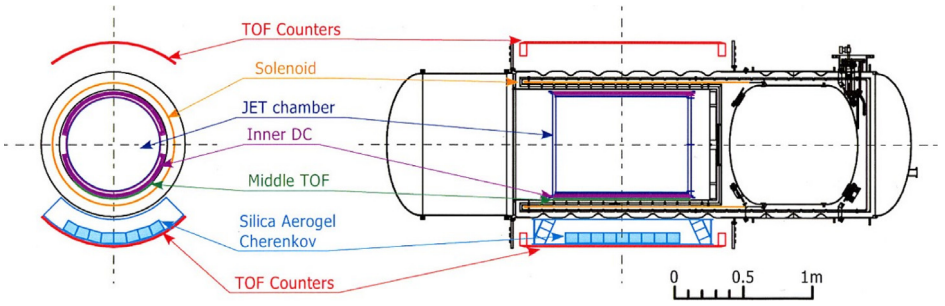

Fig. 4. The BESS-Polar II payload [31].

spectrometer achieved an MDR of $\approx$ 240 GV with a geometrical acceptance of ≈ 0.3 m^2 sr. The instrument was sufficiently light ($<$ 1500 kg) to operate on a long duration flight. The main scientific goal of the instrument was the measurement of the antiproton cosmic-ray component below a few GeV. Therefore, a high MDR was not deemed necessary while it was very important to limit the amount of material traversed by the particles. Hence, the choice of jet chambers with a relatively low spatial resolution (≈ 140 μm) but also low density.

The superconducting magnet provides clear advantages with respect to permanent one:

- significant lower mass, hence possibility to build larger instrument, hence large collecting power;
- they can carry large currents without dissipating energy hence producing significantly larger magnetic fields, thus higher MDR;
- they can be switched off, which significance will be discussed at page 18.

However, they also have significant limitations:

- they must be cooled below a critical temperature of, usually, a few Kelvin;
- they consume cryogenic fluids, hence limiting the lifetime of the experiment;
- there is a risk of magnet quench.

For these reasons until now cosmic-ray experiments in space have been equipped with permanent magnet and superconducting ones have been limited to fly on stratospheric balloons. Actually, the idea of placing a superconductive magnet in space for cosmic-ray measurements was studied up to the point of becoming proposed experiments. In the eighties the superconducting magnetic spectrometer ASTROMAG [32] was proposed to be used as a facility for cosmic-ray studies. ASTROMAG was planned for the FREEDOM Space Station (FSS) that was under construction and was planned to go into service in 1992. The first experiment planned for the ASTROMAG facility was WIZARD [33] and it was designed to study the energy spectra of cosmic rays with a focus on antiparticles and search for antinuclei. With the cancellation of the FSS in 1991 this cosmic-ray space project was abandoned and later on revised with a new collaboration in the Russian Italian Mission program that led to the PAMELA experiment. Subsequently, NASA selected the Alpha Magnetic Spectrometer for the new space station, the ISS, with a preliminary two-week flight on board a shuttle (AMS-01) [34]. In the original design AMS-02 was equipped with a superconducting magnet later abandoned in favor of a permanent one in the perspective of a significantly longer ($>$ 3 years) mission. Recently, the idea of superconduting magnets is reconsidered for next-generation magnetic spectrometers in space as will be discussed in Section 4.

2.2.2. Calorimeters

An alternative approach to the energy measurement is based on the usage of a calorimeter. Actually, this is the most used technique in balloon- and satellite-borne cosmic-ray experiments. Calorimeters measure directly the particle energy by measuring or sampling the energy deposited by the particle and its, possible, shower secondaries in the apparatus. In cosmic-ray physics both homogeneous (e.g. [35]) and sampling (e.g. [36]) calorimeters were and are used.

Fig. 5 shows a state-of-art calorimeter employed in the experiment DArk Matter Particle Explorer (DAMPE) [37]. DAMPE is a satellite-borne experiment that was launched in space on December 17, 2015, with the scientific goals of studying the cosmic radiation up to tens/hundreds of TeV. It is a homogeneous calorimeter consisting of 14 layers of 22 BGO bars (size $2.5 \times 2.5 \times 60$ cm^3) corresponding to $\approx$ 32 radiation lengths or to $\approx$ 1.6 interaction lengths. The DAMPE calorimeter is representative of recent calorimeters employed in cosmic-ray physics and can be used to study the advantages and disadvantages with respect to magnetic spectrometers. In the energy range of interest, it has an approximately constant energy resolution ranging from $\approx$ 1% for electromagnetic showers to $\approx 30 - -40\%$ for hadronic showers. The energy resolution of the DAMPE calorimeter holds well into the TeV region and, indeed, the energy range is limited by the decreasing, as the energy increases, cosmic-ray statistics more than by the instrumental energy resolution. In fact, the energy range covered by a calorimeter depends on the depth of the instrument that scales logarithmic with the energy of the incident particle. While for magnetic spectrometers, the energy (rigidity) range scales linearly with the rigidity and

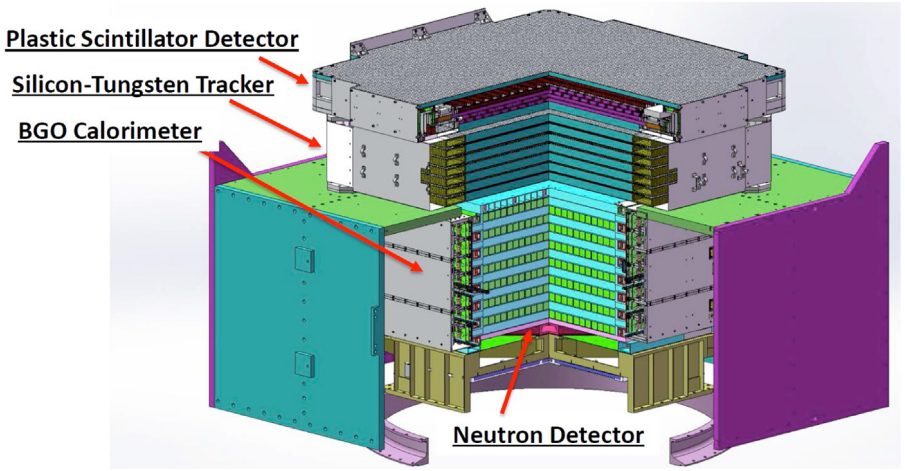

Fig. 5. Schematic view of the DAMPE calorimeter [37].

it depends on the squared track length and on the magnetic field intensity. Therefore, considering that the cosmic-ray energy spectra fall steeply with energy, a calorimeter measurement of a typical cosmic-ray spectrum is less affected by the systematics due to the folding of the energy resolution with respect to a magnetic spectrometer measurement (see Fig. 3).

The acceptance of the DAMPE instrument, a combination of a charge detector, a tracking system, the calorimeter and a neutron detector, is defined by the requirement of containment of the cosmic-ray particles in the calorimeter and is $\approx$ 0.03 m^2 sr slowly varying with energy [37]. Hence, the instrumental acceptance is essentially determined by the geometrical dimension of the calorimeter. In both calorimeter and magnetic spectrometer approaches the instrumental acceptance is a matter of size but an increase in size for a calorimeter is mostly a matter of weight and geometry, while for a superconducting magnet it impacts (it reduces) also the magnetic field intensity. This results in a reduction in the rigidity resolution unless a different magnetic technology is used to produce a comparably strong magnetic field.

Moreover, novel approaches to calorimeters have been proposed to increase their acceptance in space-borne experiments. Fig. 6 left shows the CaloCube project [38] consisting in a homogeneous isotropic calorimeter with a possible configuration of $20 \times 20 \times 20$ scintillating crystal cubes. With appropriate electronics (Fig. 6 right), the calorimeter can accept particles from all direction with the possible exception of one surface dedicated to mechanical support structure. Choosing crystal cubes of CsI(Tl) of side 3.6 cm, the projected total depth of CaloCube is 39 radiation lengths or 1.9 interaction length with a geometrical acceptance of $\approx$ 10 m^2 sr [39]. Such an approach maximizes the useful geometry while keeping good energy resolution and, thanks to the high granularity, providing excellent shower imaging useful for both leakage correction and electron/hadron separation (more on this in Section 2.3). Considering the relatively constant energy resolution and relatively large geometrical acceptance, calorimeters appear as the best solution to study the high-energy ($>$ 100 GeV) part of the cosmic-ray spectrum extending well into the multi-TeV region, potentially approaching the cosmic-ray knee-region.

However, the important point of energy calibration should not be neglected especially because the limited thickness of the calorimeters does not allow the full containment of the particle energies. Moreover, while energy calibration is an issue that affects both magnetic spectrometer and calorimeters, the different energy range achieved by these detectors ($\leq$ 1 TV for magnetic spectrometer, multi-TeV for calorimeters) makes energy calibration at accelerators possible only in a small part of the energy range of interest for calorimeters, differently than for magnetic spectrometers. The extension to higher energies relies essentially on Monte Carlo simulations and resulting systematic uncertainties are often derived from the comparison of different Monte Carlo models. But, as it will be shown in Section 3, sometime these uncertainties seem to be unable to reconcile different experimental results. An in-flight calibration would be highly desirable; however it is not easily achieved due to the difficulties in having independent energy measurements. The AMS-02 [40] and PAMELA [41] experiments were able to cross calibrate their magnetic spectrometers and calorimeters with electrons and positrons, but this cross-calibration was limited to energies of a few hundred GeV and less. Extension to higher energies may be achieved with different approaches that will be discussed in the next section.

It should also be noted that the size and weight of calorimeters like the DAMPE one, which weights $\approx$ 800 kg, or CaloCube, predicted of the order of 1.5–2.0 Ton, cannot be greatly increased because of the severe weight and size limitations for space experiments. Technical and costs constrains for space mission limit the mass of the detectors to the point that, except for the lowest (less than a few GeV) energies, the calorimeters flown in cosmic-ray experiments contained only partially the particle energies. Furthermore, calorimeters have different energy resolution for electromagnetic particles than for hadrons, ranging from percent level in the first case to a few tens of percent for hadronic showers. Thus, for

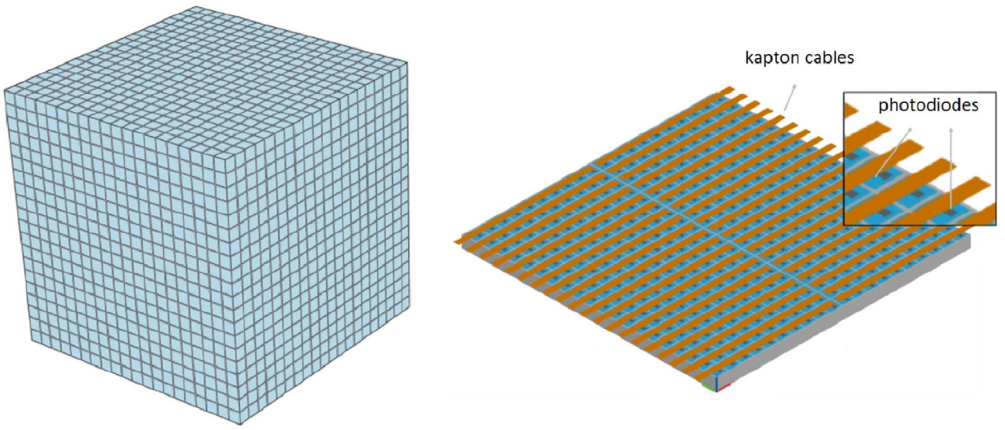

Fig. 6. Left: Possible configuration of the CaloCube calorimeter. Right: one CaloCube layer. The complete calorimeter consists of 20 identical layers [38].

energies of tens of GeV and less magnetic spectrometers are the best choice to study the cosmic-ray energy spectra and their feature. Finally, the sign of the particle charge cannot be measured by calorimeter. Hence, studies of cosmic-ray antiparticles and searches of antimatter have been primarily conducted with magnetic spectrometers (e.g. [25]).

As it will be discussed in Section 2.3, it is important to notice that calorimeters have also been used in cosmic-ray experiments in combination with magnetic spectrometers for energy cross calibration and, especially, particle identification.

2.2.3. Velocity measurements

The energy of a particle can be evaluated also measuring its velocity that, combining this information with the identification of the particle, i.e. mass resolving the particle, allows the derivation of the particle energy. In cosmic-ray experiments the particle velocity was measured either with time-of-flight (TOF) systems in combination with detectors able to measure the trajectory or using effects as ionization losses, transition radiation or Cherenkov light. These velocity-based approaches have been used both as standalone techniques or in combination with other energy measurements.

Deriving the velocity from other effects, like Cherenkov radiation, has been abundantly employed in cosmic-ray studies. Often Cherenkov detectors were used for particle identification (see Section 2.3), however in various experiments Cherenkov counters provided also the only instrumental measurement of the particle energy. The Super Trans-Iron Galactic Element Recorder (SuperTIGER) [42], shown in Fig. 7, is an example, of an experiment employing Cherenkov detectors to identify and measure the energy of cosmic-ray nuclei. The hodoscopes provided the trajectories of cosmic rays, while nuclei were identified combining the charge and velocity measurements derived by the scintillator and Cherenkov detector information. When cosmic rays cross the Cherenkov detectors with a speed larger than the speed of light in the medium (c/n, n refractive index of the medium), Cherenkov photons are emitted with an angle of emission θ_C:

$$\cos\theta_C = \frac{1}{\beta n}. \tag{3}$$

The Cherenkov signal, *Ch*, per unit path length induced by the emitted photons depends on the particle velocity, βc and the medium refractive index as:

$$Ch \propto Z^2\left(1 - \frac{1}{\beta^2 n^2}\right); \tag{4}$$

with Z the particle charge, thus allowing a determination of the particle velocity. In combination with the information from the scintillator counters and hodoscope, the particle can be identified and mass resolved, thus deriving the particle energy. By combining Cherenkov detectors with different radiating materials (aerogel blocks of refractive indexes 1.043 or 1.025 and acrylic of refractive index 1.49) a larger energy range of investigation is achieved, that is from $\approx$ 0.8 to 10 GeV/nuc for cosmic-ray nuclei from Ne ($Z = 10$) to Ba ($Z = 56$) [43].

Another way of using the Cherenkov radiation is to measure the angle in which the photons are produced, hence obtained a more refined evaluation of the particle velocity (Eq. (3)). This is obtained using so-called Ring-Imaging CHerenkov detectors (RICH) [45]. As it will be shown in the next section, RICH detectors have been mostly used in cosmic-ray physics for particle identification, however they were also used for the measurements of cosmic-ray energies. Most notable case is the RICH detector developed by the Chicago University (e.g. [46]) to measure the proton and helium energy spectra from a few tens up to a few hundred GeV/n. The detector used a gaseous radiator filled with nitrogen gas (later on C_4F_{10} gas) and flew on stratospheric balloons a few times in the nineties. The advantage of such an instrument relies

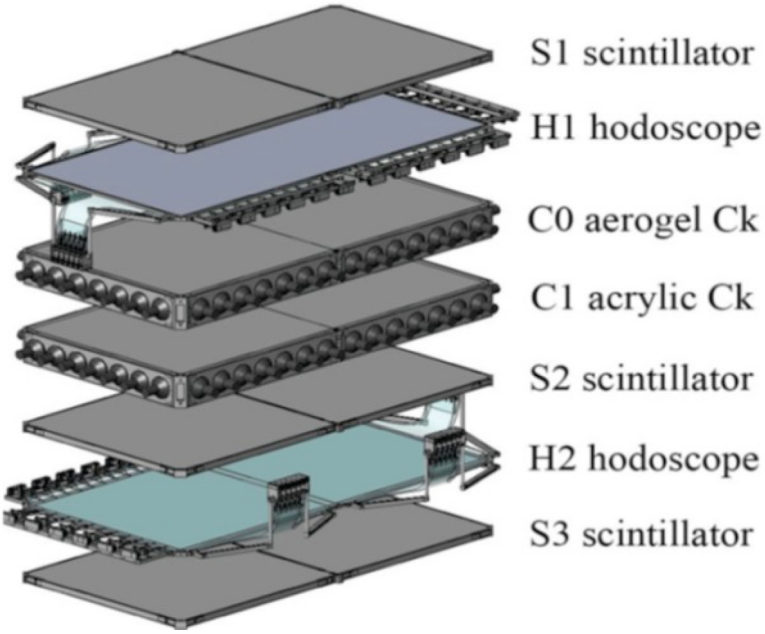

Fig. 7. A module of the SuperTIGER instrument [44].

on the larger acceptance achievable for a given detector weight with respect to magnetic spectrometers. However, the increased availability of space facilities for experiments and progress in the magnetic spectrometers and calorimeters, combined with the difficulties in handling gaseous detectors in space and limited energy resolution, made this technique less attractive and not anymore pursued after these flights.

Since the Cherenkov angle depends on the particle velocity via the Cherenkov relation (Eq. (3)), a Cherenkov detector is not the ideal instrument to measure the speed of very relativistic particles. Instead, a detector (TRD) based on transition radiation process is sensitive only to highly relativistic particles ($\gamma > 10^3$, with γ the particle Lorentz factor). Since its yield, i.e. the number of transition radiation X-rays, is a function of the charge and Lorentz factor of the particles up to a saturation value ($\gamma \approx$ a few thousands), a TRD is an excellent detector for high-energy (several hundred GeV, see next section) particle identification and can be used to measure the energy of particles in a relatively wide energy range. A balloon-borne instrument, called Transition Radiation Array for Cosmic energetic radiation (TRACER) [47], based on this technique had a test flight in 1999 and then flew twice on long-duration balloons in 2003 and 2006. The instrument was equipped with two pairs of scintillator and Cherenkov counters sandwiching arrays of gas-filled, single-wire proportional tubers and layers of plastic-fiber radiators composing the TRD. Actually, TRACER made use of various techniques for the velocity, hence energy, determination. These are shown in Fig. 8: at the lowest energies ($\approx$ 0.5 to 3 GeV/n), it used the Cherenkov signal ("CER" in Fig. 8), while at intermediate energies (up to $\approx$ 400 GeV/n) it used the relativistic rise of the ionization losses ("DEDX" in Fig. 8), finally at energies above $\approx$ 1 TeV/n it used the TRD signal ("TRD" in Fig. 8). Thus, TRACER was able to measure the energy spectra of cosmic-ray nuclei from carbon to iron in the energy range from 1 GeV/n to several TeV/n (it should be noted that this corresponds to total energies of 10^{14} eV for the heaviest nuclei).

Similarly to Cherenkov detectors, TRACER employed light-weight materials that allowed a large geometrical acceptance, $\approx$ 5 m^2 sr [47], making it the largest cosmic-ray detector ever flown. Another advantage in this approach is the possibility to calibrate the velocity/energy response for the whole γ-range of interest at accelerators using singly charged low-mass particles (electrons and pions). The energy resolution depends on the particle charge and for TRACER varied from $\approx$ 15% for boron to $\approx$ 8% for iron [47]. It should be noted that such an approach can be used for in-flight calibration of other techniques, mostly notably calorimeter. A TRD in combination with a large calorimeter were the main detectors for the Advanced Cosmic-ray Composition experiment for the Space Station (ACCESS) to study the energy spectra of individual elements up to the knee region [48]. The experiment was supposed to be installed on the ISS but it never went beyond the proposal phase. Subsequently, this approach was adopted by the balloon-borne Cosmic Ray Energetics and Mass (CREAM) experiment [49]. CREAM flew on long-duration balloon flights several times from Antarctica, once with the combined TRD and calorimeter configuration [50].

2.3. Particle identification

While still very useful, an experimental measurement aimed to the all-particle energy spectrum (i.e. Fig. 1) is not sufficient for a full understanding of the nature of the cosmic radiation. The measurement of the energy spectrum has to be

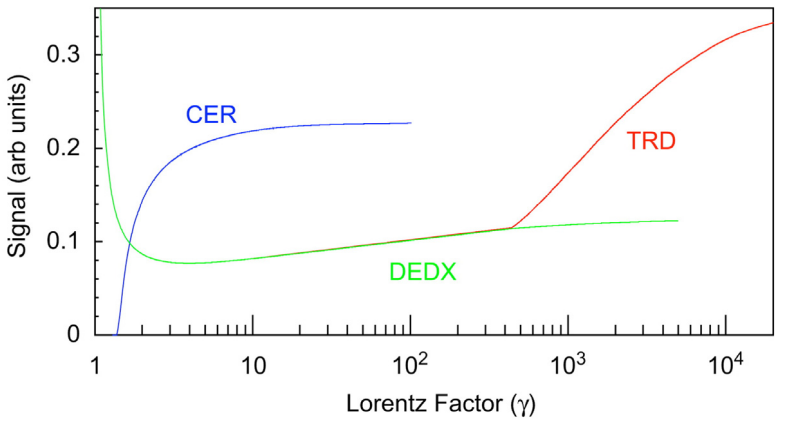

Fig. 8. Energy response of TRACER [47]. See text for more details.

performed for as many as possible cosmic-ray components over the widest energy range to study how the energy spectra vary with chemical composition, if there are and where spectral features. Hence, understanding if there is a common origin and propagation mechanism for the various cosmic-ray components.

The chemical composition of the cosmic rays spans all elements of the periodical table and most of the nuclear isotopes. Therefore, the determination of this composition requires a combination of highly performing particle identifiers. In the following we will examine various recent experimental approaches that produced most of the results that will be discussed in Section 3.

2.3.1. Charge identification

The most basic study of the cosmic-ray composition regards its elemental composition, i.e. the charge measurement. Fundamentally, this is obtained using the theoretical dependence (Bethe–Block formula) of ionization losses from the particle charge, i.e.:

$$\frac{dE}{dx} \propto Z^2.$$

This dependence can be clearly seen in Fig. 9 that shows the ionization losses (dE/dx) measured by the scintillator counters of the time-of-flight system of the PAMELA apparatus as a function of measured rigidity of cosmic rays recorded over one-year period. The ionization losses are shown in MIP (the energy lost for a minimum-ionizing particle) units. The bands corresponding to the elemental species from hydrogen to oxygen can be clearly distinguished as following the square charge dependence at high energies. Considering the relative abundances of the cosmic-ray elements, a charge resolution (σ_Z) of about 0.2 charge unit is sufficient to clearly resolve the various elemental species (e.g. [42]). up to very high energy (> 1 TeV), as for example done by the DAMPE experiment, with the only limitation due to statistics.

Additionally, detectors developed to measure particle were also used for charge identification. Eq. (4) shows the relation between the Cherenkov radiation and the particle charge, making Cherenkov detectors excellent charge discriminators. This information was, for example, used by the SuperTIGER apparatus that, comparing the ionization loss information from the scintillator counters and the Cherenkov signals, properly corrected for the track lengths with the particle trajectory information obtained from the two hodoscopes, was capable to derive the particle charge in the range $Z = 10 - Z = 56$. Likewise, properly detecting the intensity of the transition radiation allows charge identification with TRDs. Combining this with the information from the other detectors, TRACER experiment was able to identify nuclear species in the range $Z = 5 - Z = 26$.

2.3.2. Isotope separation

Observing the low rigidity part of the ionization losses distribution (Fig. 9), a strong dependence to the particle velocity ($\sim \beta^{-2}$) of the energy loss can be observed. Comparing the energy losses at the same rigidities brings out the isotopic composition of the various elements (hydrogen and helium in figure). This leads to the next issue in particle identification: resolving particles with the same charge but different masses. This allows to address questions concerning the propagation of cosmic rays in the Galaxy. In fact measurements of nuclei like the radioactive "clock" ^{10}Be provide strong constrains on cosmic-ray propagation models. Isotopic separation can be achieved measuring the ionization losses and stopping range of cosmic rays in the instrumentation. Fig. 10 shows the capability for nuclear and isotopic reconstruction of the satellite-borne experiment NINA [52]. The NINA apparatus operated in space from July 1998 to April 1999, followed by a twin instrument, NINA-2 [53], that operated from July 2000 to August 2001. The experiment measured the galactic, solar and anomalous components of the cosmic radiation in the energy range 10–200 MeV/n. The instrument consisted of 16

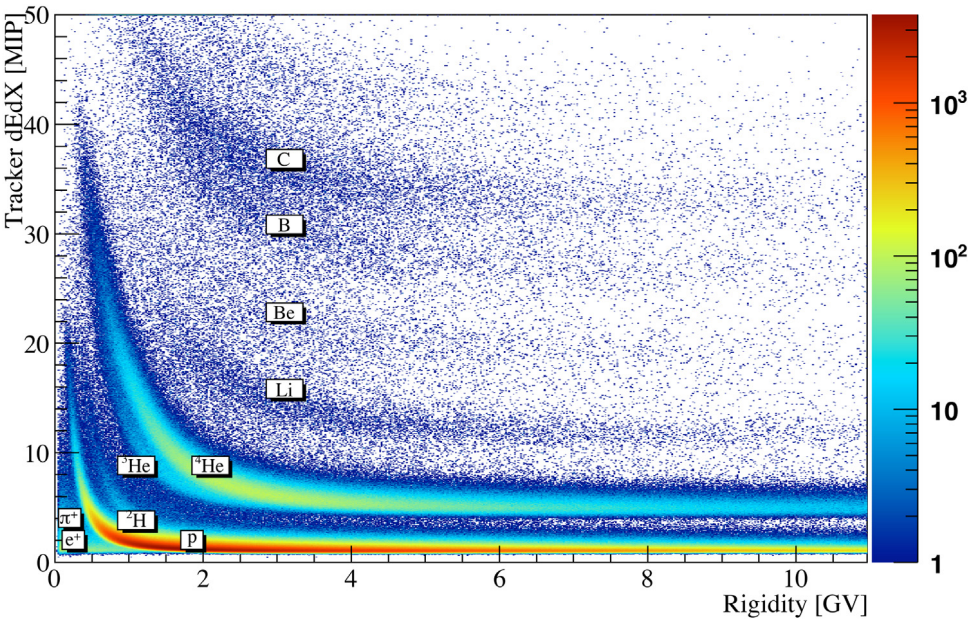

Fig. 9. Ionization loss distribution as a function of rigidity for cosmic rays measured by the PAMELA apparatus.

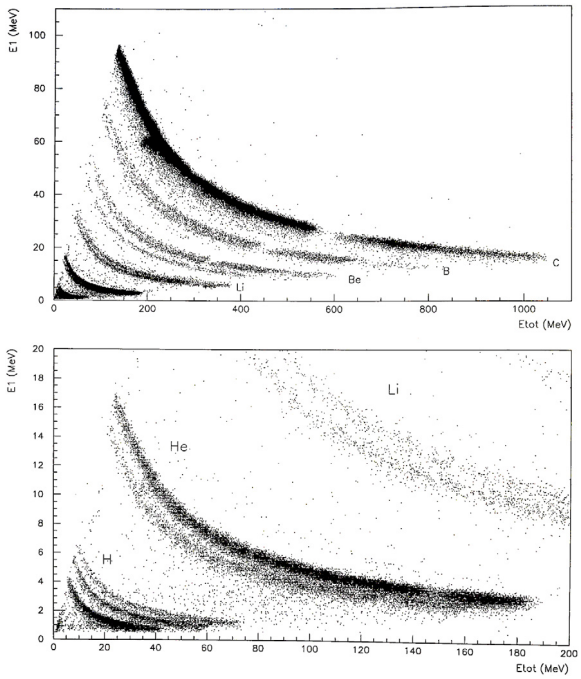

Fig. 10. Top panel: distribution of the energy released in the first plane (E_1) versus the total energy (E_{tot}) detected by the NINA apparatus for particles produced in the fragmentation of ^{12}C produced at the GSI test beam facility [51]. Bottom panel: an expanded view for the lightest nuclei.

planes composed by two 6 × 6 cm^2 silicon detectors. Each silicon detector was segmented in 16 strips with alternating orientation, thus providing X and Y coordinates. The detectors were 380 μm thick, except the first pair that was 150 μm thick. The support structure run around the lateral strips 1 and 16, hence a particle going through the instrument was crossing only sensitive material. Selecting only cosmic rays that entered and stopped inside the apparatus, a calorimeter measurement of the total energy of the particles was achieved. Consequently, this determined the energy range over which cosmic rays were measured. Together with the total energy, the instrument made several measurements of the ionization losses hence sampling the slow down of the particle. From this, charge and mass of the particle could be derived either

comparing the ionization losses to theoretical expectation (e.g. Bethe–Bloch formula) or using the method of the residual range shown in Fig. 10. By comparing the energy lost in the first plane (two silicon detectors) with the total energy, the chemical composition of the particles was derived as it is evident in the figure. A similar approach was used by the Cosmic Ray Isotope Spectrometer (CRIS) on board the Advance Composition Explorer (ACE) spacecraft [54]. ACE was launched in 1997 and placed at the L1 Lagrange point, hence outside the influence of the Earth magnetosphere. CRIS was designed to study the chemical composition of both the solar and galactic components of the cosmic radiation from lithium to zinc in the energy range 50–500 MeV/n. It consisted of scintillating fiber hodoscopes for trigger and particle trajectory reconstruction and multiple layers of silicon detectors. As in the case of NINA, only particles contained in the instrument were selected and their energy and composition were derived from the multiple energy loss measurements.

This approach performs best up to several hundred MeV/n, the extension to higher energies has been obtained employing other methods. As discussed in Section 2.2.3, various techniques can be used for velocity measurements and, when combined with complementary information, they can be used for the identification of the nuclear species. For example the Isotope Magnet Experiment (ISOMAX, a balloon-borne experiment that unfortunately flew only twice since it was permanently damaged on the second flight) [55] used precise time measurements for the isotopic identification. The apparatus consisted of a magnetic spectrometer equipped with drift chamber tracker, three-layer time-of-flight system and two silica–aerogel Cerenkov counters. The scientific goal of the experiment was the measurement of the light nuclei isotopes, with a focus on ^{10}Be, up to about 2 GeV/n that was achieved also thanks to a time TOF resolution of 60 ps for beryllium [55]. Higher energies were achieved measuring the velocity via the Cherenkov effect. The Cosmic Antiparticle Ring-Imaging Cerenkov Experiment (CAPRICE98) [56] flew on a stratospheric balloon in 1998. It was a superconducting magnetic spectrometer equipped with three gaseous drift chambers as tracking device, a TOF system, an electromagnetic calorimeter and a 1 m tall RICH detector, with radiator C_4F_{10} gas. The experiment was designed for antiparticle studies, however the low refractive index of the radiator ($n = 1.0014$) allowed the isotopic separation of the hydrogen nuclei, measuring the deuteron flux between 12 and 21 GeV/n [57]. Data on the isotopic composition of light cosmic-ray nuclei will also be provided by the AMS-02 experiment. Equipped with a Cherenkov detector made up by two different radiators (sodium fluoride, $n = 1.33$ and aerogel, $n = 1.05$) AMS-02 should be able to identify, for example, deuterons up to ≈ 5 GeV/n.

2.3.3. Discrimination of $Z = 1$ particles

In Fig. 9 it can also be noticed the presence of minimum ionizing particles at the lowest rigidities. These are particles lighter than protons like positrons and, less abundant, positive pions (these pions are produced locally by the interaction of cosmic rays with the satellite). In fact, cosmic rays include various charge one particles both of Galactic and local, produced by cosmic rays interactions in the proximity of the apparatus or in the Earth's atmosphere, origin. Indeed, it should not be forgotten that present-day particle physics originated from cosmic-ray observations in the first half of the twentieth century. As seen in Fig. 9, ionization losses can be used to identify different charge one particles. However, one point that it should be made clear is that particle identification requires the combination of various experimental techniques. This is especially true when searching for rare components as is the case of charge one particles but protons. Besides the study of deuterium previously discussed, these studies concern primarily the measurement of the electron and of the antiparticle components.

Antiparticles (antiprotons and positrons) are a natural component of the cosmic radiation being produced in the interaction between cosmic rays and the interstellar matter. These antiparticles have been observed in the cosmic radiation and they have been shown to be extremely interesting for understanding the propagation mechanisms of cosmic rays. Furthermore, novel sources of primary cosmic-ray antiparticles of either astrophysical or exotic origin can also be probed as it will be discussed in Section 3. However, antiparticles amount to just a tiny fraction of the cosmic radiation. Positrons are about ten percent of the electron (e^-) component and a few per mill of the proton component above a few GeV, while antiprotons are $\approx 10^4$ times less abundant than protons. And heavier antiparticles like cosmic-ray antideuterons (expected but not yet observed) are orders of magnitude even less abundant than cosmic-ray antiprotons. This places stringent requirements on the experimental instrumentation and subsequent data analysis.

A fundamental ingredient in these studies is the measurement of the sign of the charge. This has been mostly obtained measuring the direction and sign of curvature of the cosmic rays inside a magnetic spectrometers. Other approaches employed made use of effects due to the magnetic field of the Earth like the East–West asymmetry (e.g. [58,59]) and the variation of the "Moon shadow" (e.g. [60]) or by inferring the antiproton component from the muon charge ratio at sea level [61]. However, these alternative approaches cannot compete with the precision achieved by magnetic spectrometers. As for the energy/rigidity measurements, the sign-of-charge identification is limited by the MDR of the magnetic spectrometer. Considering that there are 10 times more electrons than positrons and 10^4 more times protons than antiprotons a misidentification of the charge sign (so called "spillover") will fundamentally affect the results. This can be seen in Fig. 11 that shows the deflection distribution measured by the PAMELA magnetic spectrometer for positively- and negatively-charged down-going particles that did not produce an electromagnetic shower in the calorimeter. It can be clearly see that positive particles (proton) spill into the negative side for very low deflection (very high rigidities) hence limiting the highest energy/rigidity up to which antiprotons can be safely detected. In the case of the PAMELA experiment this amounted to about one third of the MDR [62], similarly for the AMS-02 experiment [63]. Hence, extreme care has to be taken in determining the spectrometer resolution and, from this, estimate the spillover background as

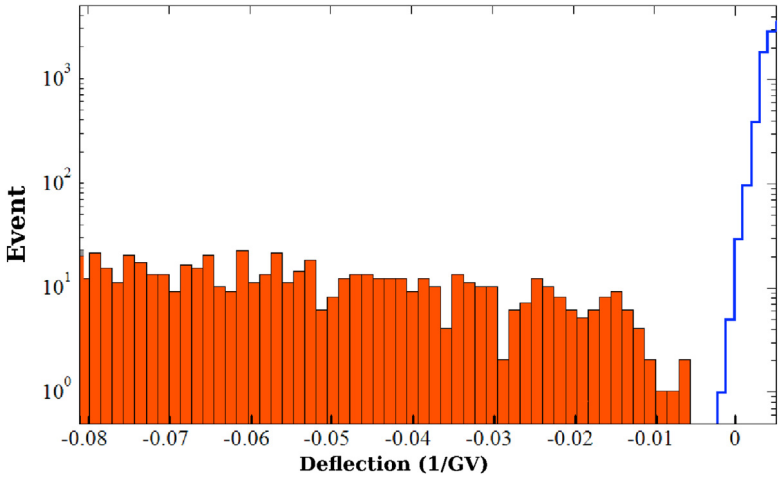

Fig. 11. The deflection measured by the PAMELA magnetic spectrometer for negatively- and positively-charged down-going particles and that did not produce an electromagnetic shower in the calorimeter.

the rigidity increases. This requires an in-flight estimation of the spatial resolutions of the tracking layers with their dependence on particle directions, of the positions in space of the tracking layers (tracking alignment) and a continuous monitoring of the magnetic field intensity over time. Various approaches can be adopted for this in-flight calibration (e.g. [63]). For example, the rigidity can be compared with the energy measured by other detectors, especially powerful is the comparison of the rigidity measured for electrons and positrons and the corresponding energy measured by a calorimeter. In this case strong constrains on the tracker alignment can be derived (e.g. see Supporting Online Material of [64]). If the magnet is superconducting and it is environmentally feasible, it can be switched off at the end of the mission allowing a maximum precision measurement of the alignment [65]. Subsequently, this in-flight calibration is usually combined with a detailed simulation of the in-flight performances of the tracking system to determine the most appropriate tracking requirements and to estimate the rigidity-dependent residual spillover background. Test beam on ground are very useful for performance studies of the magnetic spectrometer and for proper tuning of the simulations. However, the shocks during the launch and orbit placement operations as well as the space environmental conditions do not allow a straightforward utilization of the calibration and alignments performed on ground.

However, a clean measurement of the charge sign is fundamental but not sufficient for a reliable estimation of the antiparticle components. In the case of antiprotons, a significant (about two order of magnitude larger) electron background remains, while the positive side is dominated by protons that exceed the positrons component by more than three orders of magnitude above a few GeV. Therefore, additional information has to be used to complete the identification process. Fig. 12 exemplifies the identification of cosmic-ray antiprotons. It shows the reciprocal of the particle velocity as a function of rigidity as measured in the BESS-polar II experiment. Because of a residual atmosphere above the payload, muons resulting by the interaction/decay chain of cosmic rays with the atmosphere represented an additional background for the measurement. Also for this reason, the apparatus was equipped with Cherenkov counters that were used to reduce the relativistic components (muons and electrons) up to 3.5 GeV. The residual background of this component can be seen showing up on the negative side at rigidities around 1 GV. Then, the final identification is performed selecting events according to their velocity, the solid lines indicate the band of inclusion for antiprotons. Hence, a clean identification of antiprotons can be performed up to a few GV considering, also, that an instrumental MDR of 240 GV assures that no spillover protons contaminate the sample. Identification at higher rigidities can be reached employing different technique for velocity measurements or using calorimeter information. The PAMELA experiment used the calorimeter information to identify electrons with extremely high efficiency and reject them (e.g. [62]). AMS-02 experiment adopted a similar approach but combined velocity information from its TOF system, Cerenkov detectors and TRD, see [63].

Conversely, the detection of electromagnetic showers in a calorimeter becomes a powerful tool for electron and positron identification. As previously stated, positrons amount to about 10% of the electron component which total less than 1% of the cosmic-ray protons, decreasing as the energy increases. Therefore, a rejection power of $\sim 10^4$ and $\sim 10^5$ is required for a clean electron and positron identification, respectively. Fig. 13 shows two cosmic-ray events: an electron (no sign of charge separation, hence it could be a positron) and a proton both with measured deposited energies of $\approx$ 3 TeV by the space experiment CALorimeter Electron telescope (CALET) [67]. CALET was launched on August 19, 2015, and then installed on the ISS. Since then, it has been collecting cosmic-ray data with a focus on the measurement of the electrons (sum of e^- and e^+) up to 20 TeV and nuclei ($Z = 1-40$) up to 1 PeV in total energy. CALET is conceptually similar to DAMPE, it consists of two layers of plastic scintillators for charge identification, an imaging calorimeter composed by scintillating fibers interleaved with tungsten planes and a homogeneous calorimeter made of

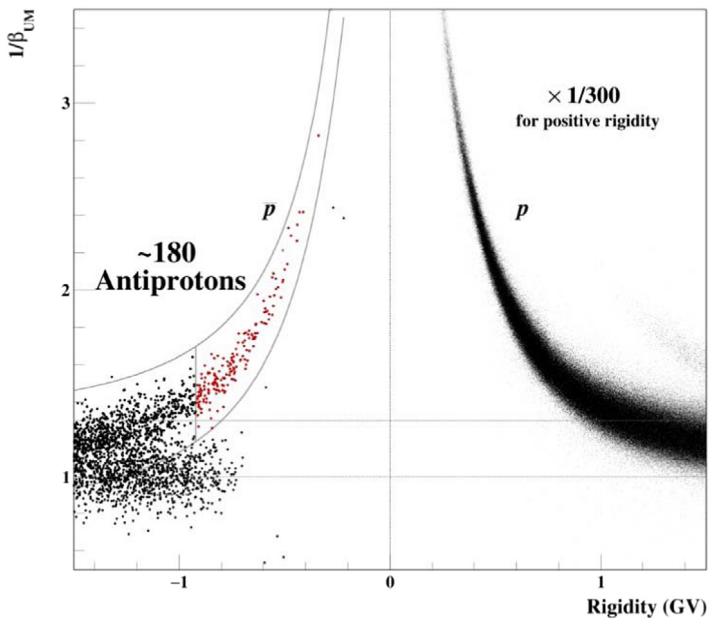

Fig. 12. The distribution of the reciprocal of the velocity in units of c versus rigidity measured by the BESS spectrometer [66]. The solid lines indicate the antiproton selection. For clarity, only 1 in 300 positively-charge events are shown.

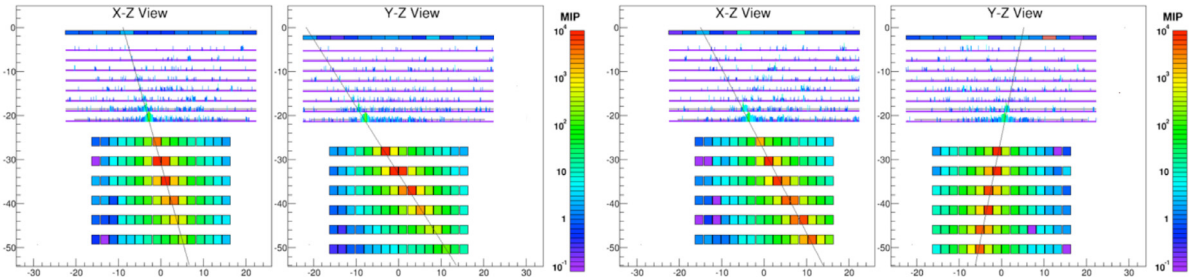

Fig. 13. A electron (left) and a proton (right) event recorded in space with deposited energies of about 3 TeV by the CALET experiment [69].

lead tungstate logs. The instrument has a total thickness of 30 radiation lengths and 1.5 nuclear interaction lengths and a geometrical acceptance of $\approx$ 1000 cm^2 sr. The events depicted in Fig. 13 have very similar deposited energy ($\simeq$ 2.89 TeV) but visibly different topology in the calorimeter. By properly combining the energy and topology information electrons can be efficiently (about 80%) identified with a proton rejection factor of $\sim 10^5$ [68]. CALET and DAMPE have extended the all-electron measurements up to the highest energy ($\approx$ 5 TeV) to date. Measurements at higher energies are possible to the extent of sufficient statistics, i.e. sufficiently long period of data taking and sufficiently large geometrical acceptance of the apparatus. The CaloCube concept described in Section 2.2.2 has been proposed to increase to higher energy these measurements and its usage in a future experiment will be discussed in Section 4.

Experiments like CALET and DAMPE measure the sum of the positron and electron fluxes. The separate measurement of the two components was obtained employing magnetic spectrometers together with calorimeters. For example, similarly to the electron identification in CALET and DAMPE, PAMELA and AMS-02 used deep calorimeters to sample the energy and topology of electromagnetic and hadronic showers. By combining the rigidity measurement from the magnetic spectrometer with the energy and topology of the showers in the calorimeter, PAMELA and AMS-02 were able to attain very high proton rejection factors (e.g. $\sim 10^5$, [70]) up to several hundred GeV. Furthermore, using also the information from the TRD, AMS-02 was able to extend the positron identification up to nearly 1000 GeV [71]. However, the extension to higher energies is limited by statistics, as in the case of the all-electron measurements, but also by the MDR of the instrument, that is by an irreducible contamination of spillover electrons. Therefore, as will be discussed in Section 4, a next-generation magnetic spectrometer is required to expand these antiparticle measurements in the TeV region.

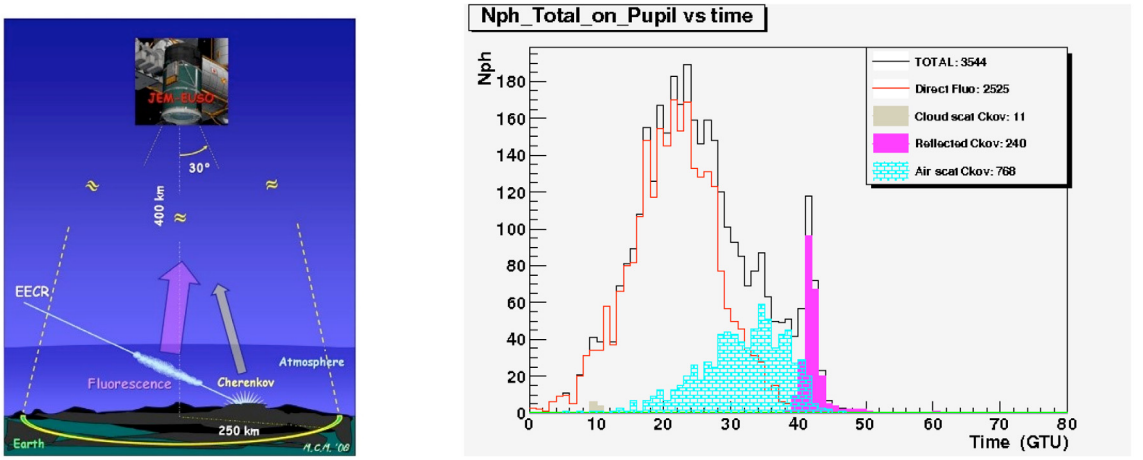

Fig. 14. Left: a schematic view of UHECR detection from space. Right: The time profile of a typical EAS induced by a proton UHECR with an energy of 10^{20} eV and arriving from a 60° zenith angle in case of clear atmosphere.

2.4. UHECR observation from space

The idea to go to space to observe ultra high energy cosmic rays (UHECRs), $E \geq 10^{19}$ eV, looking on darkness to the nadir the fluorescence light produced by extensive air showers (EAS) originated from cosmic rays crossing the Earth's atmosphere, was first proposed by John Linsley in the late 70.ies [72]. In 1995 the Linsley's original idea was taken up by Yoshiyuki Takahashi who developed the concept of MASS, the Maximum-energy Auger (Air)-Shower Satellite, later named Airwatch. The key breakthrough was in the imaging technology with the use of lightweight, unphased, segmented, double Fresnel lens optics to enlarge the field of view (FoV). The MASS idea evolved in U.S. into the Orbiting Wide Angle Light Concentrator (OWL), two satellites with Schmidt telescopes observing the atmosphere in stereo configuration. While Airwatch in Europe became EUSO, the Extreme Universe Space Observatory proposed for a free-flyer to ESA. Selected by ESA and re-oriented as a payload for the Columbus module of the International Space Station, the program was finally canceled for financial constraints in ESA and the Columbia Shuttle accident. In 2006, the Japanese and US teams, under the leadership of Yoshiyuki Takahashi, redefined the mission as an observatory attached to KIBO, the Japanese Experiment Module (JEM), named JEM-EUSO [73].

The most relevant advantage of space based observations of UHECRs is the extremely large instantaneous observational area that can be monitored from space compared with the on-ground arrays, two orders of magnitude larger than the Pierre Auger Observatory in case of JEM-EUSO. A second relevant feature of the space approach is the highly uniform exposure over the full sky. Space observations cover a 4π sky by the same instruments, assuring identical experimental performance for southern and northern hemispheres. A disadvantage of the space-based experiments is the detection time, due to their operation only in the dark.

The observation from space of UHECRs is based on the measurements of fluorescence and Cherenkov photons produced in EAS phenomena. An UHECR, hitting the atmosphere, produces secondary particles that, in turn, collide with the air atoms producing a long shower largely dominated by negative and positive electrons. The number of particles is related to the energy of the primary particle (about 10^{11} for a primary particle of energy $E \sim 10^{20}$ eV). Crossing the atmosphere, the electrons excite metastable energy levels in atmospheric atoms and molecules, especially nitrogen. These atoms return to the ground state in a short time, emitting characteristic fluorescence light that, in air, lies in the ultraviolet (UV) band with wavelengths between 300 and 400 nm. This light is isotropic, and its intensity is proportional to the energy deposited in the atmosphere. The EAS thus forms a streak of fluorescence light along its path in the atmosphere, depending on the energy and zenith angle of the primary particle. In addition, many secondary particles have velocities higher than that of light in air, thus emitting Cherenkov photons, highly beamed within a cone of $< 1°$ of aperture along the trajectory. Part of these photons can be scattered by the molecular and aerosol content in the atmosphere and by the clouds.

Looking downward at the Earth's atmosphere in the dark, a specifically designed space telescope can, step by step, detect such fluorescence light emitted along the shower's evolution path, as shown in Fig. 14 left. At any atmospheric depth, the recorded amount of light is nearly proportional to the shower size at that point. By imaging the motion of the streak every few microseconds, it is possible to define the arrival direction of the primary cosmic ray. The integral of recorded light allows to determine the energy of the primary UHECR. The shape of the shower, especially the position of the shower maximum, Xmax, in the traversed slant depth, has different values for different particles with the same energy. Hence, it gives information about the nature of the primary constituents.

The time profile of a typical EAS induced by a proton UHECR with an energy of 10^{20} eV and arriving from a 60° zenith angle in case of clear atmosphere is shown in Fig. 14 right for a telescope as JEM-EUSO installed on the ISS. The vertical

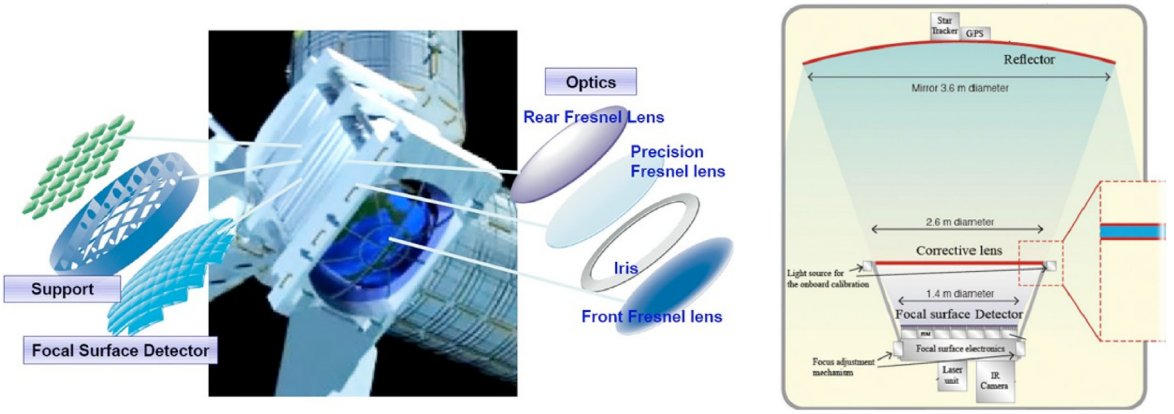

Fig. 15. Left: the JEM-EUSO apparatus. Right: the K-EUSO telescope.

axis denotes the number of photons reaching the optical system. The black line represents all photons. The fluorescence component is shown by the red histogram. Cherenkov photons are indicated by the cyan and magenta shaded histograms for the components scattered in the atmosphere and diffused from the surface, respectively. The sharp peak at the end of the profile is the so-called Cherenkov mark due to the Cherenkov photons reflected from the impact point. Identification of such a mark helps locating where EAS has landed. Another characteristic parameter of UHECR experiment is the exposure time, which is the acceptance of a detector convoluted with the fraction of time in which the detector is sensitive to the EAS detection. A further advantage for the experiments in space is the large and well monitored distance between the instrument and the location of the EAS. The track length of an EAS is in fact constrained at $\sim 10 - 20$ km, rather small compared with the usual orbits of satellites or ISS. In addition, space-based telescopes have the possibility of observing in many cloudy conditions since, in most cases, the maximum of the shower occurs above the cloud-top.

2.4.1. UHECR space instrumentation

The objective of a UHECR space experiment is the detection of cosmic rays at energies at which ground experiments start running out of statistics. However, detection of cosmic rays with energies lower than 10^{19} eV is highly desirable providing data overlapping with on-ground measurements. To achieve this goal while complying with the typical constraints of power, mass, size and bandwidth of space detectors, numerous novel technologies from optics to sensors, across front-end and read-out electronics have been developed over the years. The energy of the primary particle, its nature and arrival direction are the fundamental quantities to be measured in an UHECR experiment. The basic instrument is a telescope composed by an optical system that focuses the light onto detectors placed in the focal surface.

JEM-EUSO, now renamed Joint Experiment Missions — Extreme Universe Space Observatory, and K-EUSO (KLYPVE-EUSO) telescopes, both designed for installation outside the ISS, use two different imaging techniques, suitable to collect photons in the 330–400 nm (UV) band at any pixel of a focal detector. Other space experiments employing these technique are discussed in Section 3.

The JEM-EUSO telescope represents the effort made by the JEM-EUSO collaboration to comprehensively design a next-generation experiment for the study of very high energy cosmic rays and to reach a very high Technology Readiness Level. Unfortunately, the mission has been frozen by the Japanese Space Agency (JAXA), leader of the project, consequently a few years back the JEM-EUSO team reoriented the program, while preserving the same objectives. However, the work made has been the technological and scientific basis of the successive missions in space or on stratospheric balloons conducted by the collaboration. A model of the JEM-EUSO instrument is shown in Fig. 15, left. It consists of a Fresnel-optics refractive telescope that focuses light onto a large Focal Surface (FS). It has been studied for many years, and several related pathfinders have been constructed and launched by stratospheric balloons or installed inside the ISS. Currently, JEM-EUSO represents the most updated project for the study of UHECRs from space. JEM-EUSO optics consists of two curved, double-sided Fresnel lenses with 2.65-m external diameter, as well as of an intermediate curved precision lens (Fig. 15 left) All lenses are made of PolyMethyl Methacrylate (PMMA) material, which has high UV transparency over the wavelength range from 330 to 430 nm. The first lens is arranged to face space, the second lens is used to reduce chromatic aberration. The two sides of this lens are characterized by a Fresnel surface acting as a "field lens", which is able to reduce the spot size, and a diffractive surface to reduce chromatic aberrations. The aberrations are due to the variation in the refractive index of the lens, caused by a rather large emission range in nanometers of UV photons from nitrogen molecules of the atmosphere. The third lens focuses light onto the focal surface. A stop (Iris) between the first and second lens defines the Entrance Pupil Diameter on axis. Looking downward from the ISS, the combination of these three Fresnel lenses returns a full angle field of view of 60° with a resolution of 0.075°, corresponding to a pixel of about 550 m on Earth.

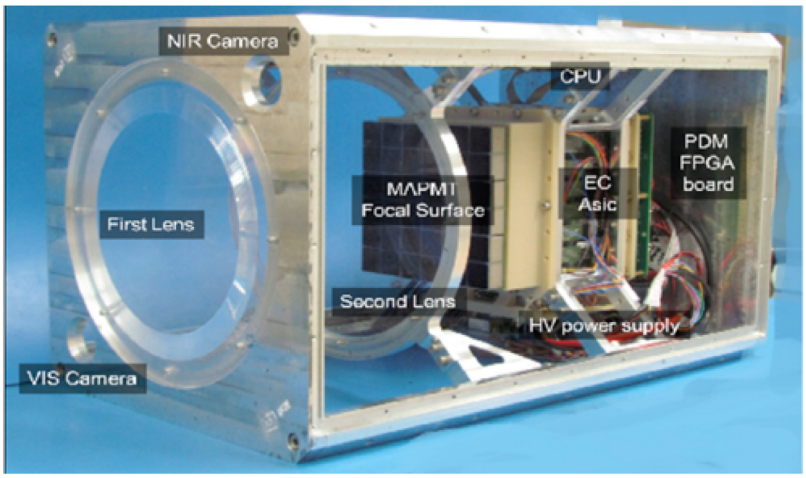

Fig. 16. The Mini-EUSO apparatus.

The proposed focal surface consists of 4932 64-channel multianode photomultipliers (PMs) working in a single-photon counting in the range 290–430 nm. They are organized in elementary cells of 4 PMs each and in 137 photo-detection modules (PDM) of 9 elementary cells each. The electronics process triggers for cosmic ray air-shower or other transient events in the atmosphere and send data to the ground for further analysis. It can also observe the signal of the forward-beamed Cherenkov radiation diffusively scattered from the Earth's ground or from the cloud's tops, which marks the core location of the shower. Using the recorded images, the energy and the arrival direction of the UHE primary are determined. Its yearly exposure time is close to an order of magnitude larger than the Pierre Auger Observatory one. A review of the JEM-EUSO mission can be find in [74]. K-EUSO [75] is a Schmidt telescope covering a FoV of 40°. The scheme is shown in Fig. 15, right. It is under construction and is planned to be attached to the Russian MRM-1 module on-board ISS in 2022 and to operate for minimum of 2 years up to more than 6 years if the lifetime of the ISS will be extended. The telescope comprises a 4 m diameter refractive mirror with a 1.7 m focal length, a corrective lens of 2.5 m, and a spherical focal surface concentric with the mirror. The aperture stop is placed on the frontal surface of the corrective plate. The nominal spot size is well inside the dimension of a pixel (3 mm) of any multi-anode photomultiplier tube in the focal surface, providing an angular resolution higher than 2 mrad. Looking downward from the ISS orbit, this corresponds to a ground resolution of about 750 m. The focal surface of K-EUSO, equipped as in JEM-EUSO, but wide less PDMs, has a concave shape with a diameter of 1.27 m and a radius of curvature of 1.7 m.

A test of the capability of Schmidt optics and Fresnel lenses to detect UV signals in the atmosphere at orbit altitude has been performed by two other space missions dedicated to UHECR studies. These are two small telescopes, TUS and Mini-EUSO, that are already providing scientific data, the first on board satellite, the second inside the ISS.

TUS (Track Ultraviolet Setup) [76] is a space mission led by the SINP Institute of the Moscow State University and the first orbital detector designed to detect UHECRs from space. Launched on April 28, 2016 on board of the Lomonosov satellite at an altitude of 470–500 km, the instrument was active until November 2017. The telescope worked in the near UV band and consisted of a modular Fresnel mirror-concentrator with an area of 1.93 m^2 and a focal area equipped with 256 PMTs. The observed ground area was of $\sim 80 \times 80$ km^2.

Mini-EUSO [77,78], shown in Fig. 16, is a small UV telescope that has been carried to the ISS by a Soyuz the 26th of August 2019 and installed in front of the UV transparent window of the Russia's Zvezda module looking down on the Earth. The instrument was switched on in October 7, 2019, and should operate with a sequence of running shifts for at least three years. The telescope has dimensions of $37 \times 37 \times 62$ cm^3 and a weight of 28 kg. The field of view is $\pm 22°$. The optics is made of two 25 cm diameter PMMA Fresnel lenses, one of them double sided, sided, which focuses light onto one JEM-EUSO-like PDM module. The instrument is equipped also with two ancillary cameras for complementary measurements in the near infrared (1500–1600 nm) and visible (400–780 nm) range and with a 8×8 SiPM imaging array for testing this technology in space. Mini-EUSO maps the Earth in the UV range (290–430 nm) with a spatial and temporal resolutions of ~ 6 km and 2.5 μs, respectively.

All these space instruments provide also a global observation in the UV band of atmospheric phenomena as UV nightglows, lightning, plasma discharges, transient luminous phenomena (TLE), such as blue jets, sprites and elves, events that occur in the upper atmosphere. Moreover, they will detect meteors and meteoroids traces in the near UV, will give access to studies of terrestrial and marine surfaces in the UV range, oceanography and sea–atmosphere interactions, marine biology. Finally, these devices could track debris in space, allowing the use of laser ablation for their removal.

Finally, it is worth to note that a space experiment designed for the detection of UHECRs needs to monitor the atmospheric background in which the UV telescope works. An Atmospheric Monitor System generally consists of an

infrared camera, a LiDAR (Light Detection and Ranging) device, and a sample of data from the main telescope in order to measure the cloud top with good accuracy (better than 500 m for JEM-EUSO).

2.4.2. The UHECR stratospheric balloon program

A test of the potential of the developed technology to detect and reconstruct extensive air showers induced by ultra high energy cosmic rays from the edge of space has been performed with stratospheric balloon missions with increasing level of performance, upgraded designs and flight duration. Furthermore these missions provide first results on UHECR and related atmospheric physics. Two balloon flights have been performed so far: EUSO-Balloon (Canada, 1 night) and EUSO-SPB1 (Pacific Ocean, 12 nights). A third one (EUSO-SPB2) is under preparation.

EUSO-Balloon was launched by the French Space Agency (CNES) from the Timmins base in Ontario, Canada, on the moonless night of August 25, 2014 to a floating altitude of $\sim$ 38 km [79]. EUSO-Balloon imaged the UV intensity in the wavelength range 290–430 nm for more than 5 h before descending to ground. The refractor telescope, inserted in a gondola, consisted of two, 1 m^2, PMMA plastic Fresnel lenses focusing light from below onto the 2304 pixels of a UV sensitive high speed JEM-EUSO PDM . The full FoV in nadir mode was $\sim 11^\circ$, while the spatial and temporal resolutions of the detector were 130 m and 2.5 μs, respectively. An infrared camera was installed to monitor the atmospheric conditions in the field of view of the instrument, in particular the optical thickness and altitude of the clouds. The main objective of the mission was the measurement of the intensity of the UV radiance from the Earth atmosphere and ground in different conditions.

The main object of the second balloon-flight of the JEM-EUSO collaboration, EUSO-SPB1 [80,81], was to detect very high energy cosmic rays from the edge of space. The telescope was an upgraded version of the instrument used in the EUSO-Balloon mission, with two, 1 m^2, PMMA plastic Fresnel lenses and a JEM-EUSO-like Photo-Detector Module (PDM) in the focal surface. In addition to the main UV camera, EUSO-SPB flew with two auxiliary systems: a detector made of two IR with different band-pass filters to monitor the clouds and a supplementary UV camera equipped with SiPMs (Silicon Photo-Multipliers) to test this technology in space conditions in the context of indirect detection of UHECRs. An autonomous internal trigger was implemented to detect UHECRs. EUSO-SPB1 was launched April 25, 2017 at an altitude of 33 km on a NASA Super Pressure Balloon from Wanaka, New Zealand, for an expected flight of few months. Unfortunately, the flight was terminated prematurely in the Pacific Ocean about 300 km SE of Easter Island after only 12 days and 4 h aloft, due to a leak in the carrying balloon. The instrument was lost together the detected data that were stored in a hard disc. Therefore the only data analyzed were the transferred ones with the antenna. No EAS track was clearly identified, in agreement with 1 event expected from simulations.

An upgraded version of EUSO-SPB1, named EUSO-SPB2, is currently under construction, and is also planned to be launched on a NASA Super Pressure Balloon in 2022 from Wanaka, for a flight of several months. Main objective of EUSO-SPB2 is to perform observations of UHECRs at the edge of space by the UV fluorescence technique. Alongside this target, the mission will explore PeV cosmic rays by the direct Cherenkov technique from near-orbit altitude, and will measure neutrino optical background signatures by looking below the Earth's limb. It will test the features of the next generation space mission POEMMA (Probe of Extreme Energy Multi-Messenger Astrophysics) that will be discussed in Section 4. EUSO-SPB2 payload will comprise 2 Schmidt telescope, each equipped with a glass spherical mirror with a 1.66 radius of curvature, with an entrance pupil of a 1 m of diameter. The field of view of each telescope will be $40^\circ \times 11^\circ$. One telescope will be dedicated to UHECR measurements using the fluorescence technique. The Focal Surface will be equipped with 3 JEM-EUSO like PDMs to increase the UHECR detection power, while a temporal resolution of 1 μs will allow to lower the energy threshold of the instrument at about 3×10^{18} eV. The second telescopes will detect the Cherenkov emission in air by EASs generated by UHECR with an energy threshold of 10×10^{16} eV. The Focal surface for this telescope will be based on SiPM sensors with a new dedicated electronics. The second telescope will point partially below the limb to test the capability to detect the beamed Cherenkov signal produced by the up-going EAS generated by τ-lepton decays produced by neutrino–tau interactions in the Earth. Observations above the limb to study UHECRs through their Cherenkov emission are also in its field of view.

3. A new era of precision measurements of cosmic rays in space

In Section 2 the physical quantities relevant for cosmic-ray studies were discussed together with the experimental approaches that were employed to measure them. In this section the current science of cosmic rays will be addressed using the most recent scientific results. As per topic of this work, the focus will be on results obtained with space instruments.

3.1. The heliosphere and its influence on the cosmic radiation

The near totality of space instruments operated and are operating deep inside the heliosphere. This implies that the Sun activity and its effects on the cosmic rays must be taken into consideration for a proper understanding of the experimental measurements. In fact, the Sun both modulates the cosmic-ray intensity via its solar wind and contributes to the particle spectra with energetic particles emitted during solar events. This last topic goes beyond the scope of this work and will not be further discussed here (for a summary of the field excellent reviews are available, e.g. see [82]). In this section, our understanding of the effects of the Sun on the galactic cosmic rays will be discussed.

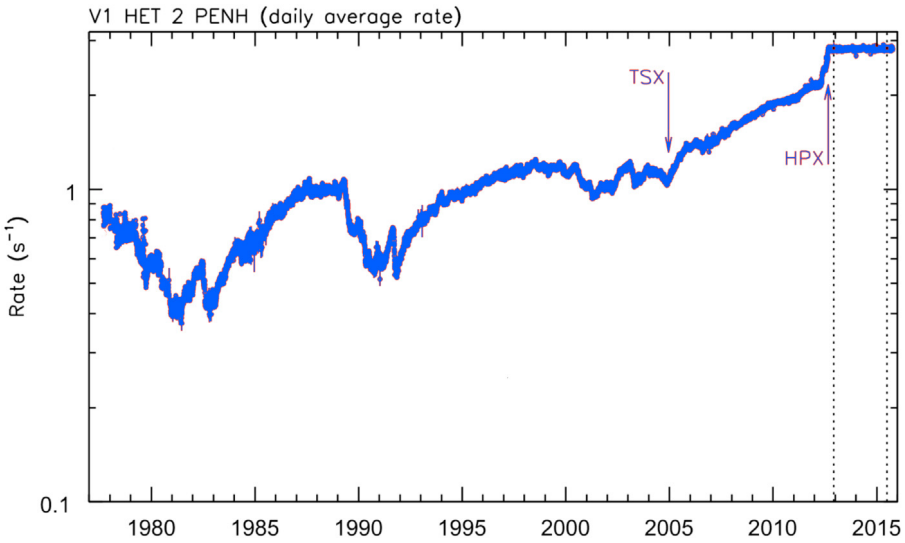

Fig. 17. Voyager 1 proton counting rate> 70 MeV from 1977 to 2015. The crossing of the solar wind termination shock is labeled by TSX and that of the heliopause by HPX.

3.1.1. The sun and the solar activity

The Sun is the central engine of the Solar System and accounts for almost 99% of its total mass. The Earth to Sun distance is about 150 millions of kilometers and is usually referred as one Astronomical Unit (AU). The internal structure of the Sun is characterized by a radiative and convective zone followed by a photosphere and a corona of plasma which extends millions of kilometers into space. The solar wind (SW) is a continuous stream of ionized gas moving at supersonic velocity emitted radially from the Sun due to the difference in pressure between the corona and the interstellar medium [83]. Through a mechanism known as flux freezing, the solar wind plasma carries the solar magnetic field out in the solar system creating the heliospheric magnetic field (HMF) [84].

At a heliocentric distance between 80 and 90 AU, where the solar wind pressure equals the external thermal pressure of the interstellar medium, the solar wind abruptly slows down to subsonic speed forming a shock called the termination shock (TS). The boundary where the interstellar medium and solar wind pressures balance is called the heliopause (HP). This bubble-like region of space occupied by the outward flowing of solar wind influences the cosmic rays propagation and is called Heliosphere.

It is well known that the Sun's activity periodically varies over an 11-year period, going through period of minimum and maximum activity. The solar magnetic field and the solar wind velocity are significantly weaker during solar minimum with respect to solar maximum periods. On top of that, every 11 years the solar magnetic field undergoes a polarity reversal introducing a second periodic variation with a 22-year periodicity. When the solar magnetic field points outward in the Northern hemisphere and inward in the Southern hemisphere, the Sun is said to be in a positive polarity cycle, $A > 0$. The opposite situation is referred to as a negative polarity cycle, $A < 0$. These two cycles have a significant impact on cosmic rays at energy below few tens of GeV inside heliosphere as explained in the following.

3.1.2. Cosmic ray through the heliosphere

The cosmic ray propagation is heavily affected by the heliospheric environment and is mathematically described by the Parker equation which is a local version adapted from Eq. (5) [85]. The relevant propagation processes described by the Parker equation are convection with solar wind (adiabatic cooling), diffusion on HMF irregularities and drift due to HMF gradients and curvature. The main consequence of cosmic rays propagation through the Heliosphere is that below few tens of GeV the spectrum of cosmic rays changes both in shape and intensity with respect to the Local Interstellar Spectrum (LIS) which is defined as the spectrum outside the heliopause. Moreover, the intensity of cosmic rays is time-dependent as a consequence of the solar activity cycle. During a solar maximum period the intensity of cosmic rays measured inside the Heliosphere will be lower with respect to a solar minimum period as a consequence of the strongest HMF intensity and solar wind velocity which prevent more cosmic rays to reach the inner Heliosphere. As a consequence, measurements of a cosmic ray species performed by space experiments operated not simultaneously will lead to different results below few tens of GeV.

Fig. 17 fully describes the effects yet described and represents the proton counting rate as a function of time measured by Voyager 1, the only detector together with its companion Voyager 2, to have accomplished a direct measurement of the cosmic radiation beyond the heliopause. The twin spacecraft Voyager 1 and Voyager 2 were conceived for the Solar System exploration and they were launched by NASA in the summer of 1977 from Cape Canaveral and they are still

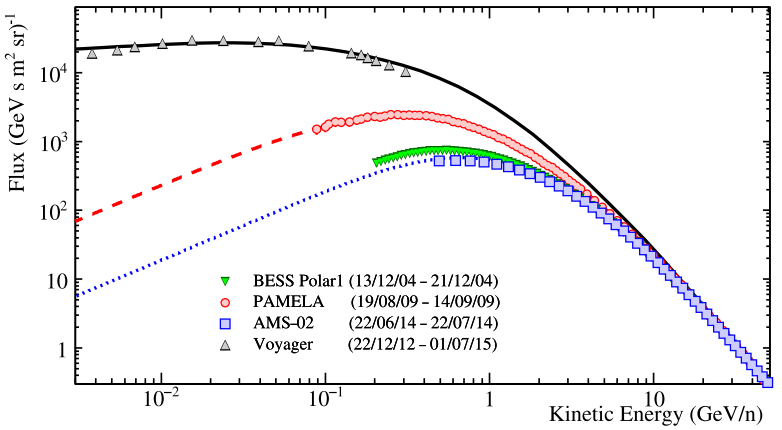

Fig. 18. Proton fluxes measured by BESS [91] (23rd solar maximum), PAMELA [92,93] (23rd solar minimum) and AMS-02 [94] (24th solar maximum) compared to the results obtained by Voyager 1 outside the Heliopause. The black solid line is the LIS based on the GALPROP model [87], while the red dashed and the blue dotted lines are the results of a 3D numerical model [90] for cosmic rays propagation inside the Heliosphere used to reproduce the PAMELA and AMS-02 results, respectively.

operating. Each spacecraft is equipped with several instruments among which the cosmic ray subsystem is devoted to measure protons, electrons and heavy nuclei up to Fe from few MeV up to few hundreds of MeV [86].

The proton counting rate presented in Fig. 17 have a general increasing trend over time or equivalently as the distance from the Sun increase. In fact, due to convection and diffusion, the closer to the Sun is the cosmic ray instrument the higher is the modulation effect. As the distance from the Sun increases less cosmic rays are prevented to reach the instrument thus the intensity increases approaching the LIS values. Labeled as TSX is the crossing by Voyager 1 of the termination shock at about 94 AU, followed by the crossing of the heliopause, identified with HPX, at about 122 AU. The heliopause crossing is identified as the position from the Earth after which the intensity of protons remains constant over time, this means that Voyager 1 from late 2012 is most likely measuring the cosmic ray LIS. Direct measurements of cosmic rays outside the Heliosphere are extremely important in order to test and calibrate numerical code for cosmic ray transport in the Galaxy like GALPROP [87] or as an input for cosmic ray propagation model through the Heliosphere, e.g. [88–90].

On top of the increasing trend over time, the cyclic variation with 11 years periodicity due to the solar activity cycle is also visible in Fig. 17. In correspondence with the 21st, 22nd and 23rd solar maxima occurred in December 1979, November 1989 and November 2001 the proton rate shows a decrease due to the increasing solar activity that prevented more cosmic rays to penetrate the Heliosphere with respect to the period of solar minima occurred around 1975, 1985 and 1996.

3.1.3. Proton, electron and positron solar modulation

Precise time-dependent spectral measurements of different particle species are fundamental to study the effect of propagation through the Heliosphere. Instruments for solar modulation studies need to:

- Have long duration: in order to survey time variation over extended period of time with one single instrument (ideally at least one solar cycle);
- Perform multi-particle measurement: to study the propagation mechanism over different particle species;
- Measure the particle charge-sign: to study the charge-sign dependent solar modulation;
- Have an extended energy range: ideally from several tens of GeV down to the lowest possible energy.

Both PAMELA and AMS-02 instruments (see Section 2.2.1) satisfy all these requirements and their results will be used in the following to describe the solar modulation. The PAMELA instruments had the advantage to reach a lower energy limits with respect to AMS-02 (70 MeV/n against 500 MeV/n for protons and electrons) while the AMS-02 thanks to its larger acceptance is able to study the time dependent intensity with a much finer resolution. Also the multiple BESS flights provide useful measurements for this study performing measurement of proton, helium and antiproton during different phase of the solar activity.

The proton spectra measured by AMS-02 [94], BESS [91] and PAMELA [92,93] during different phases of solar activity are shown in Fig. 18 together with the proton LIS from Voyager 1. The PAMELA fluxes were measured in August 2009, during the minimum phase of the 23rd solar cycle and result higher than the AMS-02 and BESS fluxes measured respectively in June 2014 and December 2004 during the maximum phase of the 23rd and 24th solar cycle. At around 0.6 GeV/n the proton intensity during the solar minimum is a factor 3.7 higher while at 3 GeV/n is only 1.4 times higher. The experimental sensitivity to the solar modulation stops at $\approx$ 50 GeV/n since the current uncertainties do not allow to appreciate any time dependence above this value. However even above 50 GeV/n a tiny modulation effect is expected,

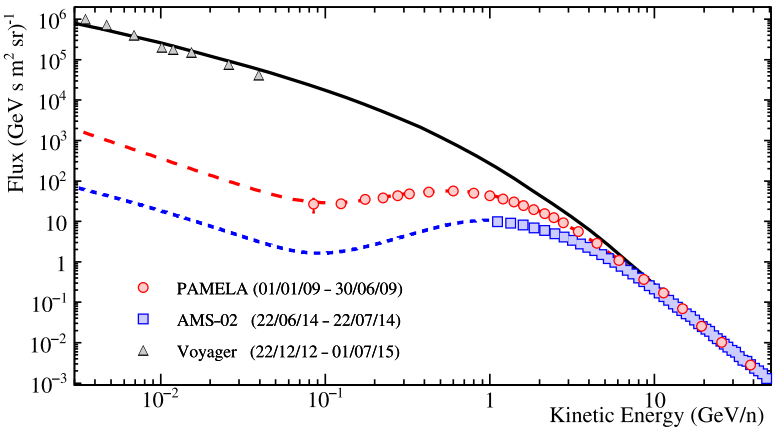

Fig. 19. Electron fluxes measured by PAMELA [95] (23rd solar minimum) and AMS-02 [96] (24th solar maximum) compared to the results obtained by Voyager 1 outside the Heliopause. The black solid line is the LIS based on the GALPROP model [87], while the red dashed and the blue dotted lines are the results of a 3D numerical model [97].

probably of the order of a fraction of one per cent. The Voyager 1 results were obtained with data collected after late 2012 and thus represent the proton LIS.

The solid lines in Fig. 18 are the results of numerical models for propagation of cosmic rays. The black line is the proton LIS obtained with the GALPROP code [87] tuned in order to reproduce the Voyager 1 data at low energies and the PAMELA and AMS-02 data above $\approx$ 50 GV, where the effect of solar modulation is considered negligible. The LIS obtained from GALPROP is then used as an input of numerical codes which reproduce the propagation of cosmic rays inside the Heliosphere. The solid lines overlapping with the AMS-02 and PAMELA data are obtained with the full 3D numerical model described in [90]. Precise data with good time resolution are fundamental to test and calibrate the propagation models.

It is interesting to note that below 1 GV the model shows a continuous decrease for the proton intensity measured at 1 AU with a power law of E^1 where E is the kinetic energy. This is due to the effect of adiabatic cooling that at low energies prevents more cosmic rays to reach the inner part of the Heliosphere. On the contrary, due to their lower mass, low energy electrons have completely different behavior since their propagation is dominated by diffusion. This situation is illustrated in Fig. 19 which shows the cosmic-ray electron-fluxes measured by PAMELA [95] and AMS-02 [96] experiments during the 23rd solar minimum and the 24th solar maximum, respectively. These data are compared to the results obtained by Voyager 1 outside the Heliopause. The solid lines represent the electron LIS obtained from GALPROP and the modulated fluxes resulting from a 3D numerical model [97]. Also in this case the electron fluxes during the solar minimum period are higher with respect to the solar maximum. The flux measured by PAMELA at 0.6 GeV is about a factor 6 higher than the AMS-02 flux and at 3 GeV about a factor 3.3 higher. These increasing factors are higher with respect to those measured for protons due to drift effects that introduce a charge-sign dependence to the solar modulation and will be discussed later. As pointed out before, the electron spectral shape at 1 AU is significantly different from the protons. In this case the dominant mechanism below few tens of MeV is diffusion. As a consequence below a few tens of MeV the electron energy spectrum measured inside the Heliosphere has the same slope of the LIS but with a much lower intensity.

The different behavior of protons and electrons demonstrates that in order to compute spectra of different particle species over time, a realistic model for cosmic ray propagation inside the Heliosphere is needed, overcoming the force field approximation that is widely used and works only for protons at 1 AU [98] with rigidities greater than 1 GV. For example, realistic predictions of the cosmic-ray intensity during different phases of the solar activity and at different location of the Heliosphere are particularly important in order to calculate the radiation dose for astronauts.

In addition to the time-dependent modulation a charge-sign dependent modulation is introduced by the drift motion due to the presence of gradients and curvature in the HMF. Since the drift motions depend on the sign of the charge the global drift pattern is expected to be opposite for positive and negative charged particles. The global drift pattern inside the Heliosphere for electrons and protons during HMF polarity $A < 0$ and $A > 0$ is illustrated in Fig. 20. During $A > 0$ positively charge particles undergo drift motion from the polar and outwards along the equatorial regions. Positively charged particles drift in opposite directions. The situation reverses when the solar magnetic field changes its polarity at each solar maximum (e.g. [99]).

A direct consequence is that oppositely charged particles propagate preferentially through different zones of the Heliosphere and experience different amounts of modulation [101,102]. The situation is illustrated in Fig. 21 which shows the positron to electron ratio as a function of time measured by the PAMELA instrument [100] for an entire solar cycle over the magnetic field polarity reversal. If positrons and electrons would experience the same solar modulation this ratio would be constant over time, instead a time dependence is observed. It is also interesting to note the sudden increase of the ratio after the polarity field reversal due to the inversion of the drift pattern. The charge sign dependence has

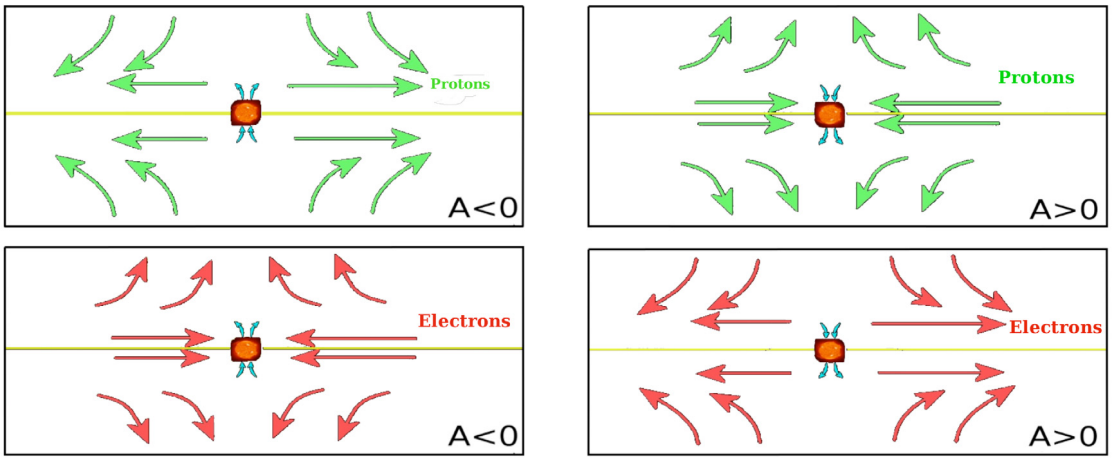

Fig. 20. Global drift pattern inside the Heliosphere for oppositely charged particles during different polarities of the HMF.

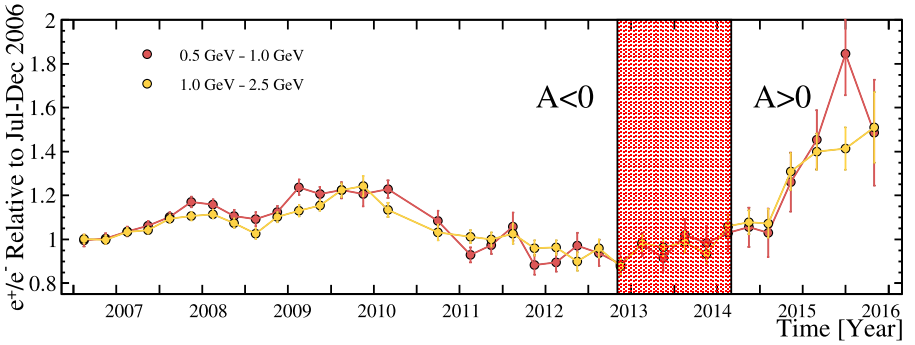

Fig. 21. The positron to electron ratio measured by the PAMELA experiment from July 2006 to January 2016 [100]. Each point represents 3 month of data taking. The red shaded area represents the period of time where no defined polarity of the Sun magnetic field was present. The non constant ratio indicates the presence of a charge-sign dependent solar modulation which is ascribable to drift motions.

the maximum effect at around few hundreds of MeV and is negligible above $\approx$ 10 GeV and below $\approx$ 10 MeV [103]. It clearly follows from this a time dependence also in the positron fraction (the ratio of positron and the sum of positron and electron fluxes), which will be discussed in Section 3.2.5.

3.2. Cosmic ray spectra and composition

As previously discussed, measurements of the energy spectra and composition of the cosmic radiation provides important information on the acceleration and propagation mechanisms of cosmic rays in the Galaxy.

3.2.1. The cosmic ray paradigm

The cosmic ray paradigm holds that the cosmic rays up to the knee region are accelerated at galactic SuperNova Remnants (SNR) located in the galactic disc. SNRs have the right energetics and through diffusive shock acceleration cosmic rays are efficiently ($\approx$ 10% of SNR bulk energy, e.g. [104]) accelerated (e.g. [105,106]) and injected in the interstellar medium with an approximate power law spectrum with spectral index $\simeq -2$. The process is pure rigidity dependent (scattering in magnetic turbulence) and therefore the power-law spectrum at injection is universal for all particle species.

Subsequently, the cosmic rays propagate in the Galaxy and its halo, a low-density confinement region extending for several kpc beyond the disk, where they diffuse interacting with the interstellar medium and magnetic fields [107]. The propagation for each single cosmic-ray specie (labeled by the index i) is usually described by the transport equation [108]:

$$\frac{\partial \psi_i}{\partial t} = q_i(\mathbf{x}, p, t) + \nabla \cdot (D \nabla \psi_i - \mathbf{u} \psi_i) + \frac{\partial}{\partial p} p^2 D_p \frac{\partial}{\partial p} \frac{1}{p^2} \psi_i - \left[\frac{\partial}{\partial p} \dot{p} \psi_i - \frac{p}{3} (\nabla \cdot \mathbf{u}) \psi_i \right] - \frac{1}{\tau_{f_i}} \psi_i - \frac{1}{\tau_{r_i}} \psi_i \,, \tag{5}$$

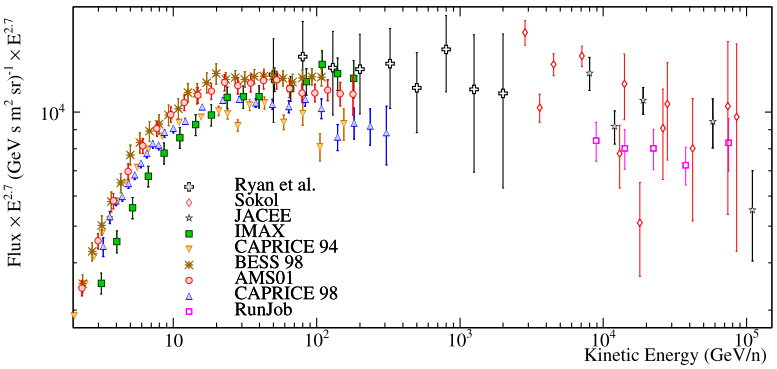

Fig. 22. Compilation of measurements of the proton energy spectrum: Ryan et al. [109], SOKOL [110], JACEE [111] CAPRICE94 [112], IMAX [113], BESS98 [114], AMS-01 [34] CAPRICE98 [115], RUNJOB [116]. The fluxes are multiplied by $E^{2.7}$, where E is the energy in GeV.

where $\psi = \psi(\mathbf{x}, p, t)$ is the cosmic-ray density per unit of total particle momentum p at position x and at time t, $q(x, p, t)$ is the source term that includes primary, spallation and decay contributions, D is the spatial diffusion coefficient, u is the convection velocity, D_p is the diffusion coefficient in momentum space and describes the diffusive reacceleration, $\dot{p} = dp/dt$ is the momentum gain or loss rate, τ_f is the characteristic time for loss by fragmentation and τ_r is the time scale for radioactive decay. Cosmic-ray diffusion on the galactic magnetic field is the main transport mechanism and explains why the cosmic-ray spatial distribution appears to be highly isotropic. For primary cosmic-ray species (e.g protons, helium, carbon) energy gains and losses can be neglected at high energy and the transport Eq. (5) at equilibrium can be simplified as:

$$0 \;=\; q_i(\mathbf{x}, p, t) + \nabla \cdot (D \nabla \psi_i)\,, \tag{6}$$

assuming an injection $q \propto p^{-\gamma}$, the classic solution is:

$$\psi_i \;\sim\; \frac{q}{D(p)} \sim p^{-\gamma-\delta}\,. \tag{7}$$

Hence, the propagation process results in a softening of the cosmic-ray energy spectra observed in the Galaxy. Therefore, according to the cosmic-ray SNR paradigm the local interstellar spectra observed nearby the Solar System reflect the injection spectra plus the softening due to the propagation. This qualitatively explains the cosmic-ray spectrum of Fig. 1 and why it is steeper than the predicted injection spectrum. It should also be noted that for pure secondary elements (e.g. boron) the source term is proportional to the primary density and the secondary-to-primary ratio (e.g. B/C) is inversely proportional to the diffusion coefficient ($D(p)$), i.e.:

$$\frac{B}{C} \;\approx\; \frac{1}{D(p)} \;\approx\; p^{-\delta}\,. \tag{8}$$

Thus, the standard scenario of cosmic rays can be tested analyzing precision measurements of the cosmic-ray energy spectra over a wide energy range and for various cosmic-ray species.

A first distinction of cosmic rays is based on being of primary, i.e. accelerated at the sources, or secondary, i.e. produced by interaction of cosmic rays with the interstellar medium, origin. Protons, helium, carbon and oxygen are the most abundant primary components while lithium, beryllium and boron are some of the most abundant secondary components.

3.2.2. Protons

Protons, together with helium nuclei, are the most abundant components of galactic cosmic rays constituting more than 95% of the total cosmic-ray flux. Not surprisingly, they are also the best measured cosmic ray components. Fig. 22 shows a compilation of various proton flux measurements[2] taken by balloon and space-borne experiments in the last century. Several things can be noticed. Due to the steep falling spectrum, data are statistically limited to relatively low energies, usually well below the knee region. There is a significant spread in the data well beyond the quoted statistical and systematic (mostly not shown in figure) uncertainties. At low energies ($<$ 30 GeV) the differences are partially due to solar modulation effects. However, the remaining experimental differences probably arise from efficiency and energy determinations. As discussed in Section 2 good energy determination and efficiency estimations require precise calibration and Monte Carlo analysis and these discrepancies may result from an insufficient estimation of the

[2] As commonly done, the figures in this work show the fluxes multiplied by a power of the energy ($E^{2.7}$ for this figure), where E is the energy in GeV. Reducing the decades of variation of the flux, this allows for a clearer picture of the spectral shapes. However, this implies that the absolute energy uncertainties are added to the flux uncertainties.

Table 1
Parameters of the fit using Eq. (9) to the experimental data from 45 GeV to ≈ 1 TeV. The experimental statistical and systematic errors were added in quadrature. The fit was performed on the AMS-02 and PAMELA rigidity spectra and on the CALET and DAMPE kinetic energy spectra.

Experiment	E_b	γ_1	γ_2	ω
PAMELA	292 ± 209 GV	−2.843 ± 0.023	−2.656 ± 0.193	0.09 ± 0.40
AMS-02	409 ± 88 GV	−2.813 ± 0.006	−2.649 ± 0.056	0.09 ± 0.21
CALET	580 ± 236 GeV	−2.822 ± 0.052	−2.550 ± 0.058	0.26 ± 0.43
DAMPE	578 ± 552 GeV	−2.705 ± 0.062	−2.580 ± 0.109	0.16 ± 0.3

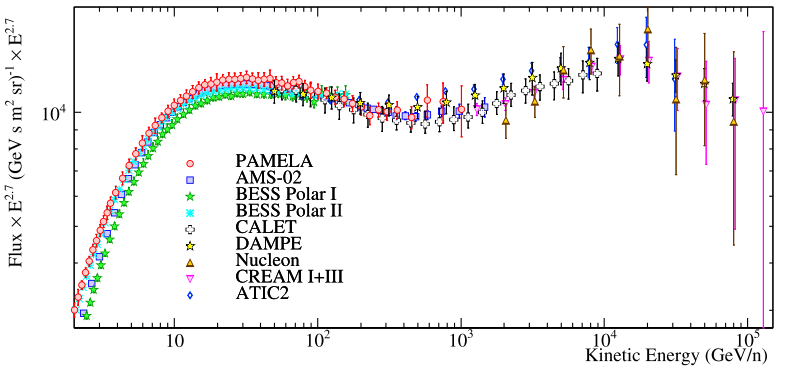

Fig. 23. Recent measurements of the proton energy spectrum: PAMELA [5,64], AMS-02 [118], NUCLEON-KLEM [119], CALET [120], DAMPE [121], ATIC2 [122], BESS-Polar I & II [123] and CREAM I+III [6]. The fluxes are multiplied by $E^{2.7}$, where E is the kinetic energy in GeV.

experimental uncertainties (see also [117]). Nonetheless, the shape of the proton energy spectrum appears consistent with the prediction of the cosmic-ray standard model but any more detailed analysis is hindered by the discrepancies in the measurements.

The new millennium saw the coming on line of new experiments with significantly improved instrumentation and long periods of data taking either in long duration balloon flights from Antarctica or in space. These experiments ushered a new era of precision cosmic ray measurements. Fig. 23 shows data from these experiments, from space: PAMELA [5,64], AMS-02 [118], NUCLEON-KLEM [119], CALET [120] and DAMPE [121] along with measurements from the balloon-borne experiments ATIC2 [122], BESS-Polar I & II [123] and CREAM I+III [6]. First thing that should be noted is that now an excellent agreement between the various measurements is found when the above-mentioned solar modulation effects and the quoted uncertainties are taken into account. Second, a clear hardening of the spectrum is observed around few hundred GeV. This hardening was first inferred by comparing the old magnetic spectrometer measurements at tens of GeV with the calorimeter measurements in the TeV region. The CREAM experiment reached this conclusion by comparing their proton spectrum measured above 1 TeV [124] with those measured by AMS-01 [34] and BESS [125] at lower energies. However, considering the different systematic, as discussed in Section 2, of a calorimeter-based experiment like CREAM with respect to magnetic spectrometers like AMS-01 and BESS, a firm conclusion was questionable. Another indication of a hardening but using the same instrument was obtained by the ATIC2 experiment [122], although the robustness of the result suffered from unclear systematic uncertainties (e.g. no evidence of spectral hardening in the hundred of GeV range for helium nuclei [122]). The first solid evidence of the hardening in the proton and helium energy spectra was obtained by PAMELA experiment [64] and subsequently confirmed by AMS-02 [118] with a significant increase in statistical precision. This can be clearly seen in Fig. 24 that shows a fit to AMS-02, PAMELA and the recent CALET and DAMPE flux data with the following equation [118,126]:

$$Flux = K\left(\frac{E}{45}\right)^{\gamma_1}\left[1+\left(\frac{E}{E_b}\right)^{\frac{1}{\omega}}\right]^{-(\gamma_2-\gamma_1)\omega}, \tag{9}$$

with E rigidity in GV for AMS-02 and PAMELA and energy in GeV for CALET and DAMPE, E_b the break energy, γ_1 and γ_2 the spectral slopes before and after the break, respectively, and a width $\omega > 0$. The values resulting from the fit are shown in Table 1.

A good agreement is found between the four sets of measurements clearly indicating a hardening of the proton spectrum occurring at a few hundred GeV. Many models were put forward to explain such a spectral hardening ranging from contributions from sources other that SNRs, e.g., nova stars [127] to propagation effects (for a review see [128]). Most recently, a consensus is arising that this feature is due to a change of regime in particle diffusion. The physical mechanisms to explain such effect were related to the transition from self-generated to pre-existing turbulence [129] or to a spacial dependence of the diffusion coefficient [130]. It is worth highlighting the recent paper by Evoli et al. [131]:

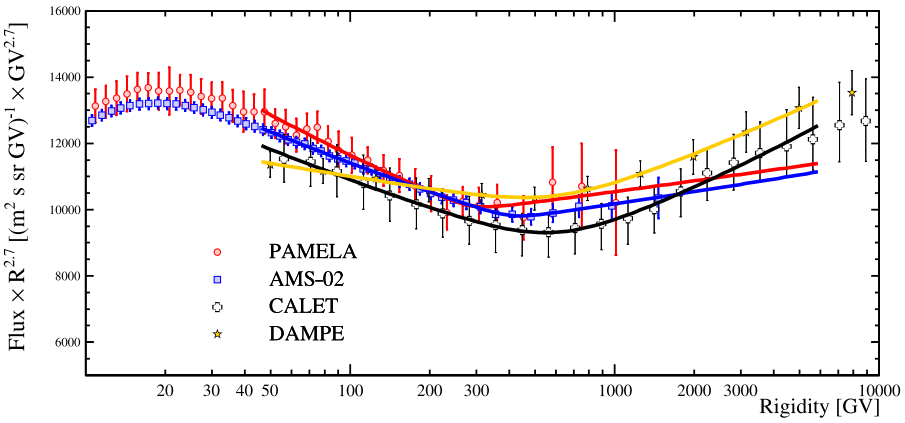

Fig. 24. Results of the fit performed with Eq. (9) on the proton AMS-02 and PAMELA rigidity spectra and on the CALET and DAMPE kinetic energy spectra. The solid line colors correspond to the marker colors.

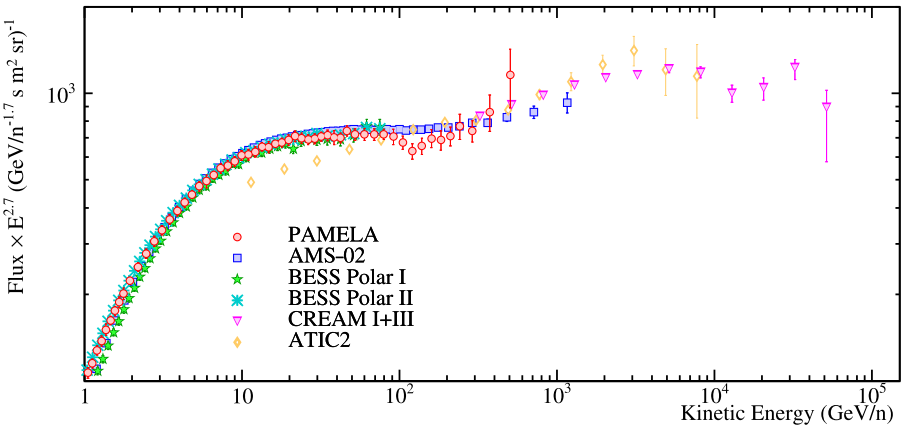

Fig. 25. Recent measurements of the helium nuclei energy spectrum: space-borne experiments PAMELA [64] and AMS-02 [133] and balloon-borne experiments ATIC2 [122], CREAM I+III [134] and BESS-Polar I & II [123]. The fluxes are multiplied by $E^{2.7}$, where E is the kinetic energy in GeV.

studying the proton spectrum, the authors propose a model where the Galactic halo arises naturally from a combination of the turbulence injected in the Galactic disc and the waves self-generated by cosmic rays. Furthermore, the change of slope at $\approx$ 300 GV arises naturally from the transition from a diffusion dominated by self-generation (at lower energies) to a Kolmogorov-like diffusion at higher energies.

It should also be noted that high-energy proton data in Fig. 23 seem to indicate a softening at $\approx 10 - 20$ TeV [6,119]. However, firm conclusions require more precise data. In fact, CREAM-III data [6] are statistically limited while NUCLEON results are obtained with an energy reconstruction method having an energy resolution of $\approx$ 70% [119]. For a proper analysis of the results, NUCLEON measurement requires a more thorough description of the systematic uncertainties than what can be found in [119]. Also the high precision CALET results [120] indicate a softening of the spectrum in the TeV region, however stopping at 10 TeV do not allow for a full description of the shape of the proton spectrum. However, preliminary results from DAMPE experiment [121] strongly point to a softening of the spectrum in this energy region.

3.2.3. Helium and heavier nuclei

The propagation effects discussed above are expected to operate on cosmic rays independently of the particle species. Therefore, the existence of the softening and energy/rigidity location of the break in the power law spectra in particle either than protons becomes a useful test of galactic propagation models.

Fig. 25 shows recent direct measurements of the helium nuclei[3] spectrum covering the energy range tens of GeV a few TeV. Although, ATIC2 results do not show any clear hardening of the helium nuclei spectrum below 1 TeV/n and BESS-Polar I & II measurements do not extend beyond 100 GeV/n, this hardening was clearly observed by PAMELA and, subsequently,

[3] About 10%–20% of helium nuclei are ^{3}He isotopes, e.g. [132].

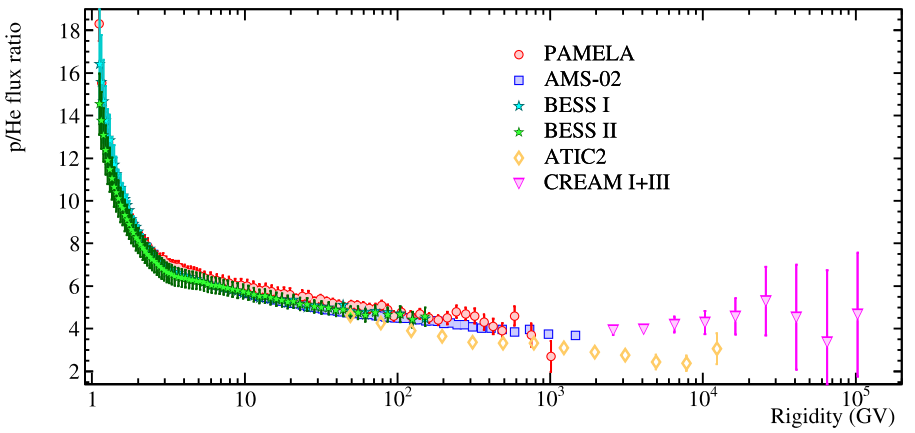

Fig. 26. The proton-to-helium flux ratio as a function of rigidity measured by the space-borne experiments PAMELA [5,64] and AMS-02 [133] and by balloon-borne experiments ATIC2 [122], CREAM I+III [134] and BESS-Polar I & II [123]. The published ATIC2 and CREAM I+III proton and helium nuclei energy spectra have been converted to rigidity spectra for this figure.

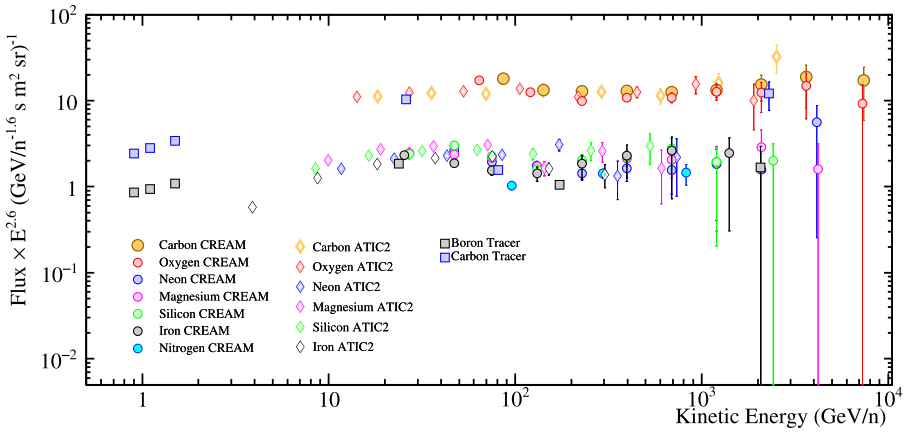

Fig. 27. Compilation of recent measurements of the energy spectra of primary nuclei heavier than He: ATIC2 [122], CREAM-II [135], TRACER [136–138]. The fluxes are multiplied by $E^{2.6}$, where E is the kinetic energy in GeV/n.

AMS-02 experiments. Moreover, this hardening is consistent with the harder helium nuclei spectrum measured by CREAM in the TeV region. Therefore, it can be reasonably assumed that the hardening is present also in the helium nuclei spectrum.

Two additional considerations can be drawn from these results:

1. if the proton and helium spectra are studied as function of rigidity instead of kinetic energy, the spectral breaks occur approximately at the same rigidities. PAMELA experiment estimated the rigidity break at 232^{+35}_{-30} GV and at 243^{+27}_{-31} GV for protons and helium nuclei [64], respectively. AMS-02 experiment estimated the rigidity break at $336^{+68+66}_{-44-28} \pm 1$ GV for protons [118] and $245^{+35+33}_{-31-30} \pm 3$ GV for helium nuclei [133]. Even accounting for the different approaches for the estimation of the rigidity breaks, the values are approximately similar and in the ballpark expected by recent models of transport in the Galaxy and in the halo, e.g. [131]. Furthermore, since the propagation is mostly affected by turbulence in magnetic fields, rigidity is the most natural quantity involved;
2. the proton and helium nuclei appear to have different spectral shapes.

The differences in the spectra of protons and helium nuclei can be highlighted studying the proton-to-helium flux ratio. Experimentally, this has the additional advantage of reducing the systematic uncertainties since several of them (for example the uncertainties associated with the tracking alignment for magnetic spectrometers) cancel out in the ratio. Fig. 26 shows the proton-to-helium flux ratio as a function of rigidity measured by recent balloon and space-borne experiments. These ratios clearly show that proton and helium nuclei have different spectral shapes. Furthermore, the ratio is very smooth and nearly a power law of spectral index ≈ -0.1 when presented as a function of rigidity. The explanation for this dependence on the rigidity of the ratio is not yet understood and it is not expected in the propagation models described before.

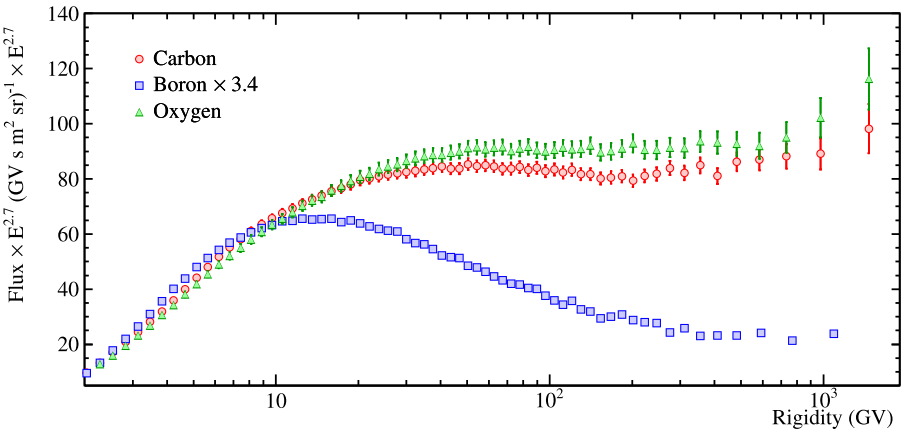

Fig. 28. The boron, carbon and oxygen rigidity spectra measured by AMS-02 [146] experiment. The fluxes are multiplied by $R^{2.7}$, where R is the rigidity in GV.

Three main hypothesis have been put forward (for a review see [139]): spallation processes between cosmic rays and the interstellar medium [140]; different cosmic-ray sources; difference between proton and helium injection based on the different charge-to-mass ratio [141]. Spallation of cosmic-ray nuclei ($Z > 1$) can result in hardening their spectra. However, it has been shown that the required amount of grammage to fit the measured proton-to-helium flux ratio would result in an overproduction of secondary species in the cosmic radiation [142] in contrast with measurement (see Section 3.2.4). The difference between the proton and helium spectra may result from different sources with different spectral indices and maximum energies [127]. However, this ad-hoc model cannot be fully tested and requires a significant fine tuning considering also the similarity of the helium nuclei spectrum with carbon and oxygen spectra (see Fig. 29). A more appealing model explains the difference on the dependence of the injection on the charge-to-mass ratio of the accelerated particles [141,143].

If the hardening of the proton and helium nuclei spectra is due to the particle propagation in the Galaxy, a similar hardening is expected in the spectra of other cosmic rays, both primary and secondaries, even if in the case of secondaries the spectra is expected to be steeper as shown in Eq. (8). Fig. 27 shows a compilation of rigidity spectra of primary nuclei heavier than He measured by ATIC2 [122], CREAM-II [135] and TRACER [136–138] experiments. While not excluding the hardening in the spectra in the hundred of GV region, no clear evidence is observed: the data are not sufficiently precise to draw firm conclusion. However, recently the AMS-02 experiment published high-precision measurements of the fluxes of carbon[4] and oxygen [145] that clearly show the spectral hardening as can be seen in Fig. 28. Furthermore, comparing the carbon and oxygen fluxes to the helium ones a similar behavior is found at high rigidities (above $\approx$ 60 GV) as can be observed in Fig. 29 that shows the helium-to-carbon and the helium-to-oxygen flux ratios measured by the AMS-02 experiment [145]. The helium-to-carbon and helium-to-oxygen flux ratios above 100 GV are rather well described by constant values of $\sim$ 30 and $\sim$ 27, respectively.

In the last decades, measurements of heavy cosmic-ray nuclei were performed with increasing precision and significant information on the cosmic-ray seeds and sources were obtained. In fact, it was observed that in the composition of heavier nuclei there was an excess of refractory elements with respect to volatile ones when comparing the cosmic-ray source composition[5] to Solar abundances [147]. This was explained in terms of preferential accelerations of elements found in interstellar grains with respect to acceleration of interstellar gas-phase ions [148]. These conclusion were essentially confirmed by the recent TIGER results on cosmic rays with atomic number $26 \leq Z \leq 38$ [149]. Furthermore it was observed that an improved organization of the cosmic-ray source abundances to solar system abundances data according to refractory and volatile components was obtained assuming a mixture by mass of 80% solar-system like composition and 20% from outflow of massive stars. Similar results were obtained by the Super-TIGER experiment [150] and also confirmed by preliminary ACE-CRIS results [151]. Hence, it was concluded that the bulk of cosmic-ray acceleration occur in OB stars associations and that galactic cosmic rays are accelerated from a mix of massive star material and normal interstellar matter with interstellar dust grains more effectively accelerated [44,149,151].

Other important information on the seeds of cosmic rays were obtained from measurements of the isotopes of nickel and cobalt nuclei, especially ^{59}Ni and ^{59}Co. Measurements performed by CRIS on ACE of these two isotopes were interpreted as indication that the cosmic-ray seeds were existing interstellar material rather than fresh supernova ejecta [152]. ^{59}Ni is a radioactive isotope that decays via electron capture with a half life of 0.76×10^5 years. Since the

4 Also PAMELA experiment published the carbon spectrum [144] but the data stopped at 200 GV.

5 The source composition is derived from measured cosmic-ray abundances corrected for the effects of solar modulation, and interactions and energy losses during propagation.

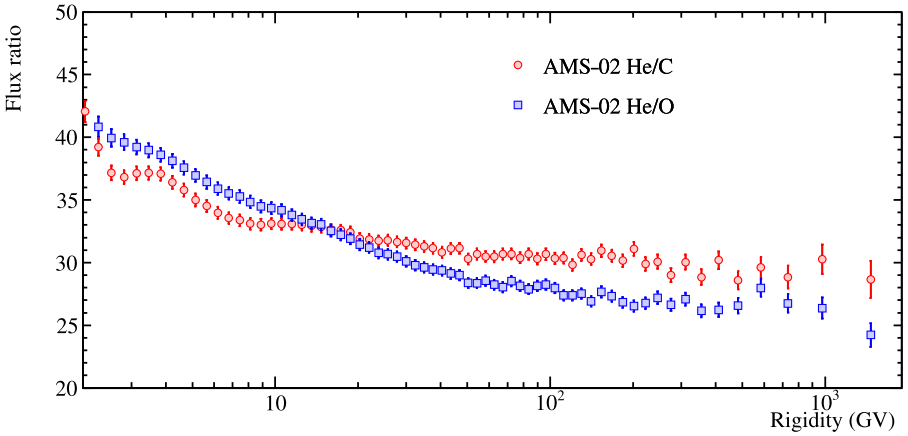

Fig. 29. The helium-to-carbon and the helium-to-oxygen flux ratios as a function of rigidity measured by the AMS-02 experiment [145].

acceleration process strips off the nuclei electrons, if freshly synthesized material as ^{59}Ni was accelerated, ^{59}Ni should survive and be present in the cosmic rays. The absence of this isotope points to an acceleration that occurred with a delay from nucleosynthesis greater than 10^5 years. The CRIS experiment performed these measurements at energies 150 − 500 MeV/nuc. Similar measurements conducted by the TIGER apparatus at higher energies ($\approx$ 0.8 − $\approx$ 5 GeV/n) [153] are consistent with this model.

3.2.4. Secondary nuclei

Secondary elements like, e.g., boron are produced by cosmic rays in their propagation in the Galaxy. Therefore they are tightly connected to both the spectra of the primaries and the physical processes that cosmic rays undergo during their propagation like amount of interstellar matter traversed, energy losses and reacceleration, decays, etc. Particularly meaningful is the secondary-to-primary flux ratio since, as shown in Eq. (8), it provides direct information on the diffusion coefficient and the grammage traversed by cosmic rays. Fig. 30 shows the boron-to-carbon (B/C) flux ratio measured by the CREAM [154], TRACER [155], PAMELA [144] and AMS-02 [146] experiments. The B/C ratio is very sensitive to propagation effects and the experimental data in Fig. 30 approximately scales like $R^{-1/3}$, which is consistent with the Kolmogorov theory of turbulence which predicts that asymptotically the ratio follows a power law of spectral index −1/3, e.g. [108]. Actually, a better fit to the data, especially AMS-02 results, is obtained adding a contribution of $\approx$ 0.2 g/cm^{-2} to the grammage traversed by cosmic rays, probably while escaping the sources [156]. Furthermore, the direct comparison of the energy spectra of secondary nuclei like boron with primary nuclei like carbon and oxygen as shown in Fig. 28 clearly show spectral hardening occurring at ≈300 GV. Once more this is consistent with changes in the diffusion coefficient either due to changes in the propagation properties of the interstellar medium or to a regime change in particle diffusion. It should also be noted the steeper spectra of secondaries than primaries in contrast with expectations from the nested leaky-box model [157,158] that was put forward to explain the recent cosmic-ray positron and antiproton results, as will be discussed in the next sections.

An important secondary component are the unstable nuclei like ^{10}Be, ^{26}Al e ^{36}Cl. With lifetime of the order of millions of years they have been used to estimate the average age of cosmic rays since the fifties. In the past, in the framework of a leaky box propagation model, the measurements of their ratios with respect to stable elements were used to estimate the size of the diffusion halo and the typical confinement time in the Galaxy of cosmic rays (e.g. $\sim$ 15 Myr [159]). However, this is not an appropriate picture especially for the propagation of unstable particles, e.g. [160]. In a more realistic diffusive halo model these unstable secondaries travel a few hundred parsecs before decaying, hence they are not very sensitive to the boundaries of the diffusive volume. However, they can be used to infer the diffusion coefficient and, in combination with stable secondary-to-primary ratios, the halo size if the diffusion coefficient does not vary significantly over the diffusive volume [108].

Most of the data on isotopes have been obtained at low energies, below a few hundred MeV per nucleon. Recently, the PAMELA experiment has published results on the fluxes of hydrogen and helium isotopes [132] and on the relative components of lithium and beryllium, but only as the ratio ^{7}Be/(^{9}Be+^{10}Be), up to about 1 GeV/n [161]. A balloon-born experiment designed for light isotopes, ISOMAX, was able to measure the ^{10}Be/(^{9}Be ratio in the energy range 1.13 to 2.03 GeV/n [55], unfortunately the collected statistics was limited because the experiment permanently damaged on the second flight. Interesting results on light isotopes above 1 GeV/n are expected by the AMS-02 experiment and by the balloon-borne experiment HELIX [162], that is expected to fly on a long duration balloon over Antarctica during NASA's 2019/20 Antarctic balloon campaign.

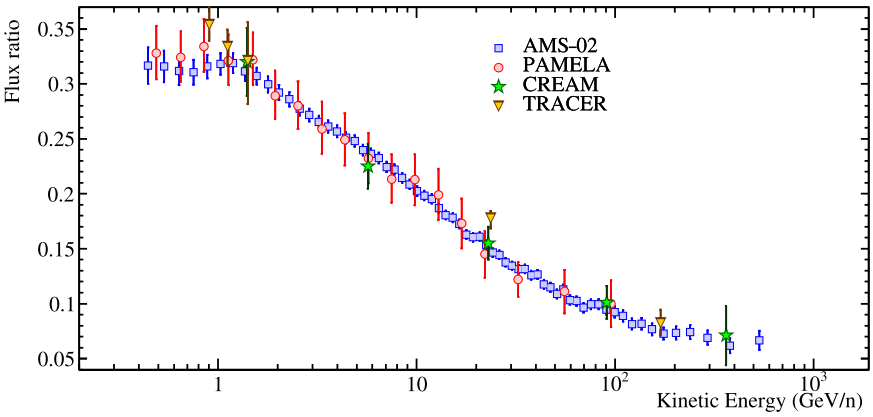

Fig. 30. The boron-to-carbon flux ratios as a function of kinetic energy measured by the CREAM [154], TRACER [155], PAMELA [144] and AMS-02 [146] experiments.

3.2.5. The light components: electrons and positrons

Electrons are a small (they constitute about 1% of the total cosmic-ray flux) but important component of the cosmic radiation (e.g. [163]). For a start, they are the only component for which unambiguous evidence of acceleration at SNRs exists. In fact, measurements of both synchrotron X-ray (e.g. [164,165]) and TeV gamma-rays (e.g. [166]) clearly indicate that high energy electrons are accelerated at SNRs where they interact with the microwave background radiation producing gamma rays via inverse Compton processes.

Second, electrons with energies above 100 MeV undergo severe energy losses mostly through synchrotron radiation in the Galactic magnetic field and inverse Compton scattering with the interstellar radiation fields and the cosmic microwave background radiation. From these effects an average life time (τ), over which the electrons lose half of their energy, can be approximated as $\tau = 2.5 \times 10^8$ (yr)$/E$ (GeV) [167]. This is a significantly smaller residence time than other cosmic ray species implying a significantly different history and propagation scale for electrons, hence spectral shape at Earth. In fact, considering that in a diffusive propagation model electrons cover on average a distance $\approx \sqrt{2D\tau}$ [22], it follows that, for example, a 10 GeV electron has a path length of just a few kpc. Additionally, the short propagation scale for high energy electrons implies that, if present, local astrophysical sources may induce features in the spectral shape of the electron energy spectrum [168,169] and anisotropies in the arrival direction of very high energy electrons (e.g. [167]).

A non negligible (several percent) fraction of electrons is of secondary origin, i.e. produced by the interactions between cosmic-ray nuclei and the interstellar matter. This is an empirical conclusion derived from the measured cosmic-ray positron component amounting to several percent of the electron one (see Fig. 33). In fact, secondary electrons are produced together with positrons (with positrons produced in slight excess) as the end product of the decay of short-lived particles (mostly pions via the decay $\pi^{\pm} \rightarrow \mu^{\pm} \rightarrow e^{\pm}$) produced by cosmic rays interacting with the interstellar matter.

Finally, as will be discussed later, recent measurements of the positron component led to considering additional sources for electrons and positrons ranging from astrophysical ones (e.g. pulsars) to more exotic (e.g. annihilation or decay of dark matter particles).

All of this has prompt the development of new experiments with the primary goal of measuring the electron component. As in the case of other cosmic ray species, direct measurements of cosmic-ray electrons have been conducted measuring their energies either with calorimeters or with magnetic spectrometer. Calorimeters are especially suited for measurements of electromagnetic particles like electrons performing simultaneously high precision energy measurements and particle identification. With respect to magnetic spectrometers they benefit from a few percent energy resolution approximately constant over a wide energy range. Vice versa, the lack of a magnetic field does not allow a direct charge-of-sign separation resulting usually in a measurement of the so-called "all-electron" spectrum, i.e. the energy spectrum resulting from the sum of both electrons and positrons. Fig. 31 shows the most recent direct measurements of the all-electron spectrum obtained by ATIC2 [170], Fermi [171], PAMELA [5], AMS-02 [40], DAMPE [172] and CALET [173] experiments.

A few interesting features can be observed:

- the highest energy fluxes measured by both CALET and DAMPE show a significant spectral break at about 1 TeV confirming previous indications resulting from the measurements of electromagnetic showers in the atmosphere performed first by the ground experiment H.E.S.S. [174,175] and later by the ground experiments MAGIC [176] and VERITAS [177]. This spectral feature may be the result of a single, local and fading source of electrons that accelerates only electrons, e^-, up to multi-TeV energies [178] or of the stochastic nature of the source distribution however assuming also an order of magnitude lower supernova rate [179]. No other significant features are evident in the multi-TeV energy spectrum that could clearly point to local sources as conjectured in [167];

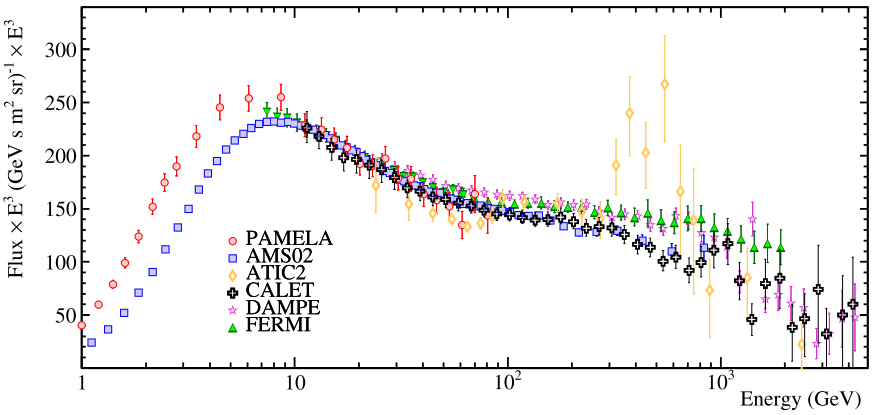

Fig. 31. The all-electron energy spectrum measured by the space experiments: Fermi [171], PAMELA [5], AMS-02 [40], DAMPE [172] and CALET [173] experiments and by the balloon-borne experiment ATIC2 [170]. The error bars include both statistical and systematic (as explicitly quoted by each experiment) uncertainties added in quadrature. The fluxes are multiplied by E^3, where E is the energy in GeV.

- below the TeV region and above the energy region of influence of solar modulation, the spectrum is approximately a feature-less power law of spectral index $\sim -3.1 \div -3.2$, hence softer than the proton and nuclei spectra, not inconsistent with propagation models. A more in-depth discussion will be done later when addressing the separate e^- and e^+ components;
- there are obvious differences between the various measurements with ATIC2 results the most in disagreement. ATIC2 data point to clear power-law breaks at $\sim$ 100 GeV and in the few hundred GeV region. Especially this last spectral feature challenged the standard model of cosmic rays prompting a variety of theoretical explanations invoking dark matter or nearby pulsar signals. However, since none of the other recent direct measurements confirmed these features it is probable that ATIC2 results were affected by additional, unknown systematic uncertainties. Notwithstanding ATIC2 data, a disagreement, albeit less significant, is also present in the other experimental data. Actually, in the energy region 100–1000 GeV the measurements gather in two sets of spectral shapes: one harder by Fermi and DAMPE experiments and one softer by AMS-02 and CALET (and PAMELA, extending its measurements above 100 GeV) experiments. Except in the case of Fermi results [171] that are affected by relatively large systematic uncertainties not all shown in Fig. 31, the differences cannot be reconciled with the various quoted experimental uncertainties. This may indicate that additional systematic uncertainties affect a few if not all these measurements, thus, significantly limiting a more extensive analysis of the energy spectrum and search for possible features.

This last point is particularly worrisome, since the existence of unknown systematics may reduce the interest in more statistically significant measurements. Personally, we regard as more accurate the results obtained with redundant detectors like the AMS-02 experiment. As discussed in Section 2.2.2, AMS-02 measured the electron energy with the calorimeter and was able to cross-check the measurements with the magnetic spectrometer. Furthermore, the AMS-02 apparatus was able to validate the electron identification of the calorimeter with the TRD response. However, until the various experiments will resolve this conundrum, an additional uncertainty of $5 \div 10\%$ should be considered when analyzing the all-electron experimental data above a few tens of GeV.

It has been often noted that the separate cosmic-ray e^- and e^+ fluxes yield much more information and provide stronger constrains to theoretical models than the all-electron spectrum. However, the separation of the two sign-of-charge components usually requires a magnetic field thus reducing the number of existing measurements. Fig. 32 shows the most recent measurements of the e^- and e^+ spectra by Fermi [59], PAMELA [5,41,70] and AMS-02 [180,181]. Even without a magnet, the Fermi experiment was able to separate the two electron components up to 200 GeV using the opposite distortion of the Earth's shadow cased by Earth's magnetic field. Except for the low energy part of the spectra affected by solar modulation, an excellent agreement between the three sets of measurements is observed for the e^- spectrum. In the case of the e^+ spectrum the results from Fermi are systematically higher than AMS-02 and PAMELA data. This may indicate an unaccounted for systematic uncertainty in Fermi data, probably due to a residual contamination of protons considering the limited, compared to AMS-02 and PAMELA, rejection power of the Fermi apparatus.

Particularly significant is the different shape of the positron and electron energy spectra. Historically, the quantity that was studied was the positron fraction, i.e. the ratio of positron and the sum of positron and electron fluxes (ϕ): $\phi(e^+) / (\phi(e^+) + \phi(e^-))$. The advantage of measuring the fraction instead of fluxes lies in not requiring a full knowledge of the instrumental performance. That is, various efficiencies can be reasonably assumed to be identical for e^- and e^+, hence, their evaluation is not required for the positron fraction estimation. Fig. 33 shows several recent measurements of the positron fraction together with a calculation for pure secondary production of positrons during the propagation of cosmic-rays in the galaxy [182–184]. A few very interesting features can be noticed:

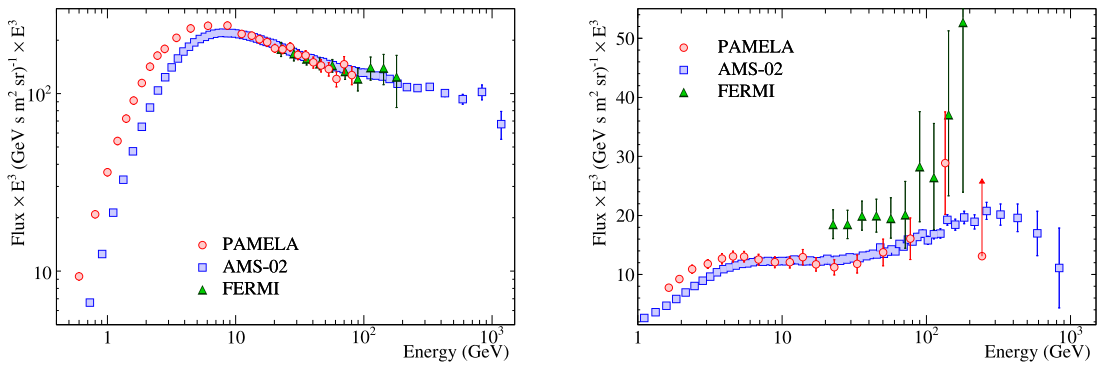

Fig. 32. The most recent measurements of the: left e^-, right e^+, energy spectrum: by Fermi [59], PAMELA [5,41,70] and AMS-02 [180,181] experiments. The fluxes are multiplied by E^3, where E is the energy in GeV.

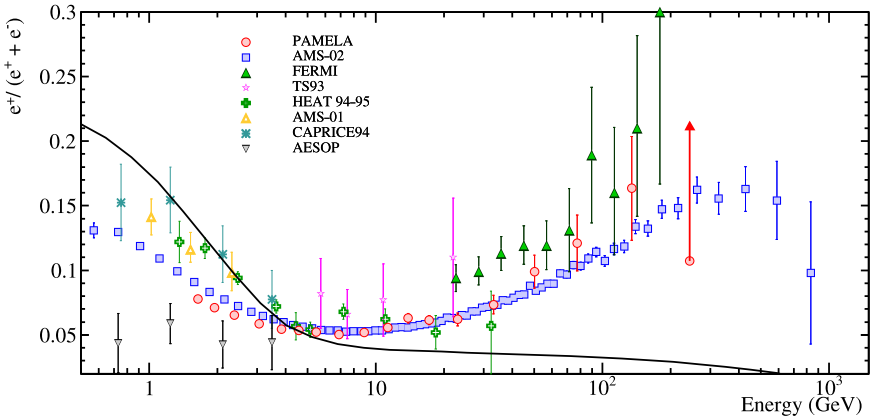

Fig. 33. Compilation of a few of the most recent measurements of the positron fraction: TS93 [185], HEAT94+95 [186], CAPRICE94 [187], AMS-01 [188,189], Aesop [190] PAMELA [70], Fermi [59], AMS-02 [180] experiments. The solid line shows a calculation for pure secondary production of positrons during the propagation of cosmic-rays in the galaxy [182–184].

- the experimental data below 5 GeV is approximately consistent or lower than the expectation for secondary production;
- but the various sets of experimental data differ significantly at these lower energies;
- on the contrary an agreement between the various measurements is observed at higher energies;
- all data sets point to a significantly higher than expected (from secondary production) positron fraction above 10 GeV.

The differences between the various low energy measurements is most probably the result of charge-sign solar modulation effects. As discussed in Section 3.1, drift effects cause charge-sign dependent solar modulation [103] and these effects depend on the intensity and polarity of the Sun magnetic field. The various experimental measurements were taken during different solar polarity: TS93 [185], HEAT94+95 [186], CAPRICE94 [187] and AMS-01 [34,189] data were collected in a $A > 0$ polarity cycle, while Aesop [190], PAMELA [70] and Fermi [59] data during a $A < 0$ polarity cycle. AMS-02 [180] data were collected during a period of maximum solar activity over two solar cycles of different polarity. In fact, comparing PAMELA and AMS-02 measurements taken over the same time period a good agreement is found [191].

At higher energies, a clear consensus exists in the experimental data that the positron fraction increases as the energy increases as a result of a e^+ spectrum harder than the e^- one. Such an increase is difficult to explain in the standard cosmic-ray paradigm, i.e. solid line in Fig. 33. Since e^- are mostly of primary origin their energy spectrum in the Galaxy is expected to be steeper than the hadronic one, see Eq. (7), due to the significantly higher energy losses, i.e. the spectral index should scale as $E^{-\gamma-\alpha}$ with $\alpha > \delta$. Hence, in qualitative agreement with the experimental data shown in Fig. 32 left. However, if positrons are only produced by interactions of cosmic rays with the interstellar matter the observed positron spectrum should reflect the parent, hadron, spectrum of Eq. (7) with the additional steepening due to energy losses, i.e. it should scale as $E^{-\gamma-\delta-\alpha}$. Hence, steeper than the primary electron spectrum resulting in a decreasing positron fraction. The opposite experimental results imply that either there is a primary e^+ (and, most probably, additional primary e^-) component or that the standard cosmic-ray paradigm has to be modified.

Thousands of works and ideas were put forward to interpret these positron results. Sources of positrons have attracted most of the interest of the community in recent years. Concerning astrophysical sources the most appealing and studied are pulsars. The production of positrons and electrons through pair production processes in the magnetosphere of pulsars have been contemplated since may years (e.g. [192,193]). Then, these accelerated pairs can escape into the interstellar medium contributing to the cosmic-ray positron and electron components. Thus pulsars, especially nearby ones because of energy losses, can explain the observed positron spectrum (e.g. [194]). Recently, this explanation was reexamined in depth following the results of the HAWC experiment [195]. HAWC stands for High-Altitude Water Cherenkov and it is an observatory located on the flanks of the Sierra Negra volcano near Puebla, Mexico at an altitude of 4100 m. The instrument detects the Cherenkov light produced by particles from air shower traversing tanks filled with purified water. By observing the intensity and pattern of signals from the water tanks atmospheric showers induced by gamma rays can by discriminated from showers produced by charged cosmic rays. Furthermore, the shower axis of the shower, hence the arrival direction of the photon, is estimated. HAWC measured high energy ($>$ TeV) gamma-ray emission from two nearby middle-aged pulsars (Geminga and PSR B0656+14) [195] often speculated to be the origin of most of the high-energy cosmic-ray positron signal (e.g. [196]). The HAWC collaboration concluded that this high-energy gamma rays were produced by inverse scattering mostly with the CMB of high-energy e^- and e^+ up to energies of the order of 100 TeV. The emitting regions extend a few tens of parsec around the two pulsars. Furthermore, by observing the surface brightness as a function of the distance from the two pulsar, a diffusion coefficient was estimated about 100 times smaller than what is usually assumed in standard model of cosmic-ray and electron propagation (e.g. [182]). Assuming that this diffusion coefficient is valid for the local interstellar medium from the pulsars to the solar system, it was concluded that these two pulsars could contribute only for a few percent to the high-energy positron fluxes [195]. Therefore, other sources than pulsars should be considered to explain the majority of the cosmic-ray positron signal. However, if the diffusion coefficient in the local interstellar medium is not the same as in the nearby of the pulsars but it is instead similar to the standard value inferred from cosmic-ray nuclei (e.g. B/C data), then an opposite conclusion can be reached, i.e. that nearby pulsars provide significant contribution to the high-energy positron (and electron) fluxes (see [197,198]). This two zone scenario could be due to the suppression of the cosmic-ray diffusion in the region around pulsar caused by the Alfvèn waves generated by the escaping electrons and positrons [199]. Yet, it has also be noted that the diffusion coefficient estimated by HAWC experiment is consistent with theoretical expectation at least for the value in the disc [200]. This would imply that either pulsars do not contribute significantly to the detected cosmic-ray e^+ signal or there is a single nearby (within 30 to 80 pc of the Earth) yet undiscovered pulsar [201]. For more detailed discussion of this issue see [202].

Among the various astrophysical sources proposed to explain the positron data, supernova remnants should not be neglected (e.g. [203]). Worth of notice is the recent work by Diesing and Caprioli [204] that using a semi-analytic approach to non-linear shock acceleration at supernova remnants obtained a softer injection spectrum for electrons respect to protons with a difference in spectral slope of $\approx 0.1-0.3$, thus potentially explain the difference e^+ and e^- energy spectra. However, the similar spectral index of high-energy positrons and protons, in tension with the standard expectation from energy losses, would still requires an explanation.

Many authors have investigated non-astrophysical sources like annihilation or decaying of dark matter particles. The existence of dark matter as the dominant gravitational mass in the universe is well established from many different measurements, but its actual nature is still completely unknown. An attractive explanation involves extending the standard model of particle physics to add a new particle (or particles) that could comprise the dark matter. There are a multitude of possibilities here, but a well motivated candidate is a weakly interacting massive particle with mass ranging from GeV to few-TeV. These dark mater particles could annihilate in Standard-Model particles. Indeed, already 20 years ago a rise in the positron fraction at high energy due to the annihilation of dark matter particles in the galactic halo was postulated (e.g. [205]). However, this explanation is confronted by two major challenges: the asymmetry (e.g. [206]) between leptonic (positron) and hadronic (antiproton, see next section) data; a pair-annihilation cross section much larger than the thermal value and disfavored by independent gamma-ray observations (e.g. in the directions of dwarf spheroidal galaxies [207]). Various solution were put forward. For example, it was speculated the existence of new light (mass $<$ 1 GeV) bosons to mediate the annihilation, hence suppressing kinematically the antiproton production [208]. The annihilation cross section issue could be solved with approaches that boost it like a Sommerfeld enhancement (e.g. [209]), near-resonance effects (e.g. [210,211]), etc. Also the possibility that dark matter particles could decay, hence reducing the tension with gamma-ray observation, was considered (e.g. [212]).

Notwithstanding the hundreds of works and ideas dealing with novel sources of positrons, several authors pointed out that the similarity of the positron spectrum (i.e. comparable spectral index) to the proton and, as it will be shown later on, to the antiproton spectrum may indicate that the cosmic-ray propagation is not properly understood. Hence, cosmic-ray positrons could have a pure secondary origin if their residence time in the Galaxy is significantly smaller than that inferred from cosmic-ray nuclei [213] (see also [214]). This would result in similar spectral shapes for cosmic-ray positron and electron at high energies with a softening caused by energy losses at energies of $\sim$ 1 TeV. This would explain the observed break in the all-electron spectrum (see Fig. 31) but appears not consistent with the electron and positron fluxes measured by AMS-02 (see Fig. 32) that show a break in the positron spectrum at sub-TeV energies, i.e. lower energies than for the electron spectrum. While more precise data are required for a conclusive result, this interpretation is in tension with existing e^- and e^+ data. A possible solution required that most of the matter traversed by cosmic rays is located in small regions near the cosmic-ray sources while the matter density in the Galaxy is significantly smaller (nested

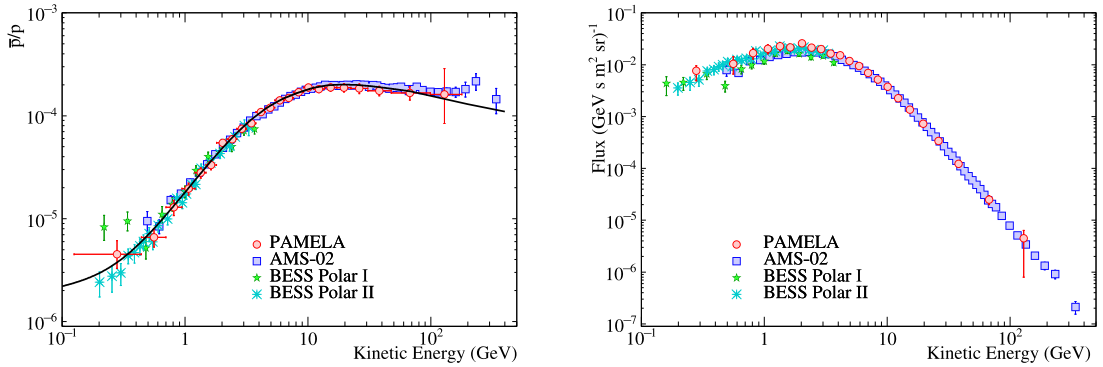

Fig. 34. The most recent measurements of the antiproton-to-proton flux ratio, left, and of the antiproton energy spectrum, right, measured by BESS-Polar I & II [223,224], PAMELA [62,225,226] and AMS-2 [63,227]. The solid line shows the calculation for pure secondary production of antiprotons during the propagation of cosmic-rays in the galaxy [183,184].

leaky box model [215]). This model can explain both the observed positron and electron spectra [157] but, as discussed in Section 3.2.4, fails to explain the measured secondary nuclei (e.g. boron) high energy spectrum. In conclusion, while viable solutions, explanations of positrons as pure secondary particles appear less appealing than models that require new sources of positrons (and electrons).

3.2.6. Antiparticles and antinuclei

Since the first observations of cosmic-ray antiprotons in the nineteen seventies [216,217] it has been apparent that antiprotons, like positrons, probe production and transport properties of cosmic rays in the galaxy and search for evidence of exotic production mechanisms (e.g. [218]). Similarly to positrons, cosmic-ray antiprotons are produced in the interaction between cosmic rays and the interstellar matter. In addition, possible primary sources of galactic antiprotons include the annihilation of dark matter particles [219] and the evaporation of primordial black holes [220,221].

Until two decades ago, cosmic-ray antiprotons were measured by balloon-borne experiments with relatively low statistics. Recently, space-borne experiments as well as long-duration flights around Antarctica significantly extended the explored energy range with a massive increase in statistical precision. Fig. 34 shows these most recent results on the antiproton-to-proton flux ratio (left) and on the antiproton energy spectrum (right) along with a calculation for pure secondary production of antiprotons [183,184]. The experimental data reproduce the fall-off below 2 GeV, characteristic of an antiproton secondary spectrum, and are in overall agreement with pure secondary calculations in the whole energy range. The antiproton-to-proton flux ratio above a few tens of GeV appear flatter than expected by the calculation from [183,184] and remarkably similar to the proton spectrum. As previously discussed, this prompted speculation on the need for a revision of the cosmic-ray propagation models with possible solutions like the nested leaky box model [158]. Yet, standard propagation models including the most recent collider data for antiproton production cross sections seem able to produce an harder high-energy antiproton flux consistent with the measurements [222].

The agreement between experimental cosmic-ray antiproton data and expected secondary production places significant constrains on additional primary antiproton components like production from annihilation or decay of dark matter particles. This clearly affects interpretations of the cosmic-ray positron data as having a significant contribution from dark matter annihilation thus motivating the novel solutions discussed in the previous section. Nonetheless, a few authors recently claimed indications of a dark matter signal resulting from an excess in the 10–20 GeV antiproton data with respect to secondary production [228,229]. According to these authors this excess has a significance of at least 3 standard deviations accounting for propagation model uncertainties and could be explained with the annihilation to $b\bar{b}$ of dark matter particle with thermal annihilation cross section and with mass in the range of several tens of GeV [230]. Interestingly enough, the dark matter models that could explain the antiproton excess are in agreement with those that could account for the excess of GeV gamma rays observed from the Galactic center (e.g. [231]). However, tension exists with constrains on dark matter signals from dwarf galaxies [228]. Furthermore, the additional antiproton component from dark matter provides a better fit to the experimental data in 10–20 GeV region but significantly overshoot the data below a few GeV where solar modulation plays an important rule and very simplistic models were used to model it. It remains to be seen if a more appropriate approach to solar modulation could reconcile these models with a dark matter component or exacerbate the discrepancies, thus reducing the significance of these hints. If instead the cosmic-ray antiproton data are used to estimate upper limits on hadronic dark matter annihilation cross section, stringent limits are obtained comparable and even stronger that those based on gamma-ray observations of dwarf galaxies [228].

While very promising, indirect searches of dark matter with cosmic-ray antiparticles are challenged by the presence of a significant astrophysical background. However, antimatter, namely antideuterons and antihelium, may provide, if detected, potentially unambiguous results [232]. The central role of the antideuteron ($\bar{D}$) in indirect searches of dark

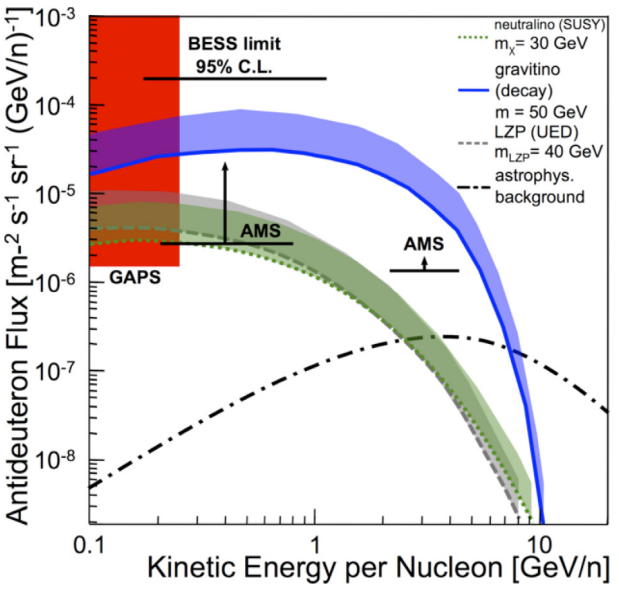

Fig. 35. The measured limit on the antideuteron flux by the balloon-borne experiment BESS [239] along with various predictions [235–238] of primary production from dark matter annihilation or decay and secondary production in the interstellar medium. The shaded bands represent the envelope, within medium and maximum effect, of model predictions obtained by considering the uncertainties on the propagation parameters [242]. The projected sensitivities of five years of operation of the space experiment AMS-02 [240] and three 35 day balloon-flights of the GAPS experiment [241] are also shown.

matter was first discussed more than 15 year ago [233], even though no antideuteron particles have yet been found in the cosmic radiation. In the framework of WIMP annihilation/decay, standard model particles, including antiprotons and antineutrons, are created and they can coalesce to form an antinuclei. Astrophysical background antinuclei can also be created when cosmic ray hadrons interact with the interstellar matter. However, because of the high production threshold needed to create an antinuclei, their spectra at low energies (below a few GeV/n) is expected to be orders of magnitude lower than those of antideuterons and antihelium resulting from plausible models of dark matter annihilation or decay [233,234]. Fig. 35 shows several predictions [235–238] of cosmic-ray antideuterons from viable dark matter models and from secondary production. The predictions are compared with upper limits from BESS [239] and projected sensitivities of five years of operation of the space experiment AMS-02 [240][6] and three 35 day balloon-flights of the GAPS experiment [241].

The situation is similar with antihelium (essentially $^3\overline{\text{He}}$) although the absolute flux is significantly suppressed as the mass number increases [234,243]. Also in this case the antihelium low energy spectrum predicted by various models of dark matter annihilation exceeds by several order of magnitude the expected astrophysical background (e.g. [243]). Currently, only experimental limits from space experiments AMS-01 [244] and PAMELA [245] and the balloon-borne experiments BESS Polar I+II [246] exist. Although, it should be noted that very recently, tantalizing hints of anti-helium candidates have been presented by the magnetic spectrometer AMS-02 [247]. Considering the extremely larger helium component observed by the experiment (about an antihelium candidate out 100 millions helium events), misidentification of helium nuclei as antihelium in the magnetic spectrometer cannot be excluded. Nonetheless, even if the results will be published and substantiated by robust simulation, the enormous scientific importance of the results (e.g. [248]) will mandate confirmation by another experiment with different systematic uncertainties.

3.2.7. The ultra high energy cosmic rays

After 80 years from the first measurement of EASs by Pierre Auger [249], the origin and nature of UHECRs ($\geq 10^{19}$ eV) remain unsolved. Where do UHECRs come from? What are these extreme cosmic accelerators and how do they accelerate to such high energies? Which is their composition? Does it evolve as a function of energy? Many sources have been conjectured, covering a large range of astrophysical objects from extremely fast-spinning young pulsars, across active galactic nuclei and starburst galaxies, to gamma-ray bursts.

Detection of UHECRs is rather challenging due to extremely low particle fluxes, around 1 particle per km^2 per century reaching the Earth at energies of the order of 5×10^{19} eV. A series of observations have been performed over many years by very large on-ground arrays of surface detectors, measuring the charged particles produced by the showers, and a system

[6] Updated for measurement time, geomagnetic cutoff model, background fluxes [241].

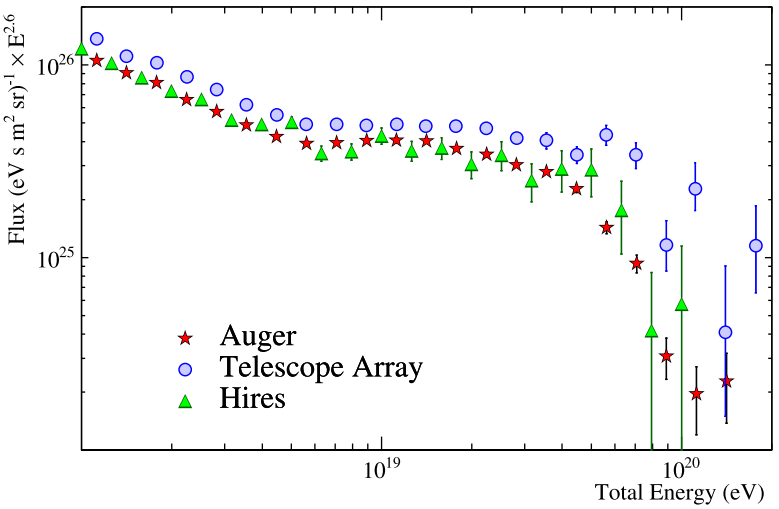

Fig. 36. The UHECR energy spectrum measured by the Hires [9], Pierre Auger observatory [10] and telescope array [251]. The fluxes are multiplied by $E^{2.6}$, where E is the total energy in eV.

of optics telescopes to detect fluorescence light. The largest installation is the Pierre Auger Observatory in Mendoza, Argentina, southern hemisphere, with 1600 water Cherenkov detectors distributed in 3000 km^2, mostly sensitive to the muon component, and 24 optics telescopes located in four stations. In the northern hemisphere, a smaller installation is the Telescope Array (TA) in Utah, USA, spread-out over 700 km^2, and based on plastic scintillator detectors mostly sensitive to the electromagnetic component. Nowadays, TA is planned to be enlarged by a factor 4. An overlapping reduced region of the sky can be observed by the two experiments.

The UHECRs energy spectra measured by the HiRes fluorescence experiment [9], Pierre Auger Observatory [10,250] and TA [251] observatories up to energies higher than 10^{20} eV are shown in Fig. 36. They agree within systematic errors below 10^{19} eV. However, a large difference remains at and beyond $E = 5 \times 10^{19}$ eV. Although significant differences, not well understood, remain also in the common sky, fundamental variation between the northern and southern UHECR skies are not ruled out.

The UHECR energy spectrum can be roughly described by a twice-broken power laws. The first break is a pronounced hardening around 5×10^{18} eV (the so-called "ankle" feature), the second is an abrupt softening of the spectrum above $E \approx 5 \times 10^{19}$ eV. This suppression in the spectrum was independently predicted by Greisen [11] and Zatsepin & Kuz'min [12] 55 years ago, just after the discovery of the cosmic microwave background (CMB). They observed that pion-producing interactions between extremely energetic protons and CMB photons,

$$p + \gamma_{CMB} \rightarrow \Delta^+ \rightarrow p + \pi^0, n + \pi^+$$

should produce a cutoff at about 5×10^{19} eV, known today as the GZK effect.

Photo-dissociation of heavier nuclei on cosmic backgrounds, from microwave to ultraviolet, equally produces a break in energy spectrum. These energy losses limit the volume of space in which UHECRs can originate to be observed at Earth, with the maximum arrival distance, the horizon of the events, at a few tens of Mpc, for protons and irons of energy above 6×10^{19} eV. Therefore, the universe volume sampled by UHECRs, is, just a small fraction of the total size of the visible Universe. However, since the acceleration limit of the known celestial objects is of the order of 10^{20} eV, it is possible that the spectral steepening is also due to an acceleration limit of the source in addition to the GZK effect. If unknown and more powerful astronomical objects exist, a rise in the energy spectrum should be found at energies currently unexplored.

The ankle is currently explained in terms of a Galactic and extragalactic transition for UHECR production site. However, it could be related also to photo-electron-pair production in interaction between the protons with CMB [252]:

$$p + \gamma_{CMB} \rightarrow p + e^+e^-.$$

About the composition of UHECRs, the measurements of both TA and Auger ([253] and ref. herein) agree for a predominantly light composition at around the ankle. At higher energies Auger data suggest a gradual increase of the average mass of cosmic rays with energy with a mean baryon number $A \approx 14 - 20$ at $E \approx 10^{19.5}$ eV. This increase cannot currently neither be confirmed nor ruled out by TA because of statistical limitations.

Concerning anisotropies in the arrival directions of high energy cosmic rays, these are highly isotropic below the ankle [253]. At higher energies, Galactic and extragalactic deflections of UHECR nuclei are expected to smear point sources into warm/hot spots. Auger [254] and TA [255,256] find intriguing hints of anisotropies at small and intermediate angular-scales in the observed sky in the two hemisphere, respectively. Particularly compelling (at more than a 5.2σ

level of significance) is the observation by the Pierre Auger Observatory of a large-scale dipolar anisotropy in the arrival direction of cosmic rays with energies above 8 EeV [19]. The magnitude and direction of the anisotropy strongly point to an extragalactic origin for these ultra-high energy particles.

A decisive step forward in addressing all these unsolved issues may come from space-based observations. Going to space to look down at the atmosphere is realistically the future of the UHECR investigations.

The ultimate science objective of a space mission for the study of UHECR is the discovery of the sources of cosmic rays, thus opening a new field of astronomy. The target can be reached exploring the UHECR energy range around and beyond 10^{20} eV, energies at which particle deflection by extra-galactic and galactic magnetic fields is weak, and the number of UHECR powering sources is small due to attenuation effects. Precise measurements of the trans-GZK energy spectrum and the study of anisotropies in the extreme-energy sky are the basis for such investigations.

Exploratory objectives, which depend on the actual nature of extreme-energy cosmic-ray fluxes, are the study of cosmogenic neutrinos, by identification of weakly interacting events via the positions of the first interaction point and of the shower maximum and the discovery of UHE gamma rays, whose shower maximum is strongly affected by geomagnetic and Landau–Migdal–Pomeranchuk (LPM) effects.

The exploration of a top-down scenario, in which UHECRs are produced by the decay or annihilation of a Super-Heavy Particle, with mass $\sim 10^{22} - 10^{25}$ eV is another topic of this research. The end products of such a process should be neutrinos and gamma rays, with an abundance two or three times larger than nucleons.

Observing the Cherenkov light of air showers will provide information about hadronic interaction physics by estimating the muon richness of the UHECR air showers [257]. Recently the Pierre Auger Collaboration reported a significant excess in the number of muons of a few tens of percent over expectations computed using extrapolations of LHC-tuned hadronic interaction models [258]. This discrepancy may be interpreted as a possible signal of physics beyond the Standard Model (for an in-depth discussion see [259]).

Another fascinating investigation that can be performed by using the UHECR detection methodology is the search of Strange Quark Matter (SQM), a theoretically predicted bound state of up, down, and strange quarks [260]. This matter should be absolutely stable [261] and could form the true ground state of hadronic matter. These particles might be produced inside neutron stars, perhaps via WIMP annihilation [262], or have cosmological origin. The high density of the SQM nuggets, that produces a long and constant signal in the atmosphere, their interstellar origin and speed, should permit a clear identification of this matter while crossing the atmosphere.

The just deployed space missions TUS and Mini-EUSO, described in Section 2.4.1, are taking data providing both validation of the space approach and first results on UHECR. Preliminary analysis of the cosmic ray mode data collected by TUS shows the presence of several events which look like some of the features of cosmic ray showers. One, TUS161003, was detected on October 3, 2016, high in the atmosphere and in perfect observational conditions. Anthropic or atmospheric sources were excluded by a detailed analysis, while the shape and kinematics of the signal suggest as natural candidate an EAS generated by an UHECR. However, this cosmic ray should have an energy of the order of 10^{21} eV to provide the observed signal, never detected by ground-based experiments. The limited total exposure of TUS reduces the possibility recording such an energetic cosmic particle to an extremely low level. Very accurate simulations have instead shown that the development of the TUS161003 event could agree with an EAS originated by a massive relativistic dust grain. Mini-EUSO, now in commissioning phase, has as main objectives the investigation of the environmental conditions for the study of UHECR and the search for the Strange Quark Matter. In addition, the instrument will provide a large amount of data on atmospheric phenomena and on the Earth's UV emissions.

However, the most important results for UHECR physics from space are expected from the KYPVE-EUSO (K-EUSO) [263,264] experiment. This mission is the result of a joint effort between the KLYPVE and JEM-EUSO collaborations to improve the performance of the planned Russian KLYPVE mission, by employing technologies developed for the JEM-EUSO mission. K-EUSO, led by the Russian Space Agency, will operate from the end of 2022 for a minimum of 2 years and more than 6 years if the lifetime of the ISS will be extended. The instrument has already been described in Section 2.4.1. It will be the first large detector to observe the whole UHECR sky uniformly, observing both hemispheres at the same time, achievement that is the real breakthrough of K-EUSO compared with the on ground detectors. Taking into account the energy spectra measured from Auger and TA, respectively in the northern and southern hemispheres, K-EUSO will detect each year over 170 events above 5.7×10^{19} eV. This number, although rather small, will allow to confirm or disprove in two years the still unsolved difference in the energy spectrum of the UHECR as measured in the two hemispheres, to study possible UHECR anisotropies over various angular scales, confirming or ruling out the uncertain hotspots in the sky claimed by the two major on ground experiments.

4. Conclusions and outlook

In the past few years significant advances have been made in the field of cosmic rays thanks to several new experiments many of which operating in space. The large amount of new data produced by these experiments have opened an era of precision in the study of cosmic rays (e.g. [265,266]). However, these data have also open new questions suggesting the need to revise the current theoretical understanding of the origin and propagation of cosmic rays (e.g. [267,268]). Such endeavor will also require bigger and more sophisticated instrumentation. Therefore, new space-borne apparatus are planned for the near future, a few are in the development phase while others are still in the design and approval phase.

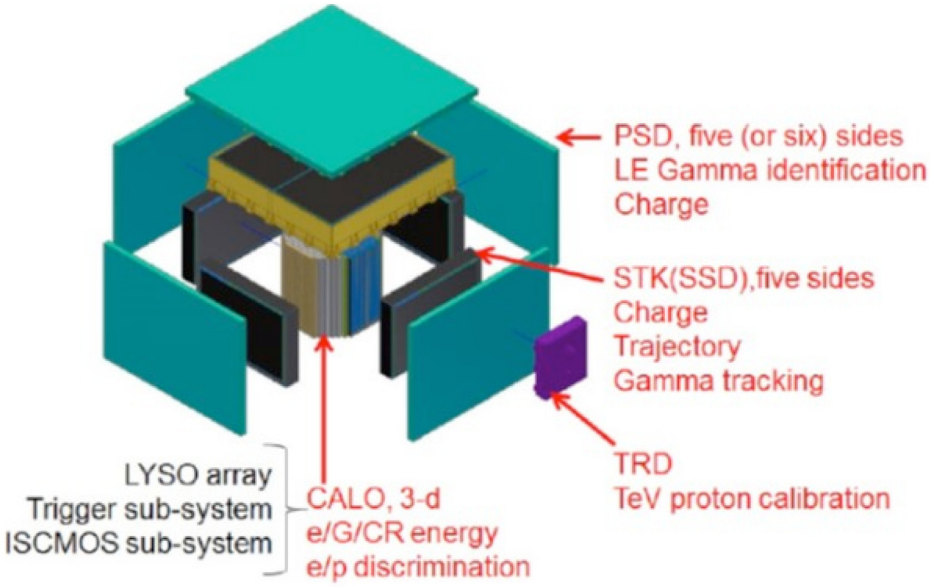

Fig. 37. Schematic diagram of the HERD apparatus [269].

The presence of a hardening in the few hundred GeV region of the cosmic-ray energy spectra has been undoubtedly established by the most recent direct measurements. However, the universality of this hardening, i.e. its presence in the energy spectrum of all cosmic-ray species, requires the extension of the measurements to heavier cosmic-ray nuclei. In the TeV regions hints of additional features in the proton cosmic-ray spectrum have been reported by various experiments [6,119–121]. However, this requires confirmation with more precise data as well as extending this investigation to the energy spectra of heavier components. Finally, no direct measurements of the cosmic-ray spectra in the knee region exist. All these studies are required to firmly established if the standard paradigm of cosmic rays is still valid with proper tuning or require to be significantly modified if not replaced at all with a new model [268].

To address these issues by extending the direct measurement of the cosmic-ray energy spectra up to the knee region and up to tens of TeV for electrons, the HERD experiment has been proposed to be installed on board of the future Chinese space station around 2025 [269]. The HERD apparatus, shown in Fig. 37, will be composed of a 3-D cubic calorimeter (CALO), based on the CaloCube approach described in Section 2.2.2, surrounded by a tracking system (STK) of microstrip silicon detectors. The whole apparatus will be covered by plastic scintillators (PSD) plus a Transition Radiation Detector (TRD) located on one lateral side. The effective geometrical acceptance of HERD is expected to be > 3 m^{2}sr for electrons and gamma rays and > 2 m^{2}sr for protons and heavier cosmic rays. The design energy resolution is about 1% for electrons and gamma-rays beyond 200 GeV, and 20% for protons from 100 GeV to 1 PeV. HERD is designed to make a direct measurement of the energy spectra and composition of primary cosmic rays from 10 GeV up to the PeV region. Furthermore, it will search indirectly for dark matter signatures in the energy spectra and anisotropy of high energy electrons and gamma-rays from 500 MeV to 10 TeV. Additionally, the wide FoV will allow the monitoring of the high energy gamma-ray sky from 500 MeV up to 10 TeV for gamma-ray bursts, active galactic nuclei and Galactic microquasars.

While important to address many questions concerning the origin and propagation of galactic cosmic rays and to provide useful information for indirect searches of dark matter, HERD will not be able to fully clarify the origin of the antimatter component. As discussed in Section 3.2.5, an important signature of the different scenarios put forward to interpret the electron and positron energy spectra is the different cutoff values for these spectra in the hundred GeV–TeV energy region. These energies are beyond the reach of the current magnetic-spectrometer experiments and the lack of the sign-charge separation capabilities significantly limits the ability of calorimeter-based experiments to clarify this issue. Furthermore, extending the current limits on the anisotropy of the arrival directions of positrons down to a few per mill or less may lead to the identification of nearby astrophysical objects as sources of cosmic-ray electrons and positrons. This will provide fundamental clues in understanding if cosmic-ray positrons have only an astrophysical origin or if dark matter contributes to their flux. The existing measurements on the cosmic-ray antiproton fluxes are in slight tension with the expectations of secondary production from interactions of cosmic rays with the interstellar matter. Extending the antiproton measurements into the TeV region combined with precise measurements of multi-TeV secondary cosmic-ray nuclei should allow to conclusively confirm or put to rest a dark matter contribution to the antiproton flux. Finally, the hints of anti-helium candidates suggested by the AMS-02 experiment if published will require confirmation by at least another experiment. For all these investigations two missions are under study: the Antimatter Large Acceptance Detector In Orbit (ALADInO) [270] and AMS-100 [271]. Both these experiments are designed to be placed at the Sun–Earth Lagrange

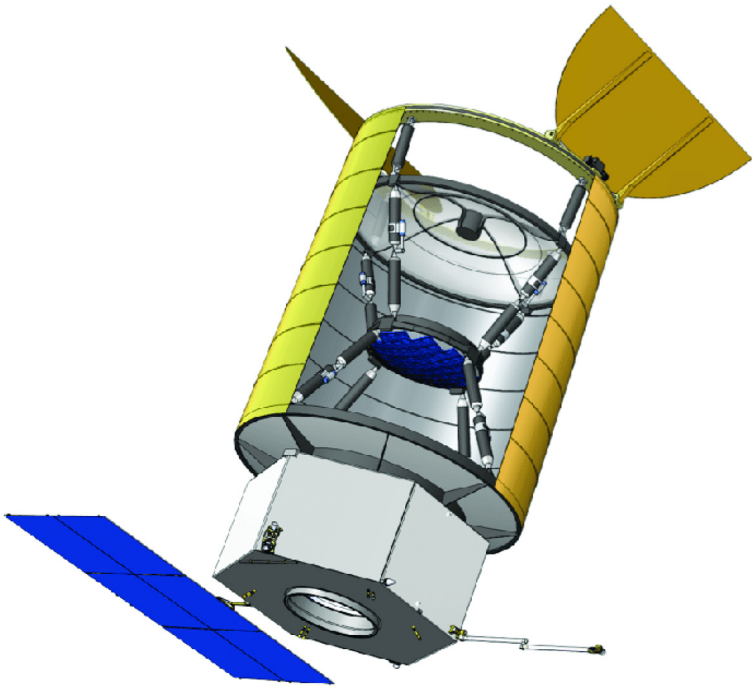

Fig. 38. A sketch of one POEMMA satellite.

Point 2 and equipped with superconducting magnets. ALADInO is designed to have a geometrical acceptance of about 10 m^2sr with an MDR greater than 20 TV and powerful particle identification provided by a 60 radiation lengths, 3.5 interaction lengths calorimeter. AMS-100 is designed to have a geometrical acceptance of 100 m^2sr with an MDR of 100 TV and equipped with a 70 radiation lengths, 4 interaction lengths calorimeter.

Concerning detection of UHECRs, a new space mission is under study: POEMMA [272] is a multi-messenger project selected by NASA for a probe mission concept study in preparation for the next decadal survey. It is an evolution of previous works on the OWL and the JEM-EUSO designs and the balloon-born EUSO-SPB1 and 2. The instrument should be placed in a circular orbit at an inclination of 28.5 degrees and an altitude of 525 km in the 2030's. POEMMA will operate in fluorescence and in Cherenkov limb-viewing mode as in EUSO-SPB2. The fluorescence observations will increase yearly of one order of magnitude the UHECR exposure compared to ground observatory arrays and two orders of magnitude compared to ground fluorescence telescopes. POEMMA will measure with high precision the spectrum, composition, and source location of the UHECRs by particle measurements at energies $E \geq 2 \times 10^{19}$ eV, opening to charged-particle astronomy. An objective of POEMMA is also the detection of neutrinos with energies above 2×10^{19} eV through fluorescence observations of neutrino induced EASs. In the Cherenkov limb-viewing mode, it will search for optical Cherenkov signals of upward-moving EASs generated by τ-lepton decays produced by ν_τ interactions in the Earth. In the Cherenkov mode, it will perform also UHECR fluorescence observations.

POEMMA will also probe physics beyond the Standard Model of particle physics and will perform measurements of pp cross-section at 238 TeV center-of-mass energy. By observing the Cherenkov light of strongly inclined EASs, POEMMA will be able to resolve the muon component from the electromagnetic ones since muons propagate over much larger distances than the electrons and photons, with distinct Cherenkov light topologies [257]. Measuring the muon component of EASs for UHECRs, POEMMA will provide information to test hadronic interaction models beyond colliders energies.

The study of Transient Luminous Events and the meteors and nuclearites are also mission objectives. POEMMA instrument will consist of two identical satellites flying at 525 km altitude in a configuration that permits to observe overlapping regions during moonless nights at angles ranging from nadir to just above the limb of the Earth, but also with independent pointing strategies. Each satellite, shown in Fig. 38, will be equipped with Schmidt-based mirror optics with a large spherical primary mirror (4 m diameter), a thin refractive aspheric aberration corrector lens (3.3 m diameter) at its center of curvature, and a convex spherical focal surface (1.61 m diameter). This particular system will provide a large collection aperture (6.39 m^2) and a large field-of-view (45° full FoV).

The focal surface (FS) of each telescope will be equipped with a hybrid of two types of cameras: about 90% of the FS will be dedicated to the fluorescence camera, while the Cherenkov camera will occupy the crescent moon shaped edge of the FS which images the limb of the Earth. The stereo images of the EAS will be used to determine the energy, direction, and composition of UHECR from Nadir to just below the Earth's limb. The much faster Cherenkov camera will cover 9° of

the FoV from the edge and will record EASs produced by UHECRs above the limb of the Earth and showers from τ-lepton decays below the Earth's limb induced by ν_τ interactions in the Earth.

References

[1] P. Carlson, A. De Angelis, Eur. Phys. J. H 35 (2010) 309.
[2] N.L. Grigorov, et al., Proc. 12th Int. Cosmic Ray Conf. Vol. 6, 1971, p. 1746.
[3] J.A. Earl, Phys. Rev. Lett. 6 (1961) 125.
[4] P. Meyer, R. Vogt, Phys. Rev. Lett. 6 (1961) 193.
[5] O. Adriani, et al., Riv. Nuovo Cimento 40 (2017) 1.
[6] Y.S. Yoon, et al., Astrophys. J. 839 (2017) 5.
[7] M.A.K. Glasmacher, et al., Astropart. Phys. 10 (1999) 291.
[8] M.G. Aartson, et al., Phys. Rev. D 88 (2013) 042004.
[9] R. Abbasi, et al., Phys. Rev. Lett. 100 (2008) 101101.
[10] V. Verzi, et al., Proc. Sci. ICRC2019 (2019) 450.
[11] K. Greisen, Phys. Rev. Lett. 16 (1966) 748.
[12] G.T. Zatsepin, V.A. Kuzmin, JETP Lett. 4 (1966) 78.
[13] A. Giuliani, et al., Astrophys. J. Lett. 742 (2011) L30.
[14] A.A. Abdo, et al., Science 327 (2010) 1103.
[15] M. Tavani, et al., Astrophys. J. Lett. 710 (2010) L151.
[16] S. Funk, Adv. Space Res. 41 (2008) 464.
[17] J. Vink, Proc. The X-ray Universe 2005, 2005, p. 319.
[18] A. Calvez, A. Kusenko, S. Nagataki, Phys. Rev. Lett. 105 (2010) 091101.
[19] A. Aab, et al., Science 357 (2017) 1266.
[20] K. Kotera, A.V. Olinto, Annu. Rev. Astron. Astrophys. 49 (2011) 119.
[21] L.A. Anchordoqui, Phys. Rep. 801 (2019) 1.
[22] V.S. Berezinskii, S.V. Bulanov, V.A. Dogiel, V.S. Ptuskin, Astrophysics of Cosmic Rays, North Holand, Amsterdam, 1990.
[23] O. Adriani, et al., Nucl. Instrum. Methods A 511 (2003) 72.
[24] S. Straulino, et al., Nucl. Instrum. Methods A 530 (2004) 168.
[25] P. Picozza, et al., Astropart. Phys. 27 (2007) 296.
[26] C. Patrignani, et al., Chin. Phys. C 40 (2016) 100001.
[27] S.A. Voronov, et al., Proc. 20th Int. Cosmic Ray Conf. Vol. 4, 1987, p. 49.
[28] J.A. De Shong, R.H. Hildebr, P. Meyer, Phys. Rev. Lett. 12 (1964) 3.
[29] R. Battiston, et al., Proc. 29th Int. Cosmic Ray Conf. Vol. 10, 2005, p. 151.
[30] R.L. Golden, et al., Nucl. Instrum. Methods A 113 (1973) 349.
[31] A. Yamamoto, Progr. Theoret. Phys. Suppl. 151 (2003) 240.
[32] M.A. Green, et al., IEEE Trans. Magn. MAG-23 (1987) 1240.
[33] R.L. Golden, et al., Nuovo Cimento B 105 (1990) 191.
[34] J. Alcaraz, et al., Phys. Lett. B 490 (2000) 27.
[35] S. Torii, et al., Proc. Sci. 2015 (2016) 581.
[36] M.J. Ryan, J.F. Ormes, V.K. Balasubrahmanyan, Phys. Rev. Lett. 28 (1972) 985.
[37] J. Chang, et al., Astropart. Phys. 95 (2017) 6.
[38] O. Adriani, et al., Astropart. Phys. 96 (2017) 11.
[39] L. Pacini, et al., J. Phys. Conf. Ser. 928 (2017) 012013.
[40] M. Aguilar, et al., Phys. Rev. Lett. 113 (2014) 221102.
[41] O. Adriani, et al., Phys. Rev. Lett. 106 (2011) 201101.
[42] W.R. Binns, et al., Astrophys. J. 788 (2014) 18.
[43] A.W. Labrador, et al., Proc. Sci. ICRC2017 (2018) 167.
[44] N.E. Walsh, et al., Proc. Sci. ICRC2017 (2018) 201.
[45] J. Seguinot, T. Ypsilantis, Nucl. Instrum. Methods 142 (1977) 377.
[46] J. Buckley, et al., Astrophys. J. 429 (1994) 736.
[47] M. Ave, et al., Nucl. Instrum. Methods A 654 (2011) 140.
[48] M.H. Israel, R.E. Streimatter, S.P. Swordy, AIP Conf. Proc. 458 (1999) 114.
[49] H.S. Ahn, et al., Nucl. Instrum. Methods A 579 (2007) 1034.
[50] E.S. Seo, et al., Proc. 29th Int. Cosmic Ray Conf. Vol. 3, 2005, p. 101.
[51] V. Bidoli, et al., Astrophys. J. 132 (2001) 365.
[52] V. Bidoli, et al., Nucl. Instrum. Methods A 424 (1999) 414.
[53] G. Furano, et al., Adv. Space Res. 31 (2003) 351.
[54] E.C. Stone, et al., Space Sci. Rev. 86 (1998) 1.
[55] T. Hams, et al., Astrophys. J. 611 (2004) 892.
[56] M. Ambriola, et al., Nucl. Phys. B 78 (199) 32.
[57] P. Papini, et al., Astrophys. J. 615 (2004) 269.
[58] D. Müller, K.K. Tang, Astrophys. J. 312 (1987) 183.
[59] M. Ackermann, et al., Phys. Rev. Lett. 108 (2012) 011103.
[60] M. Chantell, et al., Nature 367 (1994) 25.
[61] S.A. Stephens, Astron. Astrophys. 149 (1985) 1.
[62] O. Adriani, et al., Phys. Rev. Lett. 102 (2009) 051101.
[63] M. Aguilar, et al., Phys. Rev. Lett. 117 (2016) 091103.
[64] O. Adriani, et al., Science 332 (2011) 69.
[65] R.L. Golden, et al., Nucl. Instrum. Methods A 306 (1991) 366.
[66] K. Sakai, et al., Proc. Sci. ICRC2017 (2018) 174.
[67] S. Torii, et al., Proc. Sci. ICRC2015 (2015) 581.
[68] O. Adriani, et al., Phys. Rev. Lett. 119 (2019) 181101.
[69] Y. Asaoka, et al., J. Phys. Conf. Ser. 1181 (2019) 012003.

[70] O. Adriani, et al., Phys. Rev. Lett. 111 (2013) 081102.
[71] M. Aguilar, et al., Phys. Rev. Lett. 122 (2019) 041102.
[72] R. Benson, J. Linsley, Proc. 17th Int. Cosmic Ray Conf. Vol. 9, 1981, p. 145.
[73] Y. Takahashi, New J. Phys. 11 (2009) 065009.
[74] J.H. Adams, et al., Exp. Astron. 40 (2015).
[75] P. Klimov, M. Casolino, Proc. Sci. ICRC2017 (2017) 412.
[76] P. Klimov, et al., Space Sci. Rev. 8 (2017) 1.
[77] M. Casolino, et al., Proc. Sci. ICRC2017 (2017) 369.
[78] M. Casolino, et al., Proc. Sci. ICRC2019 (2019) 212.
[79] J.H. Adams, et al., Exp. Astron. 40 (2015) 281.
[80] S. Bacholle, et al., Proc. Sci. ICRC2017 (2017) 384.
[81] J. Eser, et al., Proc. Sci. ICRC2019 (2019) 247.
[82] D.V. Reames, Space Sci. Rev. 90 (1999) 413.
[83] E.N. Parker, Phys. Rev. 110 (1958) 1445.
[84] E.N. Parker, Interplanetary Dynamical Processes, Interscience Publishers, New York, USA, 1963.
[85] E.N. Parker, Planet. Space Sci. 13 (1965) 9.
[86] E.C. Stone, R.E. Vogt, F.B. McDonald, et al., Space Sci. Rev. 21 (1977) 355.
[87] A.W. Strong, I.V. Moskalenko, Astrophys. J. 509 (1998) 212.
[88] A. Vittino, C. Evoli, D. Gaggero, PoS 301 (2018).
[89] M.S. Potgieter, Living Rev. Solar Phys. 10 (2013) 3.
[90] M.S. Potgieter, et al., Sol. Phys. 289 (2014) 301.
[91] K. Abe, et al., Astrophys. J. 822 (2015) 2.
[92] O. Adriani, et al., Astrophys. J. 765 (2013) 91.
[93] M. Martucci, et al., Astrophys. J. 854 (2018) l2.
[94] M. Aguilar, et al., Phys. Rev. Lett. 121 (2018) 051101.
[95] O. Adriani, et al., Astrophys. J. 810 (2015) 2.
[96] M. Aguilar, et al., Phys. Rev. Lett. 121 (2018) 051102.
[97] M.S. Potgieter, et al., Astrophys. J. 810 (2015) 2.
[98] R.A. Caballero-Lopez, H. Moraal, J. Geophys. Res. 109 (2004) A01101.
[99] O.P.M. Aslam, et al., Astrophys. J. 873 (2019) 70.
[100] O. Adriani, et al., Phys. Rev. Lett. 116 (2016) 241105.
[101] R.R. Nndanganeni, M.S. Potgieter, Adv. Space Res. 58 (2016) 453.
[102] R. Munini, et al., Astrophys. J. 853 (2018) 76.
[103] V. Di Felice, R. Munini, E.E. Vos, M.S. Potgieter, Astrophys. J. 834 (2017) 89.
[104] D. Caprioli, A. Spitkovsky, Astrophys. J. 783 (2014) 91.
[105] A.R. Bell, Mon. Not. R. Astron. Soc. 182 (1978) 147.
[106] R.D. Blandford, J.P. Ostriker, Astrophys. J. Lett. 221 (1978) L29.
[107] V.L. Ginzburg, S.I. Syrovatskii, The Origin of Cosmic Rays, Macmillan, New York, 1964.
[108] A.W. Strong, I.V. Moskalenko, V.S. Ptuskin, Annu. Rev. Nucl. Part. Sci. 57 (2007) 285.
[109] M.J. Ryan, J.F. Ormes, V.K. Balasubrahmanyan, Phys. Rev. Lett. 28 (1972) 985.
[110] I.P. Ivanenko, et al., Proc. 23rd Int. Cosmic Ray Conf. Vol. 2, 1993, p. 17.
[111] K. Asakimori, et al., Astrophys. J. 502 (1998) 278.
[112] M. Boezio, et al., Astrophys. J. 518 (1999) 457.
[113] W. Menn, et al., Astrophys. J. 553 (2000) 281.
[114] T. Sanuki, et al., Astrophys. J. 545 (2000) 1135.
[115] M. Boezio, et al., Astropart. Phys. 19 (2003) 583.
[116] M. Hareyama, et al., J. Phys. Conf. Ser. 31 (2006) 159.
[117] M. Boezio, E. Mocchiutti, Astropart. Phys. 39–40 (2012) 95.
[118] M. Aguilar, et al., Phys. Rev. Lett. 114 (2015) 171103.
[119] E. Atkin, et al., JETP Lett. 108 (2018) 5.
[120] O. Adriani, et al., Phys. Rev. Lett. 122 (2019) 181102.
[121] Q. Yuan, et al., Proc. Sci. ICRC19 (2019) 017.
[122] A.D. Panov, et al., Bull. Russ. Acad. Sci. Phys. 73 (2009) 564.
[123] K. Abe, et al., Astrophys. J. 822 (2016) 65.
[124] H.S. Ahn, et al., Astrophys. J. Lett. 714 (2010) L89.
[125] T. Sanuki, et al., Adv. Space Res. 27 (2001) 761.
[126] P. Lipari, Astropart. Phys. 97 (2018) 197.
[127] V.J. Zatsepin, N.V. Sokolskaya, Astron. Astrophys. 458 (2006) 1.
[128] P. Blasi, Braz. J. Phys. 44 (2014) 426.
[129] P. Blasi, E. Amato, P.D. Serpico, Phys. Rev. Lett. 109 (2012) 061101.
[130] N. Tomassetti, Astrophys. J. Lett. 752 (2012) L13.
[131] C. Evoli, P. Blasi, G. Morlino, R. Aloisio, Phys. Rev. Lett. 121 (2018) 021102.
[132] O. Adriani, et al., Astrophys. J. 818 (2016) 68.
[133] M. Aguilar, et al., Phys. Rev. Lett. 115 (2015) 211101.
[134] Y.S. Yoon, et al., Astrophys. J. 728 (2011) 122.
[135] H.S. Ahn, et al., Astrophys. J. Lett. 707 (2009) 593.
[136] F. Gahbauer, et al., Astrophys. J. 607 (2004) 333.
[137] M. Ave, et al., Astrophys. J. 678 (2008) 262.
[138] A. Obermeier, et al., Astrophys. J. 742 (2011) 14.
[139] P.D. Serpico, Proc. Sci. ICRC2015 (2016) 009.
[140] P. Blasi, E. Amato, J. Cosmol. Astropart. Phys. 12015 (2012) 010.
[141] A. Hanusch, T. Liseykina, M.A. Malkov, Astrophys. J. 872 (2019) 108.
[142] A.E. Vladimirov, et al., Astrophys. J. 752 (2012) 68.
[143] M.A. Malkov, P.H. Diamond, R.Z. Sagdeev, Phys. Rev. Lett. 108 (2012) 081104.
[144] O. Adriani, et al., Astrophys. J. 791 (2014) 93.

[145] M. Aguilar, et al., Phys. Rev. Lett. 119 (2017) 251101.
[146] M. Aguilar, et al., Phys. Rev. Lett. 120 (2018) 021101.
[147] J.P. Meyer, L.O. Drury, D.C. Ellison, Astrophys. J. 487 (1997) 182.
[148] D.C. Ellison, L.O.C. Drury, J.P. Meyer, Astrophys. J. 487 (1997) 197.
[149] B.F. Rauch, et al., Astrophys. J. 697 (2009) 2083.
[150] R.P. Murphy, et al., Astrophys. J. 831 (2016) 148.
[151] M.H. Israel, et al., Proc. 36th Int. Cosmic Ray Conf. 2019.
[152] M.E. Wiedenbeck, et al., Astrophys. J. Lett. 523 (1999) L61.
[153] G.A. de Nolfo, et al., Proc. 29th Int. Cosmic Ray Conf. Vol. 3, 2005, p. 61.
[154] H.S. Ahn, et al., Astropart. Phys. 30 (2008) 133.
[155] A. Obermeier, et al., Astrophys. J. 752 (2012) 69.
[156] R. Aloisio, P. Blasi, P. Serpico, Astron. Astrophys. 583 (2015) A95.
[157] R. Cowsik, B. Burch, Phys. Rev. D 82 (2010) 023009.
[158] R. Cowsik, T. Madziwa-Nussinov, Astrophys. J. 827 (2016) 119.
[159] N.E. Yanasak, et al., Astrophys. J. 563 (2001) 768.
[160] F. Donato, D.D. Maurin, R. Taillet, Astron. Astrophys. 381 (2001) 539.
[161] W. Menn, et al., Astrophys. J. 862 (2018) 141.
[162] J. Beatty, et al., Proc. Sci. ICRC2017 (2018) 226.
[163] P. Picozza, M. Boezio, Astropart. Phys. 43 (2013) 163.
[164] K. Koyama, et al., Nature 378 (1995) 255.
[165] G.E. Allen, et al., Astrophys. J. Lett. 487 (1997) L97.
[166] F. Aharonian, et al., Nature 464 (2007) 235.
[167] T. Kobayashi, Y. Komori, K. Yoshida, J. Nishimura, Astrophys. J. 601 (2004) 340.
[168] T. Delahaye, et al., Astron. Astrophys. 524 (2010) A51.
[169] J. Nishimura, et al., Astrophys. J. 238 (1980) 394.
[170] J. Chang, et al., Nature 456 (2008) 362.
[171] S. Abdollahi, et al., Phys. Rev. D 95 (2017) 082007.
[172] G. Ambrosi, et al., Nature 552 (2017) 63.
[173] O. Adriani, et al., Phys. Rev. Lett. 120 (2018) 261102.
[174] F. Aharonian, et al., Phys. Rev. Lett. 101 (2008) 261104.
[175] F. Aharonian, et al., Astron. Astrophys. 508 (2009) 561.
[176] D. Borla Tridon, et al., 2011, arXiv:1110.4008.
[177] A. Archer, et al., Phys. Rev. D 98 (2018) 062004.
[178] S. Recchia, et al., Phys. Rev. D 99 (2019) 103022.
[179] P. Mertsch, J. Cosmol. Astropart. Phys. 1811 (2018) 045.
[180] M. Aguilar, et al., Phys. Rev. Lett. 122 (2019) 101101.
[181] M. Aguilar, et al., Phys. Rev. Lett. 122 (2019) 041102.
[182] I.V. Moskalenko, A.W. Strong, Astrophys. J. 493 (1998) 694.
[183] A.E. Vladimirov, Comput. Phys. Comm. 182 (2011) 1156.
[184] https://galprop.stanford.edu/webrun/.
[185] R.L. Golden, et al., Astrophys. J. Lett. 457 (1996) L103.
[186] S.W. Barwick, et al., Astrophys. J. Lett. 482 (1997) L191.
[187] M. Boezio, et al., Astrophys. J. 532 (2000) 653.
[188] J. Alcaraz, et al., Phys. Lett. B 484 (2000) 10.
[189] M. Aguilar, et al., Phys. Lett. B 670 (2008) 103.
[190] J. Clem, P. Evenson, J. Geophys. Res. 114 (2009) A10.
[191] O. Adriani, et al., Phys. Rev. Lett. 116 (2016) 241105.
[192] A.K. Harding, R. Ramaty, Proc. 20th Int. Cosmic Ray Conf. Vol. 2, 1987, p. 92.
[193] A.M. Atoian, F.A. Aharonian, H.J. Volk, Phys. Rev. D 52 (1995) 3265.
[194] D. Hooper, P. Blasi, P.D. Serpico, J. Cosmol. Astropart. Phys. 0901 (2009) 025.
[195] A.U. Abeysekara, et al., Science 358 (2017) 911.
[196] H. Yuksel, M.D. Kistler, T. Stanev, Phys. Rev. Lett. 103 (2009) 051101.
[197] D. Hooper, I. Cholis, T. Linden, Phys. Rev. D 96 (2017) 103013.
[198] S. Profumo, J. Reynoso-Cordova, N. Kaaz, M. Silverman, Phys. Rev. D 97 (2018) 123008.
[199] C. Evoli, T. Linden, G. Morlino, Phys. Rev. D 98 (2018) 063017.
[200] R. López-Coto, G. Giacinti, Mon. Not. R. Astron. Soc. 479 (2018) 4526.
[201] R. López-Coto, R.D. Parsons, J.A. Hinton, G. Giacinti, Phys. Rev. Lett. 121 (2018) 251106.
[202] G. Giacinti, Proc. 36th Int. Cosmic Ray Conf. 2019.
[203] M.A. Malkov, P.H. Diamond, R.Z. Sagdeev, Phys. Rev. D 94 (2016) 063006.
[204] R. Diesing, D. Caprioli, 2019, arXiv:1905.07414.
[205] M.E.M. Kamionkowski, Turner, Phys. Rev. D 43 (1991) 1774.
[206] M. Boezio, et al., New J. Phys. 11 (2009) 105023.
[207] M. Ackermann, et al., Phys. Rev. Lett. 115 (2015) 231301.
[208] I. Cholis, D.P. Finkbeiner, L. Goodenough, N. Weiner, J. Cosmol. Astropart. Phys. 0912 (2009) 007.
[209] N. Arkani-Hamed, D.P. Finkbeiner, T.R. Slatyer, N. Weiner, Phys. Rev. D 79 (2009) 015014.
[210] D. Feldman, Z. Liu, P. Nath, Phys. Rev. D 79 (2009) 063509.
[211] M. Ibe, H. Murayama, T.T. Yanagida, Phys. Rev. D 79 (2009) 095009.
[212] E. Nardi, F. Sannino, A. Strumia, J. Cosmol. Astropart. Phys. 0901 (2009) 043.
[213] P. Lipari, Phys. Rev. D 99 (2018) 043005.
[214] B. Katz, K. Blum, J. Morag, E. Waxman, Mon. Not. R. Astron. Soc. 405 (2010) 1458.
[215] R. Cowsik, L.W. Wilson, Proc. 13th Int. Cosmic Ray Conf. Vol. 1, 1973, p. 500.
[216] E.A. Bogomolov, et al., Proc. 16th Int. Cosmic Ray Conf. Vol. 1, 1979, p. 330.
[217] R.L. Golden, et al., Phys. Rev. Lett. 43 (1979) 1196.
[218] M. Boezio, Braz. J. Phys. 44 (2014) 441.
[219] G. Jungman, M. Kamionkowski, K. Griest, Phys. Rep. 267 (1996) 195.

[220] S. Hawking, Nature 248 (1974) 30.
[221] P. Kiraly, et al., Nature 293 (1981) 120.
[222] M. Winkler, J. Cosmol. Astropart. Phys. 1702 (2017) 048.
[223] K. Abe, et al., Phys. Lett. B 670 (2008) 103.
[224] K. Abe, et al., Phys. Rev. Lett. 108 (2012) 051102.
[225] O. Adriani, et al., Phys. Rev. Lett. 105 (2010) 121101.
[226] O. Adriani, et al., JETP Lett. 96 (2013) 621.
[227] M. Aguilar, et al., Phys. Rev. Lett. 117 (2017) 091103.
[228] A. Cuoco, M. Krämer, M. Korsmeier, Phys. Rev. Lett. 118 (2017) 191102.
[229] M.Y. Cui, Q. Yuan, Y.L.S. Tsai, Y.Z. Fan, Phys. Rev. Lett. 118 (2017) 191101.
[230] I. Cholis, T. Linden, D. Hooper, Phys. Rev. D 99 (2019) 103026.
[231] D. Hooper, L. Goodenough, Phys. Lett. B 697 (2011) 412.
[232] T. Aramaki, et al., Phys. Rep. 618 (2016) 1.
[233] F. Donato, N. Fornengo, P. Salati, Phys. Rev. D 62 (2000) 043003.
[234] E. Carlson, et al., Phys. Rev. D 89 (2014) 076005.
[235] H. Baer, S. Profumo, J. Cosmol. Astropart. Phys. 0512 (2005) 008.
[236] F. Donato, N. Fornengo, D. Maurin, Phys. Rev. D 78 (2008) 043506.
[237] A. Ibarra, S. Wild, Phys. Rev. D 88 (2013) 023014.
[238] L. Dal, A. Raklev, Phys. Rev. D 89 (2014) 103504.
[239] H. Fuke, et al., Phys. Rev. Lett. 95 (2005) 081101.
[240] V. Choutko, F. Giovacchini, Proc. 30th Int. Cosmic Ray Conf. Vol. 4, 2008, p. 765.
[241] K. Perez, et al., 2019, arXiv:1904.05938.
[242] F. Donato, N. Fornengo, D. Maurin, P. Salati, Phys. Rev. D 69 (2004) 063501.
[243] M. Cirelli, N. Fornengo, M. Taoso, A. Vittino, J. High Energy Phys. 1408 (2014) 009.
[244] M. Aguilar, et al., Phys. Rep. 366 (2002) 331.
[245] O. Adriani, et al., Phys. Rep. 544 (2014) 323.
[246] K. Abe, et al., Phys. Rev. Lett. 108 (2012) 131301.
[247] A. Kounine, et al., Proc. Sci. ICRC2017 (2018) 1093.
[248] V. Poulin, et al., Phys. Rev. D 99 (2019) 023016.
[249] P. Auger, et al., Rev. Modern Phys. 11 (1939) 288.
[250] J. Abraham, et al., Phys. Rev. Lett. 101 (2008) 061101.
[251] D. Ivanov, et al., Proc. Sci. ICRC2015 (2016) 349.
[252] V.S. Berezinsky, S.I. Grigorieva, Astron. Astrophys. 199 (1988) 1.
[253] F. Sarazin, et al., Bull. Am. Astron. Soc. 51 (2019) 93.
[254] A. Aab, et al., Astrophys. J. Lett. 853 (2018) L29.
[255] R.U. Abbasi, et al., Astrophys. J. Lett. 790 (2014) L21.
[256] K. Kawata, et al., Proc. Sci. ICRC15 (2016) 276.
[257] A. Neronov, D.V. Semikoz, I. Vovk, R. Mirzoyan, Phys. Rev. D 94 (2016) 123018.
[258] A. Aab, et al., Phys. Rev. Lett. 117 (2016) 192001.
[259] R. Alves Batista, et al., Front. Astron. Space Sci. 6 (2019) 23.
[260] E. Witten, Phys. Rev. D 30 (1984) 272.
[261] J. Madsen, Phys. Rev. D 71 (2005) 014026.
[262] M.A. Perez-Garcia, J. Silk, J.R. Stone, Phys. Rev. Lett. 105 (2010) 141101.
[263] B. Khrenov, et al., Nucl. Phys. B 113 (2002) 115.
[264] M. Casolino, et al., Proc. Sci. ICRC2017 (2017) 368.
[265] P.D. Serpico, J. Astrophys. Astron. 39 (2018) 41.
[266] C. Evoli, R. Aloisio, P. Blasi, Phys. Rev. D 99 (2019) 103023.
[267] F. Donato, IAU Symp. 331 (2017) 220.
[268] S. Gabici, et al., 2019, arXiv:1903.11584.
[269] S.N. Zhang, et al., Proc. Sci. 2017 (2018) 1077.
[270] R. Battiston, et al., High precision particle astrophysics as a new window on the universe with an antimatter large acceptance detector in orbit (ALADInO), in: Presented At Voyage 2050 Workshop Shaping the European Space Agency's Space Science Plan for 2035-2050, 2019.
[271] S. Schael, et al., Nucl. Instrum. Methods A 944 (2019) 162561.
[272] A. Olinto, et al., 2019, arXiv:1907.06217.